UNIVERSITA DEGLI STUDI DI NAPOLI "FEDERICO II"

Corso di dottorato in DINAMICA INTERNA DEI SISTEMI VULCANICI E RISCHI IDROGEOLOGICO-AMBIENTALI

XXV CICLO

Ph.D. Thesis

Constraints on the origin of the nodules from the Sarno (Pomici di Base) plinian eruption of Mt. Somma-Vesuvius (Italy) based on geochemical studies

Rita Klébesz

Advisors:

Prof. B. De Vivo (Universita degli Studi di Napoli "Federico II", Naples, Italy)

Prof. R. J. Bodnar (Virginia Polytechnic Institute and State University, Blacksburg, VA, USA)

March 2012

Abstract

Four, “sub-effusive” type of nodules, collected from the uppermost layer of the Sarno (Pomici di Base - PB) plinian eruption, were studied in this doctoral research. This thesis presents new geochemical data (major/trace elements and volatiles) of both melt inclusion (MI) and minerals of the studied nodules. The main goal of this research was to constrain the formation depth of the nodules, and hence the depth of the magma chamber associated with the Sarno (PB) eruption, but later the focus shifted on the origin of melts trapped in representative minerals of the nodules.

A detailed petrographic study was carried out on all four selected nodules. They have porphyrogranular texture, but they differ in terms of modal composition. Three of the four nodules contain clinopyroxene and olivine as phenocrysts (Type A nodules), whereas one contains amphibole (Type B). The groundmass in both cases is completely crystallized, and crystallized melt pockets were also recognized in the interstitial space.

MI are abundant in clinopyroxenes in the nodules. All MI observed in this study are partially to completely crystallized, suggesting they cooled relatively slowly after trapping. Two types of MI can be distinguished based on petrography. Type I consists of mica, Fe-Ti-oxide minerals and/or dark green spinel, clinopyroxene, feldspar and a vapor bubble. No volatile species (CO_2, H_2O) were detected in the bubbles during Raman analysis. Type II inclusions are generally lighter in color and they contain feldspar and/or glass and oxides. Both types of MI are randomly distributed in the crystals or occur along a growth zone and are interpreted to be primary. Some of the MI were analyzed by LA-ICP-MS without homogenizing them first, but most of the MI were heated to produce a homogeneous glass phase before analysis. MI homogenized between 1202-1256 °C, but mostly above 1220 °C. Type I MI can be classified as phono-tephrite – tephri-phonolite – basaltic trachy-andesite, whereas Type II MI have mainly basaltic composition. The two different types of MI also show different trace element patterns. Type I MI are more enriched in incompatible elements compared to Type II MI. The heating experiments revealed, however, that only Type I MI are representative of the crystallizing melt. The compositions of Type II MI are strongly modified by accidentally trapped An-rich feldspar.

The comparative study of Type I MI and bulk rock of Mt. Somma-Vesuvius concluded that compositions of Type I MI are similar to the bulk composition of the pre-Sarno, older Somma lava rocks rather than the Sarno (PB) volcanics. Therefore, the NLM1-1a nodule and perhaps the other two Type A nodules have formed from the same melt that was erupted during the early history of Mt. Somma. The presence of older, crystallized material in the younger eruptive products indicates that the Sarno (PB) magma erupted from the same (or a deeper) magma chamber(s) that fed the older eruptions. The thermobarometer models estimate at least 4 kbar (~12 km) for nodule formation.

MI were also studied in amphibole from Type B nodules. The petrographic and geochemical studies, however suggested that the compositions of these MI are strongly modified by trapping solid inclusions, including phlogopite and less commonly, apatite. Therefore, the origin of Type B nodules cannot be determined based on MI compositions. Most likely this nodule crystallized from a melt that was more enriched in light REE, but less enriched in Ti, compared to melts from which Type A nodules crystallized. Thermobarometer models estimate at least 8 kbar (~24 km) for Type B nodule formation.

Table of Contents

Preface

In the processes of this doctoral research and writing this thesis, I have received considerable help and support from various people who I would like to thank here. First of all, my advisors, Prof. Benedetto de Vivo (University of Naples "Federico II") and Prof. Robert J. Bodnar (Virginia Tech) are acknowledged for their instructions and guidance. I would also like to thank to Prof. Paola Petrosino (University of Naples "Federico II") for field work assistance, Annamaria Lima (University of Naples "Federico II") for showing me the sample preparation techniques and for scientific guidance, and Kálmán Török (Eötvös Loránd Geophysical Institute) for helping with the petrographic studies. In addition, I would like to thank all of them for participating in a co-authored article. I would also like to thank to Ph.D. candidate Daniele Redi for field work assistance.

I am grateful for the opportunity to work as a research scholar at the Department of Geosciences of Virginia Tech. I would like to thank to the members of the Fluid Research Group and another visiting scholar, Ph.D. candidate Angela Doherty for their guidance, help and support. I would particularly like to express my gratitude for Ph.D. candidate Rosario Esposito for all our discussions, talks and his support; and Ph.D. candidate Daniel Moncada for helping out in the laboratory during sample preparation. I would also like to thank to Prof. Esteban Gazel for his enthusiasm in our discussions about MI data. I appreciate the assistance of Research Associate Luca Fedele (Virginia Tech) with the microanalytical work with LA-ICP-MS, SEM and EPMA, and the help of Laboratory Technician Charles Farley with Raman analysis.

Ph.D. candidate Balázs Kiss (Eötvös Loránd University) is acknowledged for being enthusiastic about helping to understand the amphibole data and the different thermobarometers.

I would also like to thank to Prof. Csaba Szabó (Eötvös Loránd University), Harvey E. Belkin (U.S. Gelogical Survey) and Ph.D. candidate Orsolya Győri (Eötvös Loránd University) for their thorough pre-examination and constructive comments on this manuscript.

The research was partially funded by the Ph.D. Program (XXV Cycle, Coordinated by B. De Vivo) "Internal dynamics of volcanic systems and hydrogeological-environmental risks" of the University of Naples Federico II (Italy), in collaboration with Virginia Tech in the framework of the Memorandum of Understanding (MoU) signed by the two Universities. This work supported in part by the National Science Foundation under Grant no. EAR-1019770 to R. J. Bodnar.

Last but not least, I would like to thank my spouse, Ákos, for his love, and for putting up with me and giving support when I've been stressed out. I am also grateful for the constant support and understanding of my family and my friends.

1. Introduction

Mt Somma-Vesuvius is one of the most studied volcanoes in the world. It is located in a densely populated area near Naples in South Italy. A catastrophic eruption – which has occurred several times during the history of the volcano – would affect the lives of many. Therefore, the interest in this volcano is not purely scientific, but also has a practical component, namely risk assessment. There is no reliable method to predict a future eruption, even with close monitoring. However, the more we know about a volcano and how and when its previous eruptions happened, the better we can interpret the signals recorded today and make plans in case of a future eruption (De Vivo *et al.*, 2010). The aim of this doctoral research is to contribute to the existing knowledge about Mt. Somma-Vesuvius by studying samples from the Sarno (Pomici di Base – PB) eruption. This eruption – one of the oldest of Mt. Somma-Vesuvius – was chosen because it has not previously been studied in detail. In the following pages I describe the eruptive history according to Rolandi (1997), and in parenthesis the names according to Santacroce (1987) are listed.

Eruptive activity associated with the volcanic complex started after the highest magnitude eruption in the Campanian Magmatic Province, the Campanian Ignimbrite eruption (39 ka; De Vivo *et al.*, 2001). Other volcanic activity in the area dates back to *ca.* 400 ka (Brocchini *et al.*, 2001; De Vivo *et al.*, 2001; Rolandi *et al.*, 2003; Santacroce *et al.*, 2008 and references therein). The eruptive activity of the Mt. Somma-Vesuvius volcano is cyclical. Several plinian or subplinian eruptive events have occurred, usually followed by mildly explosive activity, referred to as interplinian eruptions (Rolandi *et al.*, 1998). The interplinian stage and the next plinian or subplinian eruption are separated by repose times that could last over several thousands of years.

The bulk rock compositional data define three groups, *i.e.*, three mega-cycles (Arnó *et al.*, 1987; Ayuso *et al.*, 1998; Civetta and Santacroce, 1992). The products of the first mega-cycle are slightly silica-undersaturated (K-trachyte, K-latite; Ayuso et al., 1998; Barberi et al., 1981; Di Renzo et al., 2007; Joron et al., 1987; Landi et al., 1999; Paone, 2006; 2008; Piochi et al., 2006a; Santacroce et al., 2008). The products of the second mega-cycle are mildly silica-undersaturated (phonotephrites to phonolites; Aulinas *et al.*, 2008; Ayuso *et al.*, 1998; Cioni *et al.*, 1998; Civetta *et al.*, 1991; Di Renzo *et al.*, 2007; Joron *et al.*, 1987; Paone, 2006; 2008; Piochi *et al.*, 2006a; Santacroce *et al.*, 2008; Somma *et al.*, 2001; Sulpizio *et al.*, 2010). The third mega-cycle is characterized by strongly silica-undersaturated rocks with tephrite to tephriphonolite-foidite composition (Ayuso et al., 1998; Barberi et al., 1981; Belkin et al., 1998; 1993; Black et al., 1998; Cioni et al., 1995; 1998; Civetta et al., 1991; Joron et al., 1987; Marianelli et al., 1999; 2005; Marini et al., 1998; Mastrolorenzo et al., 1993; Mues-Schumacher, 1994; Paone, 2006; 2008; Piochi et al., 2006a; Rolandi et al., 1993a; Rosi and Santacroce, 1983; Santacroce et al., 1993; 2008; Somma et al., 2001; Villemant et al., 1993).

The first mega-cycle lasted from >25 ka to about 14 ka, and includes the older Somma activity, the Codola, the Sarno (BP), and the Novelle (Verdoline) plinian eruptions and the subsequent interplinian stages. The second mega-cycle started around 8 ka and lasted until about 2.7 ka, incorporating the Ottaviano (Mercato) and Avellino plinian eruptions and protohistoric interplinian activity. The third mega cycle started in 79 AD with the Pompei plinian eruption and the subsequent ancient historic interplinian activity. Two other subplinian eruptions belong to this mega-cycle; the 472 AD (Pollena) and

the 1631 AD eruptions, both followed by interplinian activity. The last eruption occured in 1944 and that eruption either represents the end of the most recent mega-cycle or an unusually long repose time between eruptions within the continuing third mega-cycle (De Vivo *et al.*, 2010 and references therein).

The eruptive products of the third mega-cycle have been extensively studied. The research focused mainly on the juvenile products (Ayuso et al., 1998; Barberi et al., 1981; Belkin et al., 1998; 1993; Black et al., 1998; Cioni, 2000; Cioni et al., 1995; 1998; Civetta et al., 1991; Fulignati and Marianelli, 2007; Joron et al., 1987; Lima et al., 1999; Marianelli et al., 1995; 1999; 2005; Marini et al., 1998; Mastrolorenzo et al., 1993; Mues-Schumacher, 1994; Paone, 2006; 2008; Piochi et al., 2006a; Raia et al., 2000; Rolandi et al., 1993a; Rosi and Santacroce, 1983; Santacroce et al., 1993; 2008; Schiano et al., 2004; Somma et al., 2001; Vaggelli et al., 1993; Villemant et al., 1993; Webster et al., 2001) and on the co-genetic or xenolitic lithic fragments, referred to as nodules (Barberi and Leoni, 1980; Belkin and De Vivo, 1993; Belkin et al., 1985; Cioni et al., 1995; Cundari, 1982; Del Moro et al., 2001; Fulignati and Marianelli, 2007; Fulignati et al., 1998; 2001; 2004; 2005; Gilg et al., 2001; Hermes and Cornell, 1978; 1981; Lima et al., 2003; 2007; Savelli, 1968; Sorby, 1858). As a result of these studies, the composition of the source region, the structure of the plumbing system, the pre-eruptive processes and volatile contents of the magmas are fairly well constrained, at least for the most recent mega-cycle. The older eruptions, especially those in the first mega-cycle, are less studied. While abundant data are available for the whole rock composition of the juvenile products, much less information is available for the melt inclusions (MI). Therefore, the pre-eruptive volatile compositions and the nature of the plumbing system for the first mega-cycle are not as well defined as for the third mega-cycle.

1.1. The aim and objectives of the research

The original goal of this and a related doctoral study carried out by Daniele Redi was to collect nodules and juvenile volcanic products from the older (pre-79 AD) plinian eruption and systematically determine the pre-eruptive volatile content of the magmas and estimate the crystallization depth to provide information about the structure of the plumbing system during the early stages of the volcano. Due to the lack of nodules in the Novelle (Verdoline) and Ottaviano (Mercato) eruptions we could not achieve our original goal, therefore we shifted our focus to the nodules found in the Sarno (PB) eruption. However, the estimation of depths of formation of nodules from the Sarno (PB) eruption was hampered by both the lack of fluid inclusions (FI) and poor constraints on the origin of the nodules. For these reasons, I have focused on the origin of melts trapped in representative minerals of the nodules, and I have included a discussion about the attempts to estimate the pressure and temperature of crystallization of the nodules. In particular, I present new geochemical data (major/trace elements and volatiles) from both MI and minerals representative of nodules ejected during the Sarno (PB) eruption, to provide a detailed geochemical description of the samples.

1.2. Publications in this thesis

This research focused on the petrographic and geochemical characterization of the nodules found in the Sarno (PB) eruption, including the detailed study of the MI hosted by the rock-forming minerals. Some of the results have been published.

Article 1, *Composition and origin of nodules from the ≈20 ka Pomici di Base (PB)-Sarno eruption of Mt. Somma — Vesuvius, Italy* (by Rita Klébesz, Robert J. Bodnar, Benedetto De Vivo, Kálmán Török, Annamaria Lima and Paola Petrosino) summarizes the petrographic description of the nodules and the preliminary results of the geochemical analyses of the MI and their mineral hosts. This publication also includes a hypothesis concerning the origin of the nodules.

Article 2, *Application of the Linkam TS1400XY heating stage to melt inclusion studies* (by Rosario Esposito, Rita Klebesz, Omar Bartoli, Yury I. Klyukin, Daniel Moncada, Angela L. Doherty, Robert J. Bodnar) is related to my research topic because this stage was used to homogenize MI for my study. A Linkam TS1400XY heating stage was tested for its suitability to homogenize multiphase MI and quench them to a homogeneous glass. The optical viewing quality was also evaluated during the experiments. Three different samples were used for the experiments, including clinopyroxene crystals from a nodule from the Sarno (PB) eruption. As discussed below, the MI in nodules from the Sarno (PB) eruption are crystallized, therefore it was necessary to homogenize the MI before the geochemical analyses. The Linkam stage was used for the homogenization experiments and these result were included in the above mentioned paper (Esposito *et al.*, 2012).

A third paper is in preparation which will include a detailed geochemical description of the samples, including trace element composition of the rock-forming minerals and major, trace and volatile element compositions of MI obtained after homogenizing the MI.

2. Theoretical framework

2.1. Why and how do we study fluid and melt inclusion?

Fluid inclusions (FI) and melt inclusions (MI) are small droplets of the fluid phase that are trapped during crystal growth. The state of the trapped fluid can be liquid, vapor or supercritical fluid, and its composition can also vary from essentially pure water, CO_2, brines, to silicate, sulfide or carbonate melts (Bodnar, 2003). Most commonly the term FI is used for those inclusions that are mainly in the fluid state at ambient surface conditions, while MI refers to inclusions that contain mostly glass or crystalline solids at ambient surface conditions (Roedder, 1984). FI are widely used in studies of magmatic rocks, as well as sedimentary and metamorphic rocks to answer various questions, such as the pressure and/or temperature of the formation, source of the fluids, relative timing of fluid migration, reconstruction of tectonic history, etc. (Goldstein and Reynolds, 1994). MI can provide valuable information about melt generation and evolution, and the trapping conditions (Anderson 2003). In addition, MI represent the only tool that can provide the pre-eruptive volatile (such as H_2O, CO_2, S, Cl, F) content of a magma. The bulk rock measurements can only give a minimum estimate of volatiles owing to continued degassing during ascent and emplacement on the surface (Lowenstern, 2003). Volatiles are extremely important in volcanic processes, because they are the main driver of magma ascent, fragmentation and hence they have a big influence on eruption type.

The importance of FI and MI in nodules is that they record the transition from silicate melt to volatile-rich magmatic fluids at the magma chamber margins between the magma-dominated system and the fluid-dominated hydrothermal system (De Vivo *et al.*, 2006). These FI and MI provide crucial information about the processes that play a major role in ore formation and in the control of eruption styles (De Vivo *et al.*, 2006). The immiscibility of Cl-rich hydrosaline fluids and melts is important for element (including ore metal) transport from the deep Earth into the atmosphere, hydrosphere and hydrothermal system (Kamenetsky *et al.*, 2004), and thus is critical to ore deposit formation (Kamenetsky *et al.*, 2004; Roedder, 1992; Webster, 2004). The coexistence of CO_2 and/or H_2O-rich FI and MI is a good indicator that at some point the melt became volatile saturated. At that point, volatile species are partitioned between the magma and the vapor phase based on their relative solubilities and abundances (Carroll and Webster, 1994). Volatile solubility mainly depends on pressure, temperature and the composition of the melt. Volatile solubility can be experimentally determined by equilibrating a known melt composition under fluid-saturated conditions at known P and T, and then quenching the liquid to glass, and measuring the volatile concentration in the glass. These experimental data sets can be used to develop models that allow interpolation and extrapolation of the data to conditions and compositions that may not have been investigated or may not be experimentally possible (Moore, 2008 and references therein). Using these models (*e.g.*, Newman and Lowenstern, 2002; Papale et al., 2006), the saturation pressure (depth) can be estimated based on the volatile content in glassy natural samples (*e.g.*, MI in minerals, interstitial glass) and entrapment temperature, which can be calculated or estimated from mineral equilibria (Holloway and Blank, 1994). These models require the assumption of volatile saturation in the melt. Therefore, if we do not observe coeval FI and MI, or have other geochemical evidence that the melt was volatile-saturated, then the depth estimated from the pressure

represents a minimum estimate, not necessary the true trapping depth. In addition, most of these models consider only the solubility of H_2O and CO_2, but experimental studies (*e.g.*, Botcharnikov et al., 2004; Webster et al., 2006; Webster et al., 2009) show that even a small amount of S influences the solubility of Cl, and indirectly the solubility of H_2O. Webster *et al.* (2012) provide further evidence for the need for more experimental works involving more than two volatiles. In addition they emphasize, that the addition of even one volatile element (Cl) to the CO_2-H_2O-melt system greatly reduces the solubility of CO_2 in a phonolitic melt, resulting in the formation of two fluid phases. Therefore, they suggest that existing models – which considers only the solubility of H_2O and CO_2 in the melt – should not be used to estimate the saturation pressure for those systems where other volatiles (Cl, S, F) appear in significant concentration (*e.g.*, Mt. Somma-Vesuvius, Balcone-Boissard et al., 2012; Cioni et al., 1998; Fulignati et al., 2001; Fulignati and Marianelli, 2007; Lima et al., 1999; Lima et al., 2007; Marianelli et al., 1999; 2005; Webster et al., 2001 and references therein). In summary, the presence of CO_2-H_2O, CO_2 and MI in the same FIA can be (Roedder and Bodnar, 1980) and have been used successfully (*e.g.*, Belkin and De Vivo, 1993; Belkin et al., 1985) to determine the trapping depth based on the CO_2 density of the FI. It is important to emphasize that MI and FI found in nodules provide direct information concerning the magma chamber depth, because nodules form *in situ* along the walls and bottom of the magma chamber.

Recent advances in analytical techniques provide the opportunity to obtain detailed information from MI and FI. Today, heating and freezing stages are routinely used for FI microthermometry, and data obtained can be used to estimate the minimum or actual trapping pressure and temperature and the salinity and/or density of the FI (Roedder, 1984). Frezzotti *et al.* (2012) reviews the various application of Raman spectroscopy in FI studies, such as qualitative detection of solid, liquid and gaseous components, identification of polyatomic ions in solution, calculation of the density of CO_2 fluids, the chemistry of aqueous fluids, and the molar proportions of gaseous mixtures present as inclusions, and measurement of the pH range and oxidation state of fluids. The main advantages of the Raman technique are that it requires minimal sample preparation and it is a non-destructive method. Laser Ablation Inductively Coupled Plasma-Mass Spectrometry (LA-ICP-MS) and Particle Induced X-ray Emission (PIXE) analysis are most commonly used to determine the trace element composition of the FI. The former method is a destructive method, but it offers the possibility to analyze many elements over a wide range in concentrations (Gunther *et al.*, 1998; Heinrich *et al.*, 2003) PIXE is a non-destructive method, and offers low detection limits for certain elements, therefore it is most commonly used in ore forming environments (Ryan *et al.*, 1995).

Most methods used for MI analyses require a homogeneous, glassy sample. MI that were erupted onto the surface shortly after trapping and cooled quickly generally remain glassy. MI in sub-effusive rocks and deep magmatic intrusions are often partially or completely crystallized due to slow cooling after trapping (Bodnar and Student, 2006; Roedder, 1979). Therefore, crystallized MI must be homogenized prior to analysis, using one of several techniques, *e.g.*, heating in one-atmosphere furnaces, in high-pressure vessels or in a microscope-mounted high temperature stage (Bodnar and Student, 2006 and references therein). The method most commonly used to determine the major element abundances (and some minor and volatile elements) in MI is electron microprobe (EPMA). LA-ICP-MS is most commonly used to determine the trace element concentration (Heinrich *et al.*, 2003) but it is also the only method that can be used to analyze crystallized inclusions (Halter *et al.*, 2002).

Secondary Ion Mass Spectrometry (SIMS) can also be used to measure trace and volatile element concentrations in MI. Fourier Transform Infrared (FTIR) Spectroscopy is used to measure the H_2O and CO_2 content in the MI, and it also provides information about the speciation of the volatile species (Hervig *et al.*, 2003). For MI smaller than 30 μm that cannot be abalyzed by SIMS, Confocal Laser Raman Spectroscopy can be used to determine the H_2O content (Thomas, 2000; Zajacz *et al.*, 2005).

Finally, it is important to emphasize that even when accurate analytical data are available, any given question can only be answered if the MI and FI populations are carefully selected. In FI studies the concept of fluid inclusion assemblage (FIA – "a group of fluid inclusions that were all trapped at the same time", Goldstein and Reynolds, 1994) is accepted and widely used. In practice this means that FI in a given FIA were all trapped at approximately the same conditions (P, T) and all trapped a fluid of approximately the same composition (Bodnar, 2003). Esposito *et al.* (2010) argue that studying assemblages is also necessary in MI studies in order to provide reliable information concerning the pre-eruptive volatile content. Unfortunately, studying MI assemblages (MIA) is not always possible, due to sample preparation methods required for MI analysis and because MIA cannot always be identified.

2.2. Previous studies on nodules from Mt. Somma-Vesuvius

The most recent review by De Vivo *et al.* (2010) summarizes our current knowledge about the source region, plumbing system and volcanic activity of Mt. Somma-Vesuvius. In this chapter I will focus only on studies that were carried out on nodules, particularly on those that described FI and MI analyses (Fig. 1).

The term "nodule" does not have a strict definition. In the Mt. Somma-Vesuvius literature it refers to ejecta commonly present in the pyroclastic products, with a wide variability in composition and texture. Nodules can be metamorphic and/or metasomatized sedimentary rocks, ranging from carbonates to silicic skarn rocks, and coarse-grained igneous rocks and cumulate rocks. Zambonini (1910) was the first to describe nodules, but the classification which has been used recently was proposed by Hermes and Cornell (1978). They divided the nodules into four groups: 1) ultramafic cumulates, 2) "skarns", which are metasomatized carbonates, 3) recrystallized carbonate hornfels, and 4) "sub-effusive" rocks which are shallow plutonic rocks. The first two types (cumulates and skarns) have been extensively studied (Barberi and Leoni, 1980; Belkin and De Vivo, 1993; Belkin et al., 1985; Cioni et al., 1995; Cundari, 1982; Del Moro et al., 2001; Fulignati and Marianelli, 2007; Fulignati et al., 1998; 2001; 2004; 2005; Gilg et al., 2001; Hermes and Cornell, 1978; 1981; Lima et al., 2003; 2007; Savelli, 1968; Sorby, 1858).

The earlier studies focused on constraining the physical parameters of nodule genesis, but did not consider the origin of the nodules or whether they are co-genetic with their pyroclastic hosts. Sorby (1858) studied metasomatized carbonate ejecta and concluded that the minerals formed between 340 and 380 °C and at a depth of about 0.6-1 km. Barberi and Leoni (1980) also studied skarns, but they assumed a temperature range of 360-790 °C and a maximum depth of 5-6 km. Cortini *et al.* (1985) estimated the crystallization temperature of phenocrysts to be 850-1050 °C in skarns, and 1170-1240 °C in cumulates, based on the homogenization temperatures of MI. Belkin *et al.* (1985) and Belkin and De Vivo (1993) suggested multistage crystallization history, based on the CO_2 FI density and their bimodal

distribution, and estimated 3.5-10 km and 4-10 km for the depth of nodule formation for the interplinian and the plinian eruptions, respectively. Belkin and De Vivo (1993) also noted that FI in nodules from the plinian eruption have higher H_2O-content compared to those from the inter-plinian eruption.

	Reference	Rock type	FI	MI T_{hom}	Estemated depth	MI comp.	Samples available
1944	Belkin et al., 1985	skarn	CO_2 - bimodal (0.31-0.72 g/cm3)	~ 1000 °C	3.5-13 km		DV11, DV12, N3, N13, N1
		cum.	pure CO_2 - ~0.35 g/cm3	~ 1200 °C	4-7 km		
	Cortini et al., 1985	cum.		1170-1240 °C			
		skarn		lower			
	Fulignati et al., 2004	fergusite				K-phonotephrite/K-tephriphonolite	
		skarn		800-920°C 1010-1022°C		major elemnts, Cl	
				1228		Multiphase (silicate glass+liquid+daughter minerals)	
	Fulignati et al., 2000	phlog.-sakarn	two phase CO_2	1010-1033°C	1.5-3 km	major, Cl, S	
		melilite-skarn	two phase CO_2, multiphase hydrosaline MI	790-920 °C	1.5-3 km	major, Cl, S	
	Lima et al., 2003	bi-wherlite		1130-1240 °C		major elements, trace elements, Cl, F, SO_2, H_2O	
	Lima et al., 2007	DV11				major elements, Cl, F, SO_2	
472 AD	Belkin & De Vivo, 1993	cum. and subeffusive	CO_2-H_2O (75%); pure CO_2 (25%)	~ 1200 °C	4-10 km		DV5, DV6, 609, 611
	Fulignati et al., 2001	syenitic and skarn	Four principal types of melt inclusions represent highly differentiated phonolite (type 1), hydrosaline melt (type 3), unmixed silicate–salt melts (type 2), and a complex chloride-carbonate melt with minor sulfates (type 4).	510-810 °C		major elements	
	Fulignati et al., 2004	syenite	hypersaline FI				
		skarn		860-885 °C		Multiphase (carbonate bearing): major elements, Cl	
	Fulignati & Marianelli, 2007	syenitic				major elements, trace elements, Cl, F, SO_2, H_2O, CO_2(below det.)	
79 AD	Belkin & De Vivo, 1993	cum. and subeffusive	CO_2-H_2O (75%); pure CO_2 (25%)	~ 1200 °C	4-10 km		DV7, DV8, 503, 506
	Gilg et al., 2001	skarn	primary silicate melt inclusions	1000-1050 °C	~ 2.5-5 km		
			CO_2 ± H_2S-rich fluid inclusions				
			multiphase aqueous brine inclusions with mainly sylvite and halite daughter minerals	720-820 °C			
			complex chloride-carbonate-sulfate-fluoride-silicate-bearing saline-melt inclusions	870-890 °C			
	Fulignati et al., 2004	syenite	hypersaline FI	970-980°C			
		skarn	hypersaline FI				
	Fulignati et al., 2005	syenitic	multiphase FIs	760-830 °C			
	Lima et al., 2007	506				major elements, Cl, F, SO_2	
Avellino	Belkin & De Vivo, 1993	cum. and subeffusive	CO_2-H_2O (75%); pure CO_2 (25%)	~ 1200 °C	4-10 km		DV1, DV2, DV3, DV4
	Gilg et al., 2001	skarn	primary silicate melt inclusions	1000-1050 °C	~ 2.5-5 km		
			CO_2 ± H_2S-rich fluid inclusions				
			multiphase aqueous brine inclusions with mainly sylvite and halite daughter minerals	720-820 °C			
			complex chloride-carbonate-sulfate-fluoride-silicate-bearing saline-melt inclusions	870-890 °C			

Figure 1. – Summary of previous FI and MI studies of nodules from plinian and sub-plinian eruptions at Mt. Somma-Vesuvius.

The origin and genesis of the nodules from Mt. Somma-Vesuvius has been controversial. Based on the mineral assemblages and the interstitial glass compositions, Hermes and Cornell (1981; 1983) inferred that the cumulate nodules formed over a range of depths, with a maximum pressure of 3 kbar. But, Varekamp (1983) argued that all nodules were derived from the same, shallow source. Savelli (1968) examined carbonate ejecta and concluded, based on the non-equilibrium assemblages, that there was no direct evidence of wall rock assimilation but rather that a metasomatism by volcanic fluids and gases was responsible for the observed compositions. Now it is generally accepted that the silicate crystalline nodules and the skarns represent samples of the heterogeneous wall of the magma chamber. The large compositional variations reflect the gradual changes from the carbonate country rock through skarns, metasomatized cumulate rocks to a cumulate crystal mush along the inner walls of the chamber (Cioni *et al.*, 1995).

Many studies have focused on skarn and silicic nodules from post 79 AD plinian eruptions in order to understand the processes at the magma/wall rock interface and constrain the underlying plumbing system of the volcano. These studies (Del Moro et al., 2001; Fulignati et al., 1998; 2000; 2001; 2004; 2005; Gilg et al., 2001) concluded that skarn generation can be explained by carbonate wall rock assimilation by mafic alkaline magma that leads to exsolution of CO_2-rich vapor and complex saline melts from the contaminated magma. These fluids react with the carbonate wall rock resulting in skarn formation. All of the above studies estimate a high (magmatic) temperature, above 700 °C, for skarn formation.

Lima *et al.* (2003) and Lima *et al.* (2007) constrain the post 79 AD evolution of Mt. Somma-Vesuvius based on compositional data from FI and MI. According to their proposed model, separate small magma chambers exist at depths of >3.5 km and possibly a larger chamber is present at a depth of > 12 km. In this model, interplinian periods represent a steady state condition under the volcano. During these periods, the volcano acts like an "open system" which means the ongoing magma supply is always followed by eruption. However, at the end of these periods, cooling of the magma leads to the precipitation of newly formed crystals, which subsequently leads to self-sealing, and hence "closing" of the system. In this situation the pressure can build up, leading to a subsequent highly explosive plinian eruption. These workers also showed that a carapace forms around the upper portion of the shallow magma chamber (3.6-4.5 km) and acts as an interface between the brittle and plastic rocks.

In summary, studies of nodules from Mt. Somma-Vesuvius have mostly focused on samples from the third mega-cycle, and MI studies are much less common.

2.3. The Sarno (Pomici di Base - PB) plinian eruption

The nodules examined during this study were collected from the Sarno (PB) eruption; therefore it is necessary to briefly summarize our current knowledge about this eruption. According to Santacroce *et al.* (2008), the PB eruption represents the first explosive event of the Somma volcano that can be unequivocally related to Mt. Somma-Vesuvius (Fig. 2a). Other authors (Ayuso *et al.*, 1998; Rolandi, 1997) refer to this event as the Sarno eruption, and report that it follows an older explosive event, the Codola eruption. However, the origin of the Codola eruption is currently a matter of debate (Di Vito *et al.*, 2008; Giaccio *et al.*, 2008; Sulpizio *et al.*, 2003). We use the term Sarno (PB) eruption to recognize the fact

that the two different names are commonly used in the literature (Pomici di Base and Sarno) to refer to the same eruptive event. The age of the Sarno (PB) eruption was first reported by Delibrias *et al.* (1979) as 17,050 ± 140 BP based on ^{14}C determination on soil organic matter. Bertagnini *et al.* (1998) obtained ^{14}C ages of 18,750 ± 420 and 19,170 ± 420 BP from paleosol samples. Their findings are in agreement with the ^{14}C age of 18,300 ± 180 BP from paleosol by Andronico *et al.* (1995). A more recent ^{14}C analysis on charcoal (Siani *et al.*, 2004) yields an average maximum age of 22,030 ± 175 yr BP (Santacroce *et al.*, 2008). Based on these studies, the Sarno (PB) eruption is thought to have occured around 20 ka BP.

Based on extensive study of the eruptive products of the Sarno (PB) eruption, Bertagnini *et al.* (1998) reconstructed three phases of the eruption (Fig. 2b): (1) the opening phase consisting of ash and minor pumice fall followed by (2) a plinian phase comprising up to 6.5 m of compositionally zoned (trachyte to latite) fallout deposits with minor surge deposits, and (3) the closing phreatomagmatic phase characterized by lithic-rich falls, surges and flows. According to Bertagnini *et al.* (1998), the Sarno (PB) eruption was the largest eruptive event in the history of Mt. Somma-Vesuvius on the basis of the thickness and areal distribution of the erupted material. Subsequent to the plinian activity the upper part of the Somma cone slid northwestwards (Bertagnini *et al.*, 1998). Cioni *et al.* (1999) found clear evidence of a caldera collapse associated with the Sarno (PB) eruption, and Rolandi *et al.* (2004) suggested that the Sarno (PB) eruption was one of four eruptive events that contributed to the destruction of the older Somma cone.

The chemically zoned plinian fall deposit indicates a normally stratified magma reservoir at about 9-12 km depth (Bertagnini *et al.*, 1998; Landi *et al.*, 1999). The magma chamber hosted a lower layer of homogeneous trachyte magma, and a more evolved upper layer of latite magma. Even though the eruptive product contains both phenocrysts (in equilibrium with the host magma) and xenocrysts (in disequilibrium with the host magma) the trace element distributions rule out any significant mixing, suggesting that the differentiation was a result of crystal fractionation (Landi *et al.*, 1999). Therefore, Landi *et al.* (1999) interpret the xenocrysts as material that crystallized at the magma chamber wall.

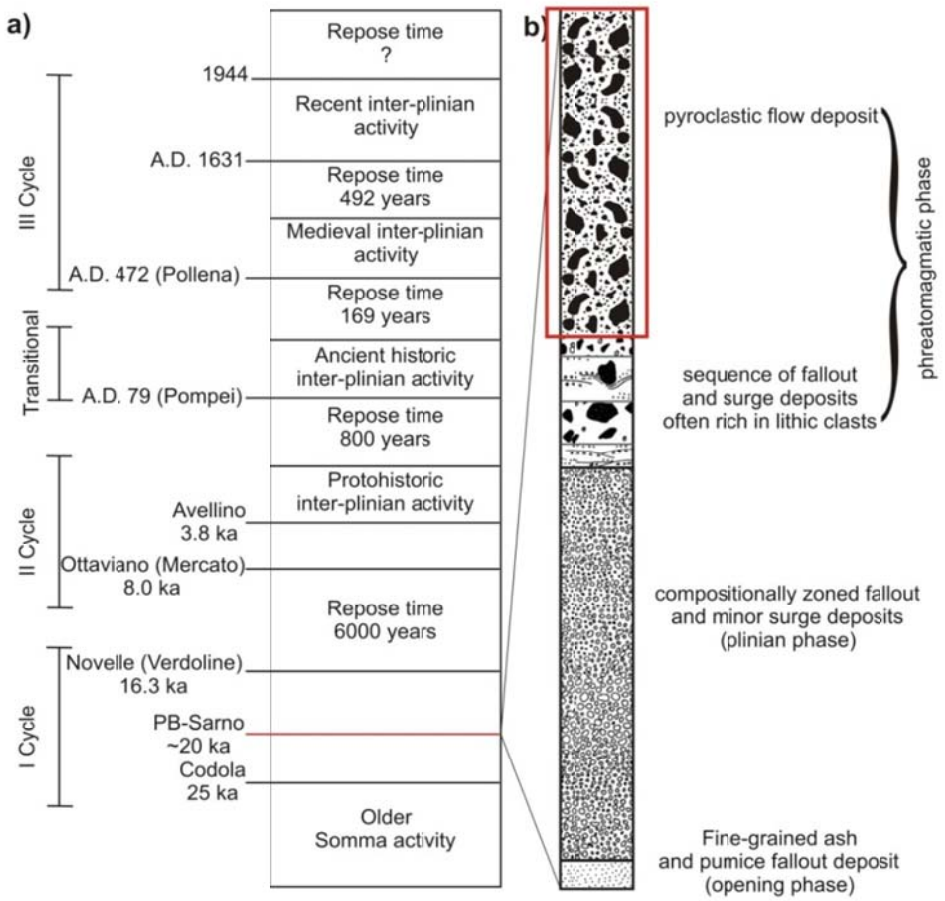

Figure 2. – a) Stratigraphy of volcanic activity of Mt. Somma-Vesuvius, modified from Piochi *et al.* (2006b). b) Schematic stratigraphic column of the Sarno (PB) eruptive products, adapted from Bertagnini *et al.* (1998). The rectangular red box near the top of the expanded column on the right indicates the portion of the unit that contains the nodules.

3. Material and methods

3.1. Sampling location

As mentioned in the introduction, this study was originally focused on nodules from the plinian eruptions of Mt. Somma-Vesuvius. Nodule samples from Avellino, Pompei, Pollena, the AD 1631 and 1944 eruptions were already available (collected by De Vivo and his coworkers in 2004). Lithic fragments-rich layers from the other three plinian and subplinian eruptions, *i.e.,* Sarno (PB), Novelle (Verdoline) and Ottaviano (Mercato) eruptions were previously reported in the literature (*e.g.*, Cioni et al., 2003; Rolandi et al., 1993b). Therefore, we expected to find nodules in the eruption products of these three older eruptions. Sampling was carried out with the help of Prof. Paola Petrosino (University of Naples "Federico II") and Ph.D. candidate Daniele Redi (University of Naples "Federico II").

We chose the Traianello quarry (Fig. 3; 40° 51' 33" N; 014° 27' 03" E), located at the NE slope of Mt. Somma, which has good outcrops of the older, prehistoric eruptions (Fig. 4), even though the quarry has been abandoned and has been partially filled. In this quarry the Sarno (PB) eruption is represented by a white pumice fall deposit (~15 cm) that abruptly changes into grey-dark grey (Fig. 5, ~25 cm). This outcrop was located in a hole in the centre of the quarry (Fig. 3). According to Bertagnini *et al.* (1998), this deposits belong to the plinian phase of the eruption. The thickness of the plinian phase is about 40 cm at this location, but it can reach 6.4 m (Bertagnini *et al.*, 1998). The fall deposit is underlain by ancient lava flows and overlain by the so called "upper member", which is a sequence of fallout, surge and flow beds (Bertagnini *et al.*, 1998). We did not find nodules in the plinian deposits, only in another outcrop, which revealed the "upper member" deposits. The nodules studied here were found in one of the final pyroclastic flow deposits (samples: NLM1). This pyroclastic flow deposit (Fig. 6) is about 1.5 m thick, and is an ungraded, unsorted lithic-rich lapilli bed. The lithic clasts are mainly fresh and oxidized, angular lava rocks and hypabyssal rocks (monzonite-diorite), ranging from a few cm to dm in size. We collected the latter for further study. The studied nodules are coarse-grained (up to 7 mm) igneous rocks with rounded to slightly angular equant to elongated shape. Nodule size varies from 1 to 10 cm. The layer is overlain by products of the Novelle (Verdoline) eruption. The lower boundary is buried.

We observed several outcrops of the Novelle (Verdoline) deposits (Fig. 4). The basal, thin pyroclastic fall deposit is overlain by alternating fall and surge deposits. The variation in grain size gives a pseudo-layering appearance to the deposit. However, the deposits contain lithic clasts, made up of lava rocks, not hypabyssal rocks. We examined two outcrops of the Ottaviano (Mercato) deposits in detail. The thick, white fall pumice layer contains mainly juvenile fragments. Upwards the amount of the lithic fragments increases giving a darker color to the bed. The layer containing lithic fragments (lava rocks) does not contain nodules. The fall deposit is overlain by a pyroclastic flow deposit from the same eruption. The grain size of the deposit decreases towards the southwest, which can be explained by the pyroclastics with larger grain size and higher thickness (10 m) being deposited in the valley, while the thinner, smaller grain-sized beds were deposited along the flank of the valley (Petrosino, oral communication).

The white Avellino fall deposit can be observed above the Ottaviano (Mercato) eruption products. The Avellino deposit consists of white pumice, but the outcrop could not be reached, therefore we were

unable to examine it in detail. The paleosols between the different eruptions represent the long repose time between the plinian eruptions.

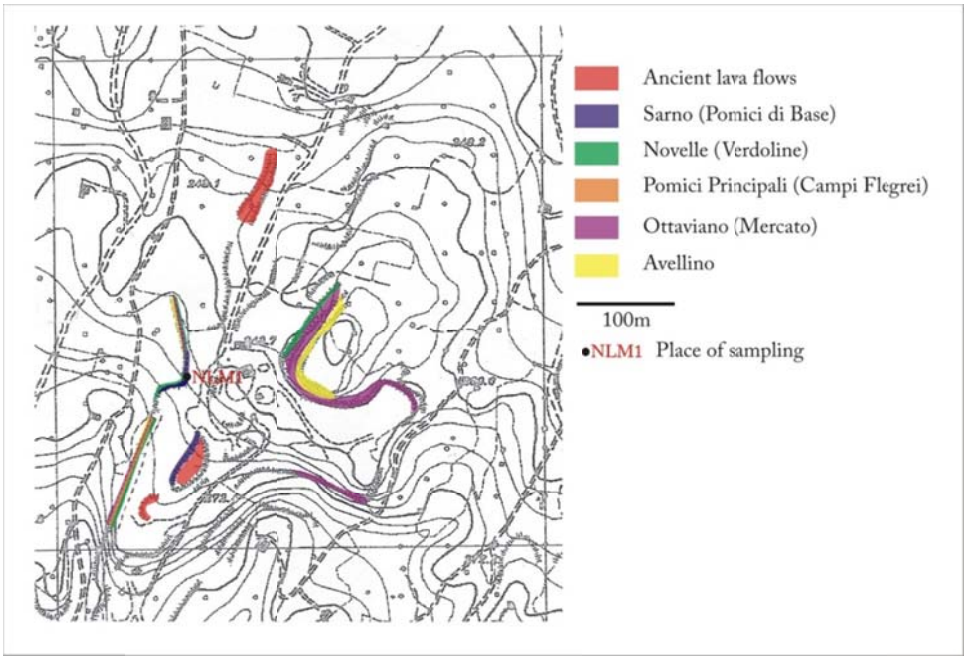

Figure 3. – Map of the geologic formations observed in the Traianello quarry (NE slope of Mt. Somma). 1:5000 topographic map by Italian National Cartography. The location of the quarry is shown in Klébesz et al. (2012).

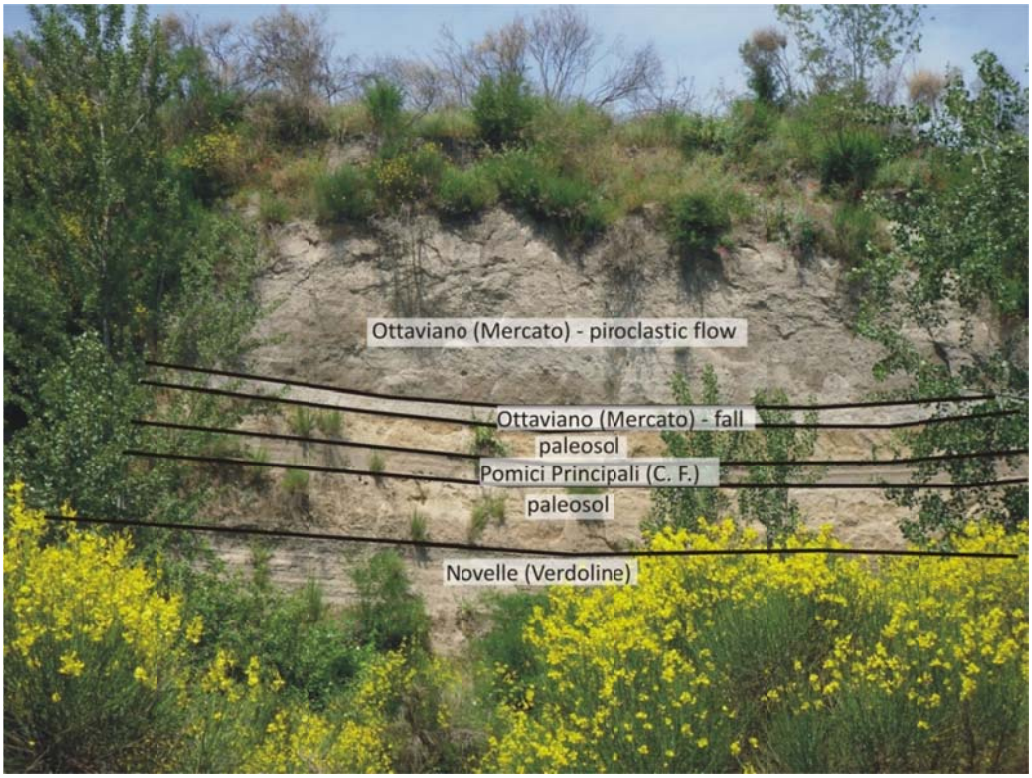

Figure 4. – Stratigraphic section of the observed formations in the Traianello quarry.

Figure 5. – Outcrop of pumice beds deposited during the plinian phase of the Sarno (PB) eruption (40°51'28"N;014°27'00"E).

Figure 6. – Outcrop of the pyroclastic flow beds deposited during the phreatomagmatic phase of the Sarno (PB) eruption (40°51'30"N;014°26'59" E).

3.2. Sample preparation for further studies

A sub-set of the collected nodules was selected to assure that all different types collected were represented, and these were cut into two pieces, and thin sections were prepared from one of the halves. Based on examination of the thin sections, some of the collected samples were determined to be effusive rocks, which were excluded from further studies. Four pieces (NLM1-1a,-1b,-1c,-1d) were coarse grained igneous rocks. The other half of these four rocks was gently crushed in a mortar and the resulting material was sieved to extract the ≤2 mm grain fraction. Using a binocular microscope, clinopyroxene, olivine and feldspar crystals were hand-picked from NLM1-1a, clinopyroxene crystals were selected from NLM1-1b and -1c, and amphibole crystals were collected from NLM1-1d. The selected crystals were mounted on glass rods (2.5 mm in diameter) and doubly polished individually following the method described by Thomas and Bodnar (2002).

When completed, the doubly polished crystals were removed from the glass rods by dissolving the glue in acetone and they were examined under the microscope to select crystals suitable for further study. Several crystals contained too many crystallized melt and/or solid inclusions and melt pockets, or they did not contain any, or they were heavily fractured, making them unusable. These unsuitable crystals included all of the clinopyroxene crystals from sample NLM1-1b and-1c, all of the olivines and feldspars and most of the clinopyroxenes from sample NLM1-1a, and some of the amphiboles from

sample NLM1-1d. The useable polished crystals, including the MI, were photographed under the microscope, hence providing a detailed map of the crystals. Unexposed and unhomogenized MI in some of the clinopyroxene crystals and in all of the amphibole crystals were analyzed (see chapter 2.3). These crystals were mounted in epoxy for analysis. Most of the clinopyroxene crystals were removed from the glass rods and individual crystals were heated in the Linkam TS1400 X-Y heating stage to homogenize the MI before analysis (see chapter 2.4.).

After the homogenization processes the crystals were individually mounted in epoxy and polished until the MI was exposed. This mounting method is preferable over the one described by Thomas and Bodnar (2002), because it does not require acetone based solvent which could be trapped in the micro fractures and potentially leading to carbon contamination. Rather than dissolving the glue after polishing, the crystals were removed from the epoxy using a hot pin (*e.g.*, soldering-iron). Carbon based polishing material was avoided, especially during the last polishing cycle (1 or 0.3 µm), when alumina powder was used in order to prevent carbon contamination. After the crystals were removed from the epoxy, they were cleaned in distilled water and then mounted in a one-inch diameter indium probe mount. An indium mount is used to prevent H_2O/CO_2 contamination from epoxy at the high vacuum conditions of the SIMS. The mounts were gold coated in preparation for SIMS analysis. A 5 nm evaporative gold coating was applied for the Scanning Electron Microscope (SEM) and for EPMA, and a 30 nm thick sputtered gold coating was applied for SIMS.

3.3. Analyses of crystallized (non-homogenized) MI by LA-ICP-MS

If MI are glassy as found, all is necessary before analysis to determine the major, trace and volatile composition by various methods (*e.g.*, EPMA, SIMS, FTIR) is to expose the MI on the crystal surface by polishing. Crystallized or partially devitrified MI cannot be analyzed by methods such as EPMA, SIMS or FTIR without homogenizing the MI first. However, Halter *et al.* (2002) developed an alternative method to determine the major and trace element composition of crystallized MI by LA-ICP-MS. This method does not require heating and homogenization of the sample, therefore complications (*e.g.*, compositional changes caused by non-ideal heating rate, Fe^{2+} diffusion; Danyushevsky et al., 2002) associated with laboratory heating can be avoided. An additional benefit of the method of Halter *et al.* (2002) is that MI do not have to be exposed at the surface. MI located as much as 100 µm beneath the surface can be analyzed by this method; therefore several MI at different depths can be analyzed within the same MIA. In addition, MI can be studied in minerals which are not commonly used in MI studies, such as amphibole (Halter et al., 2004). Homogenization of the crystallized MI is not an option for hydrous minerals because the host amphibole would be affected. The drawback of the method is that certain elements (*e.g.*, volatile elements) cannot be analyzed. Because the Halter *et al.* (2002) method is destructive, bubbles in the MI were analyzed by Raman Spectroscopy for CO_2 and H_2O before the LA-ICP-MS analyses, but no volatiles were detected.

With the method of Halter et al. (2002) the MI and its host are ablated together, hence generating a mixed LA-ICP-MS signal. In order to determine the MI/ablated host ratio (x) and to subtract the amount of host from the mixed signal, the concentration of one element in both the host and the MI must be known. Halter *et al.* (2002) tested several different internal standards (*e.g.*, constant element, constant

element ratios, constant distribution coefficient of an element, determination of *x* based on volume measurements) through which the composition of the MI can be determined.

In this study 40 unexposed inclusions in 5 clinopyroxene crystals (NLM1-1a), and 40 inclusions in 9 amphibole crystals (NLM1-1d) were analyzed by LA-ICP-MS at Virginia Tech (Blacksburg, VA, USA). Details of run conditions are reported in Table 1. The uncertainties are estimated to be 2-4 % relative (Norman *et al.*, 1996). The pit size was selected to be slightly larger than the inclusion diameter for each inclusion. During the ablation, the transition from the clinopyroxene to the MI and then back into the host crystal was determined by monitoring elements that are incompatible with respect to the clinopyroxene (*e.g.* K, Ba). Then, during data reduction, these elements were used to determine the portion of the signal that represented the inclusions. The software package AMS (Mutchler *et al.*, 2008) was used to reduce the mixed LA-ICP-MS signals (MI + ablated host), and to quantify the chemical composition of the MI according to the method of Halter *et al.* (2002). Only those data for which *x* (the MI/ablated host ratio) was ≥0.2 were used. During the data reduction of the MI in clinopyroxene crystals, a value of Al_2O_3=18 wt. % was assumed for the internal standard and the compositions were normalized to 100 % (both for MI and host). Although the Al content varies somewhat (15.2 to 19.8 wt. %) during the early history (megacycle I and earlier) of Mt. Somma (Ayuso *et al.*, 1998; Landi *et al.*, 1999; Paone, 2006), we chose 18 wt. % as an internal standard because the average of all values reported (Ayuso *et al.*, 1998; Landi *et al.*, 1999; Paone, 2006) is 17.65 wt. %. The absolute concentration assumed for the Al_2O_3 does not significantly affect the result, especially for trace elements, as long as the real A_2O_3 concentration does not vary significantly from 18 wt. %. For example, the Sr value obtained for a MI assuming 18 wt. % Al_2O_3 as the internal standard is 918 ppm. If we assume an Al_2O_3 concentration of 15.2 wt. % as the internal standard, the calculated Sr concentration would be 773 ppm instead of 918 ppm. If we assume an Al_2O_3 concentration of 19.8 wt. % as the internal standard, the amount of Sr is predicted to be 1007 ppm. Thus, even using the most extreme values for the Al_2O_3 concentration reported in the literature only leads to a range in Sr concentration of 773-1007 ppm, an insignificant variation when using trace elements as petrogenetic indicators. In addition, because trace elements are displayed on "spider diagrams", interpretations are generally based on trends in the data and the absolute concentrations are less important. If an incorrect concentration for the internal standard were used, all trends would be affected to the same extent and the trace element pattern would be unchanged.

While the percent variation caused by the different internal standards will be the same for the major elements as for the trace elements, the absolute variations are larger and may affect how we classify the melt composition. For example, if the Al_2O_3 concentration of the melt is assumed to be 18 wt. %, the predicted SiO_2 content of the MI would be 48.9 wt. %. Using the most extreme values for Al_2O_3 concentration reported in the literature results in a predicted range in SiO_2 of 41.14 to 53.6 wt. %. Although this is a relatively large variation in SiO_2, the trends in major element abundances remain the same, and the data points are simply shifted along the x and y axes.

In the case of the MI in amphiboles, an Al_2O_3 concentration of 18 wt. % in the melt was also used as the internal standard. In several MI, however using this value produced negative x values, or values exceeding 1, neither of which is possible. These data were not considered further. The MI compositions were normalized to 100 %, while the amphibole compositions were normalized to 98 % during the data reduction.

3.4. Heating experiments of selected MI

As mentioned above, crystallized MI can be analyzed by LA-ICP-MS without the need for homogenization, but the volatile composition cannot be determined. One of our primary goals was to determine the volatile contents of MI. Therefore, heating experiments were carried out in the Linkam TS1400 XY heating stage on 67 clinopyroxene crystals from sample NLM1-1a. The specifications of the heating stage and the details of a heating experiment are discussed in details in our paper (Esposito et al., 2012).

Heating experiments were conducted during five analytical sessions. Before each session, the stage was first calibrated as described by Esposito *et al.* (2012). Eight (8) clinopyroxene crystals were tested in the first run, 11 in the second run, 8 in the third run, 11 in the fourth run and 31 in the fifth run, and generally only one MI in each crystal was monitored during heating. The heating rates are summarized in Table 2. In every crystal one MI was preselected and observed and photographed during the experiment. Examples of phase changes in MI during heating runs are shown in Esposito *et al.* (2012) and in Fig. 7. Heating was continued until the observed inclusion homogenized, then the sample was quenched. After the experiment was completed, the crystal was removed from the sample holder slide with a razor blade. In some cases the crystals broke or were completely damaged during sample removal, if some of the external glass in the sample melted and caused the sample to be fused to the slide during quenching.

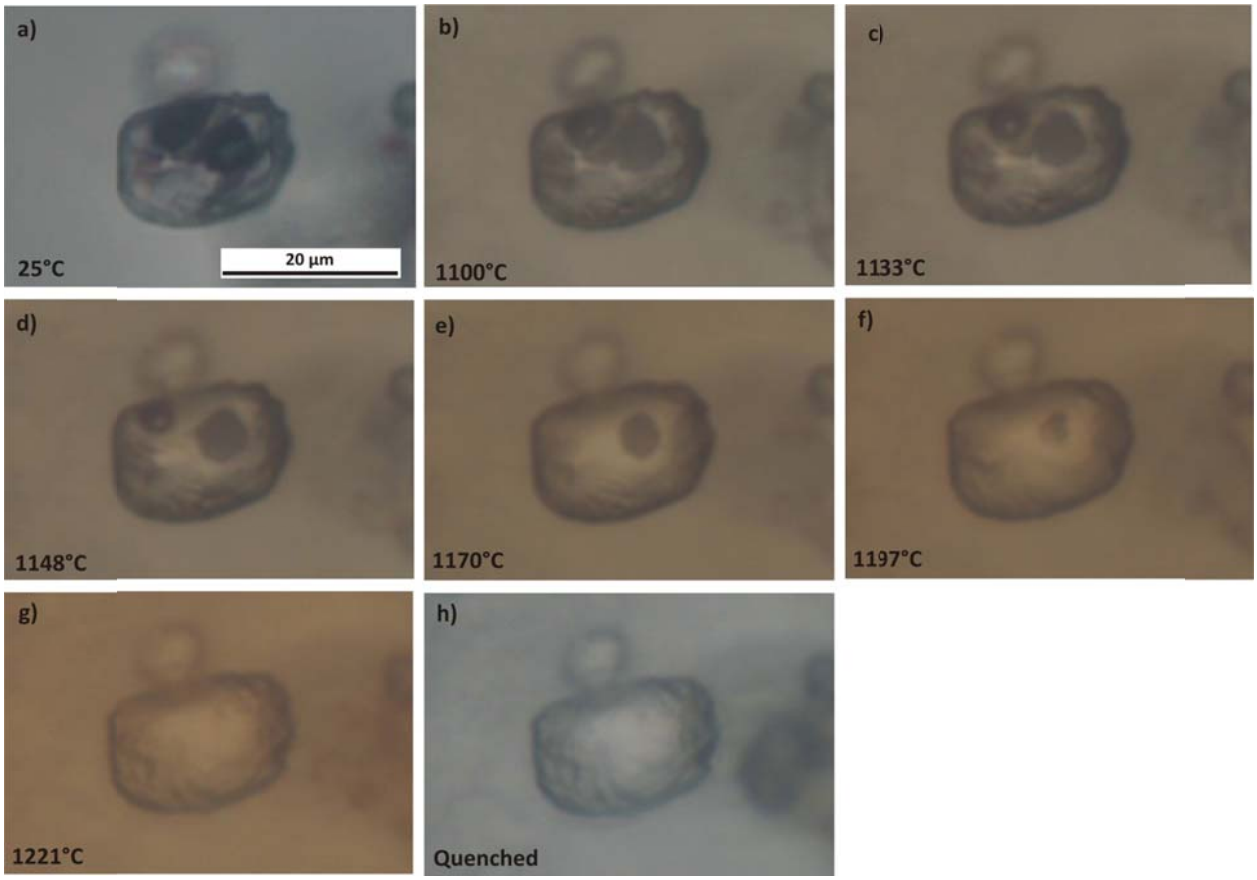

Figure 7. (Above) – Heating experiment on a MI in clinopyroxene from sample NLM1-1a. a) At room temperature the MI is crystallized, a bubble and some daughter crystals can be observed. b) Melting starts at around 1100 °C. c) The melting is more advanced, the yellowish-brown daughter mineral (most likely mica) starts to melt at around 1130 °C. d) An about 1150 °C the (mica?) daughter mineral disappears, and the size of the bubble is considerably smaller. e) At ~1170 °C the bubble dissolves into the melt, and only one solid phase can be observed. f) A slightly less than 1200 °C the last solid phase is barely visible. g) After the MI homogenized at ~1220 °C, h) it was quenched to a homogeneous glass.

3.5. Analyses of homogenized MI from sample NLM1-1a

Two mount were prepared from the clinopyroxene crystals hosting the homogenized MI. The first mount contained 10 clinopyroxene crystals from the first four sets of heating experiments, the second mount contained 30 crystals from the fifth heating session. The remainders of the crystals from the heating experiments were damaged or lost during sample preparation. The first mount was gold coated for SIMS studies, and 15 MI were large enough (>20µm) to be analyzed for volatiles (H_2O, CO_2, F, Cl, and S). After the gold coating was removed, the mount was carbon coated for SEM and EPMA analysis, and 27 MI were analyzed for major elements. Subsequently, 29 of these MI were analyzed by LA-ICP-MS for trace elements. The second mount was first gold coated for SEM and EPMA, and 102 MI were analyzed. Then, the thin gold coat was removed and it was gold coated again with a different thickness for SIMS analysis. Out of >100 MI, only 17 MI were large enough to be analyzed by SIMS. Finally, the gold coating was removed again, and 46 MI that were large enough were analyzed for trace elements by LA-ICP-MS.

MI and adjacent clinopyroxene host were analyzed to determine the major element composition using a Cameca SX-50 electron microprobe at Virginia Tech. An accelerating voltage of 15 kV was used with a beam current of 10 nA and 5µm diameter defocused beam for MI analyses, and the same voltage with a beam current of 20 nA and focused beam was used for host analyses. For each MI, the host phase two spots located >15 µm from the glass/host interface were analyzed. If the two analyses showed large variability in the major element abundances, a third analysis was carried out. Every MI that was ≥10 µm and exposed on the surface was analyzed, regardless of whether petrographic information was available or not (*i.e.*, whether or not the MI had been previously "targeted" for analysis during the initial petrographic examination). The one sigma relative error was always less than 5 %, and usually ≤1 %, if the concentration of the element is >1 wt. %.

MI were analyzed for volatile element concentration using the IMS 7f ion probe at Virginia Tech. Analyses were performed using $^{133}Cs^{+}$ as the source, with a current between 1 and 1.6 nA. A 30 µm x 30 µm spot was rastered within or around the glass for 240 s to clean the surface before analysis. Then, a 15 µm x 15 µm spot within the rastered area was analyzed 15 times in depth profile mode. Volatile contents were related to the ratio of the isotope (mass) of interest ($^{16}O^{1}H$, ^{12}C, ^{19}F, ^{32}S or ^{35}Cl) to ^{30}Si. The four standard glasses that were used to calibrate the SIMS are natural glasses (EN11346D-2, ALV1649-3, GL07D52-5 and ALV1654-3; Helo *et al.*, 2011). The measured element ratios (*e.g.*, $^{12}C/^{30}Si$) were plotted against the known volatile concentration (*e.g.*, CO_2) of the standard glasses to define the calibration curve. Relative precision for volatiles by SIMS is considered to be <10 % relative for all the volatiles analyzed, based on repeated analyses of glass standards. In addition, it is important to note, that in

some cases the volatile concentration (usually F, sometimes Cl too) of the sample was too high and saturated the Faraday cup and the concentrations of those volatile species could not be determined.

MI and adjacent clinopyroxene host were analyzed by LA-ICP-MS to determine their trace element abundances. Run conditions are summarized in Table 1. The uncertainties are estimated to be 2-4% relative (Norman *et al.*, 1996). The analytical spot size was selected to be slightly smaller than the inclusion. Background signal was collected for 60 s before the laser was turned on. In this case only MI exposed on the surface were analyzed. During the analyses, the transition from the MI into the host crystal (after ablating through the entire MI) was determined by monitoring elements that are incompatible whit respect to the clinopyroxene (*e.g.*, K, Ba). Then, during data reduction, only the signal from the MI was included. The software package AMS (Mutchler *et al.*, 2008) was used to reduce the data from the LA-ICP-MS. The totals of the EPMA were close to 100 % and low volatile contents were detected by SIMS, therefore the data was normalized to 100 % for both the clinopyroxene host and the MI. As discussed above (Chapter 2.3), this normalization does not cause significant variations in the estimated trace element concentrations.

3.6. Analyses of the minerals in the rocks

Thin sections prepared from samples NLM1-1a,-1b,-1c,-1d were carbon coated and mapped by SEM. Then, the minerals were analyzed by Cameca SX50 (EPMA) at Virginia Tech to determine their major element chemistry. An accelerating voltage of 15 kV was used with a beam current of 10 nA and defocused 5 µm defocused beam for feldspar analyses, and the same voltage with a beam current of 20 nA and a focused beam was used for olivine, clinopyroxene, mica, apatite and amphibole analyses. The one sigma relative error was always ≤5 %, and usually ≤1 %, if the concentration of the element is >1 wt. %.

Following SEM/EPMA analyses, the thin sections were cut into pieces, and the minerals were analyzed for trace elements by LA-ICP-MS at Virginia Tech. Attempts were made to analyze the same mineral grains that were analyzed by EPMA, but it was not always possible to do so. Analytical conditions were the same as for the MI analyses. The spot size was chosen to be as large as possible without including heterogeneities (*e.g.*, inclusions) within the crystal. This approach was particularly important in the case of oxide phases, which are heterogeneous, and the spot size had to be large enough to give representative (bulk composition) results. The software package AMS (Mutchler *et al.*, 2008) was used to reduce the LA-ICP-MS signals. The compositions of olivine, feldspar, clinopyroxene and heterogeneous oxides and groundmass were normalized to 100 %. Owing to the volatile contents of mica and amphibole, their compositions were normalized to 96 % and 98 %, respectively. Apatite contains volatile elements and P, which cannot be analyzed by LA-ICP-MS, and apatite analyses were normalized to 56 %.

4. Results

4.1. Petrography

Thin sections of the nodules were examined by petrographic microscope and by SEM for additional details. As mentioned above, many of the samples were found to be lava rocks during initial examination, and these are not discussed here in detail. The remaining four samples have similar textural characteristics and were divided into two groups: Type A – nodules NLM1-1a, -1b, 1c and Type B – nodule NLM1-1d.

Type A nodules have a coarse porphyrogranular texture (Fig. 8a-b), *i.e.*, large "phenocrysts"(up to 7 mm) in a coarse-grained matrix. The "phenocrysts" are euhedral-subhedral clinopyroxene and olivine crystals. The clinopyroxene is colorless-light green colored in transmitted light. In rare cases the clinopyroxene phenocrysts show some slight reverse, normal or oscillatory zoning, and in most cases the zoning can only be observed by SEM with high contrast. Also, it is important to note that resorption surfaces within the crystals are rare, and the contacts between the zones are usually straight. This feature is more common in nodules NLM1-1b and -1c. The olivine is colorless and highly fractured. Mica overgrowths around olivine phenocrysts are common. The groundmass consists of K-feldspar, with less plagioclase, mica, clinopyroxene and accessory apatite and Fe-Ti-phases. The feldspars show a euhedral-subhedral, tabular shape and sometimes show compositional zoning on SEM images (Fig. 8f). Mica and clinopyroxene are subhedral-anhedral, often with irregular edges and angular embayments. Occasionally, this feature is observed in clinopyroxene phenocrysts also. The apatite and oxide crystals are euhedral. The oxide crystals are inhomogeneous, they have dissolution texture; *i.e.*, oriented ilmenite lamellae in magnetite crystals (Fig. 8e).

A common feature in all samples is the irregular and vesicular intergrowth of alkali feldspar and plagioclase, and occasionally clinopyroxene, mica, apatite and oxide phases floating in a vesicular feldspar matrix (Fig. 8c-d). The grain size in the aggregates is much smaller than in the matrix and the crystals are usually anhedral. The most distinctive feature is the appearance of abundant tiny vesicles. The size of the aggregates varies from about 100 µm up to a few mm. We interpret these features to represent crystallized melt pockets.

Type B nodule (NLM1-1d) also show a coarse-grained porphyrogranular texture (Fig. 9a). The grain size is slightly smaller than in Type A nodules. The phenocrysts are subhedral-anhedral amphiboles (Fig. 9b) that have light to dark brown color in transmitted light. The edges of the amphibole phenocysts are very jagged (irregular embayments) and a reaction rim consisting of mica, clinopyroxene and feldspar is often observed around the amphiboles (Fig. 9c). The groundmass consists of mainly K-feldspar and another colorless phase that we could not identify, not even after chemical analysis. The contact of the large tabular feldspar and this unknown phase is most commonly linear, or slightly irregular, but with angular edges. The unidentified phase and the K-feldspar also form irregular intergrowths, and the texture is much more vesicular and the grain size is much smaller, compared to the groundmass where both phases have a tabular habit and the grain boundaries are more regular (Fig. 9d). Analogous to the Type A nodules, we interpreted these features to represent crystallized melt pockets. The size of the crystallized melt pockets is up to a few hundred micrometers. Given the appearance of this unknown phase it appears to be a primary phase, or one that has completely replaced some other primary phase.

The groundmass also contains green, subhedral clinopyroxene, mica and anhedral, accessory apatite and Fe-Ti-oxide. Small (≤100 µm), euhedral mica crystals that show strong, complex zoning on the SEM images are also observed in the melt pockets.

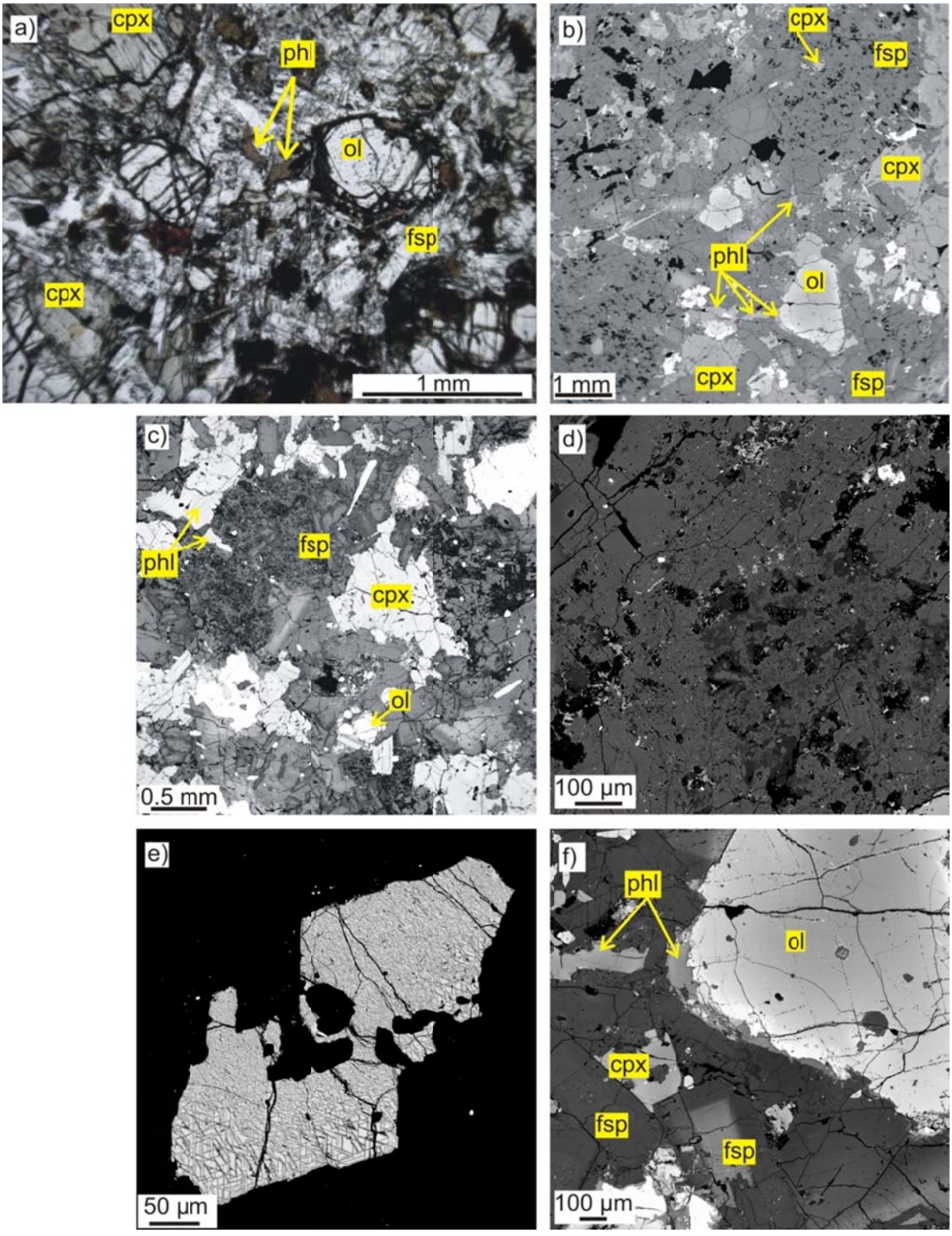

Figure 8. (Above) – a) Photomicrograph and b) SEM image showing the porphyrogranular texture of a Type A nodule (cpx – clinopyroxene, phl – phlogopite, ol – olivine, fsp – feldspar). SEM images of the crystallized melt pockets (see text for more details) with c) lower and d) higher magnification. Note the abrupt transition from tabular K-feldspar to vesicular, irregular K-feldspar and then to an intergrowth of K-feldspar and plagioclase. e) SEM image of the dissolution texture of a Fe-Ti-oxide crystal. f) Phlogopite overgrowth around an olivine phenocryst.

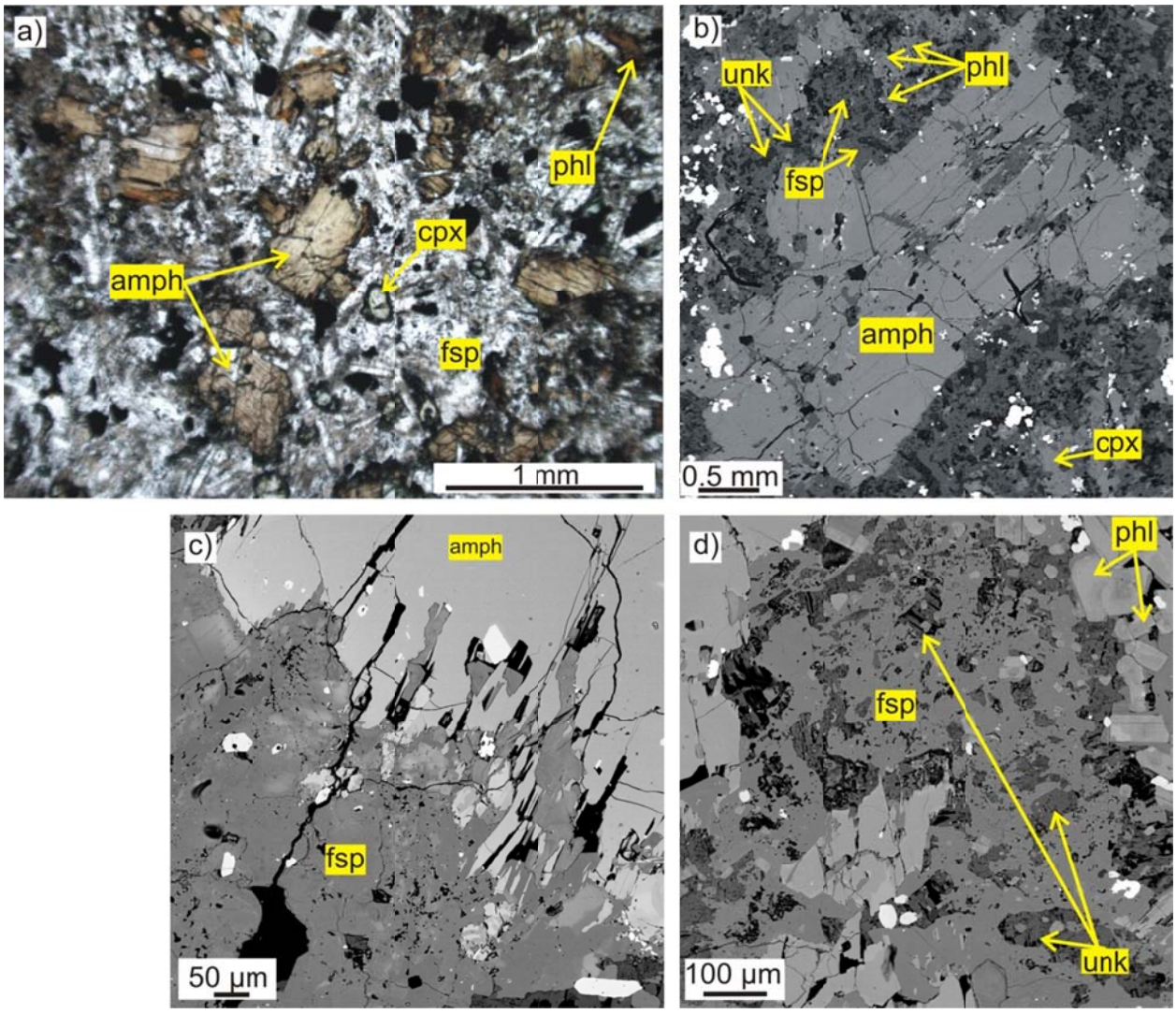

Figure 9. – a) Photomicrograph showing the porphyrogranular texture of Type B nodule. b) SEM image of an amphibole (amph) phenocryst floating in a crystallized matrix of K-feldspar (fsp), phlogopite (phl), clinopyroxene (cpx) and an unknown phase (unk). c) SEM image of the reaction rim around the amphibole, consisting of feldspar, phlogopite and clinopyroxene. d) High magnification SEM image of the vesicular, irregular intergrowth of K-feldspar and the unknown phase. Also note, that even though phlogopite crystals are small, they show complex compositional zoning.

4.2. Mineral chemistry

Clinopyroxene is present in both Type A and Type B nodules, but it is less common in Type B (NLM1-1d) and only appears in the groundmass. Significant differences can be recognized between the clinopyroxenes from the two types of nodules in major and trace element composition. There is some variation in the clinopyroxene compositions, but most can be classified as ferroan diopside based on the compositions obtained by EPMA (Table 2. in Klébesz et al., 2012 and Fig. 10). Slight differences can be observed between the compositions obtained by EPMA and LA-ICP-MS. The concentration obtained by LA-ICP-MS (Table 3.) for most of the elements is similar to the concentrations obtained by EPMA, except for CaO and SiO_2. The Ca concentration is underestimated while the Si concentration is slightly overestimated by LA-ICP-MS compared to the concentrations obtained by EPMA. The differences in these elements can lead to incorrect classification or false pressure/temperature estimates if the clinopyroxene used in thermobarometeric calculations.

Clinopyroxenes from Type B nodules are usually more ferroan and have slightly higher Ca-content compared to clinopyroxene from Type A nodules. Compositions of clinopyroxene from Type A and B nodules show different trends on an MgO *vs.* TiO_2 diagram (Fig. 11a). The Ti-content increases with decreasing Mg-content in clinopyroxenes from Type A nodules, but no trend is evident in Type B nodules. Similar trends can be recognized on the MgO *vs.* Al_2O_3 diagram (not plotted). CaO/Al_2O_3 ratios correlate positively with MgO content in sample NLM1-1a (Type A nodule), but in the other samples these values show wide variability, and no general trends can be observed (Fig. 11b). The trace element composition of clinopyroxene shows wide variability (Fig. 11d), but a general trend can be recognized on the MgO *vs.* trace elements plots. The trace element concentrations increase with decreasing MgO-content, except in the case of Cr and Ni, which decrease with decreasing MgO-content (Fig 11c). The largest compositional variation is observed in samples NLM1-1b and -1c, with smaller compositional ranges in NLM1-1a and -1d, for most elements. In general, clinopyroxene from Type B nodule (NLM1-1d) is more enriched in trace elements compared to those from Type A nodules (Fig. 11d). It is also important to note that in nodules NLM1-1b and -1c zoned clinopyroxenes are much more common than in nodule NLM1-1a. The wider compositional ranges and the zoning may indicate crystallization under open system conditions and/or crystallization from a heterogeneous magma. On the trace element variation diagram (Fig. 11d), averages of clinopyroxene crystallized from Vesuvius magma (Wood and Trigila, 2001) are also plotted for comparison. The trace element patterns of the clinopyroxenes from the nodules are consistent with a general trend for a clinopyroxene that crystallized from a melt.

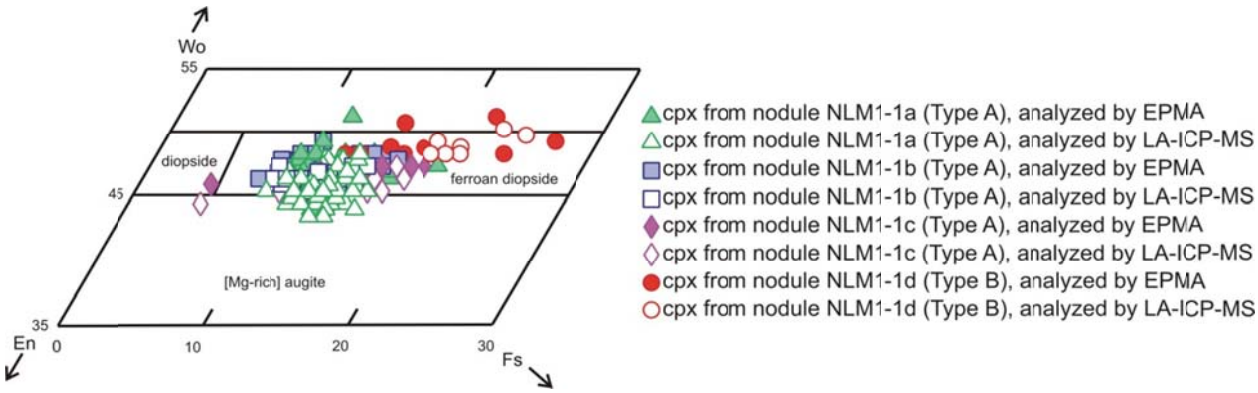

Figure 10. – Classification of the clinopyroxenes (cpx) from Type A and Type B nodules.

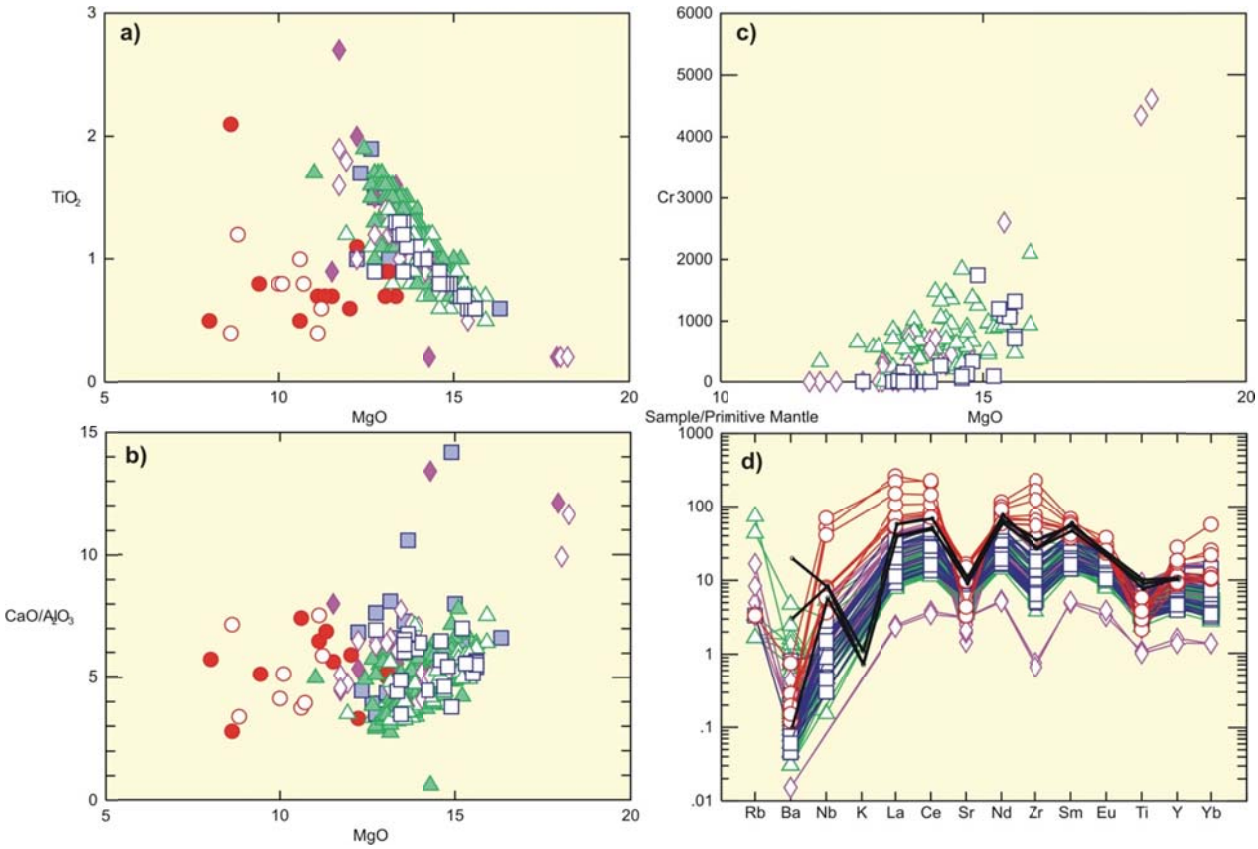

Figure 11. – Clinopyroxene compositions plotted on a) MgO *vs.* TiO2, b) MgO *vs.* CaO/Al_2O_3, c) MgO *vs.* Cr and d) primitive mantle (pyrolite, McDonough and Sun, 1995) normalized trace element variation diagrams. Symbols are as in Fig. 10. On d) the black lines represent average clinopyroxene compositions from Wood and Trigila (2001).

Olivine is observed only in Type A nodules. Olivine compositions (Table 2. in Klébesz et al., 2012) in samples NLM1-1a and -b range from Fo_{53} to Fo_{77} and from Fo_{58} to Fo_{66} in NLM1-1c. The olivines show normal zoning, with the Fe-content gradually increases towards the rim.

Amphibole occurs only in Type B nodule (NLM1-1a). Table 2. in Klébesz et al. (2012) and Table 4. here show the compositions of some analyzed amphiboles. Amphibole can be classified as

magnesiohastingsite based on its composition (Fig. 12.), according to the classification of Leake *et al.* (1997). Amphiboles sometimes show zoning, with the rim being more K-rich and Mg-poor than the core. The amphibole is F-rich (up to 4.8 wt. %) and Cl-rich (0.1 wt. %). While the F-content decreases with decreasing MgO-content, no correlation was observed between Cl and MgO within the analytical precision of the EPMA measurements. In some cases the sum of the analyzed volatiles is higher than the amount that can be accommodated in the structure according to the stoichiometric formula.

The trace element compositions of the amphiboles show significant variation (Fig. 13) but no general trend was recognized between MgO and the trace elements. The amphiboles can be divided into two groups, one with high Ti and Ba content, and the other with lower Ti and Ba content (Fig. 13). It is unclear whether these differences have a petrogenetic significance or are simply an artifact of the analytical method (LA-ICP-MS). It is important to note that amphiboles in one group were analyzed during a different analytical session than amphiboles in the other group, and the background signals differ in the different sessions.

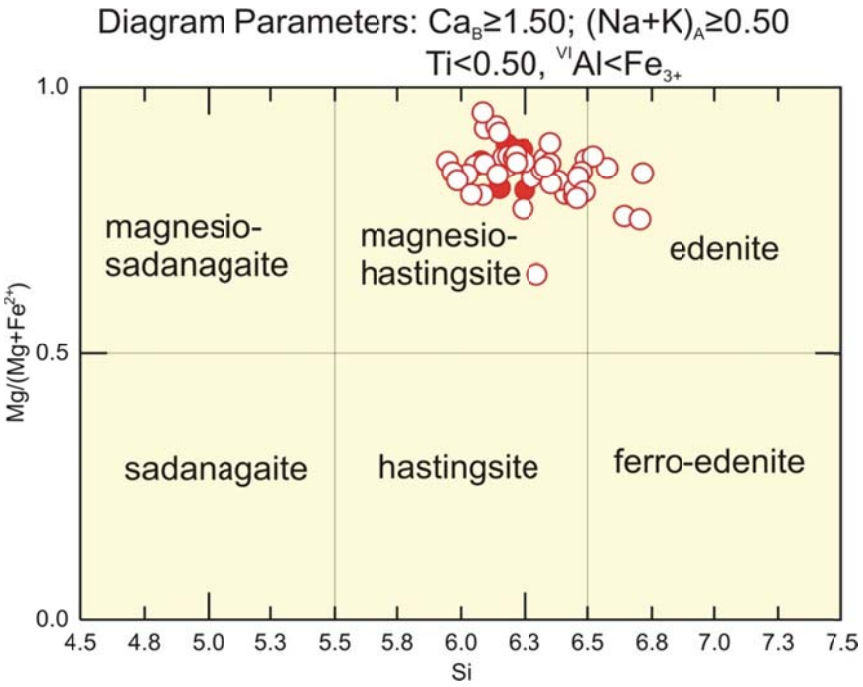

Figure 12. – Classification of the amphiboles from Type B nodule (NLM1-1d) according to the classification of Leake *et al.* (1997). Closed symbols are EPMA data, open symbols are LA-ICP-MS data.

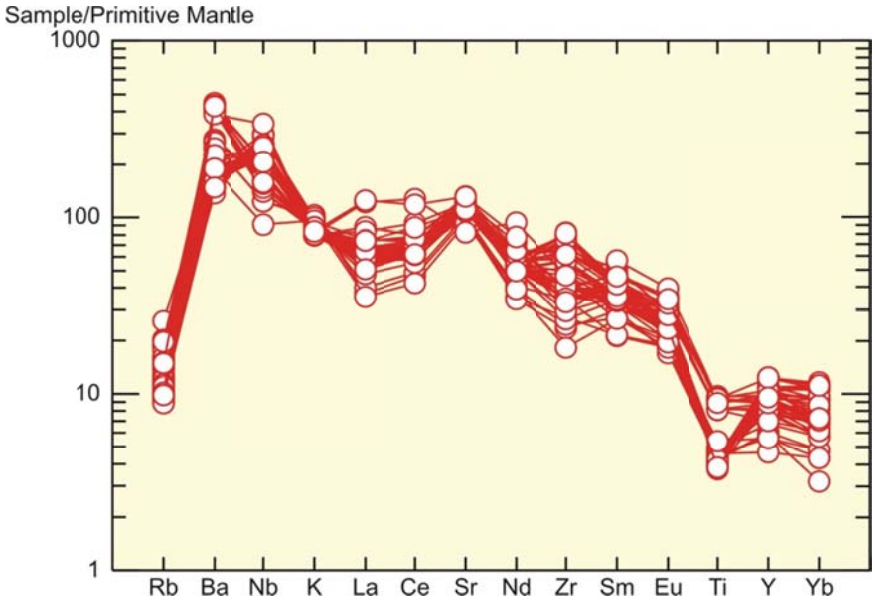

Figure 13. – Primitive mantle (pyrolite, McDonough and Sun, 1995) normalized trace element diagram of amphiboles from Type B nodule (NLM1-1d).

Feldspar is present in the groundmass in both types of nodules. The tabular feldspars in the groundmass of Type A nodules (NLM1-1a, -1b, -1c) are An-rich (An>50 mol%) plagioclase and K-feldspar (Table 5, Fig. 14). The K-feldspar sometime shows compositional zoning, with the core being Ba-rich (up to 6 wt. % BaO). The feldspars in Type B nodule are almost exclusively K-feldspar, usually with very low Na-content (less than 1wt. % NaO). Trace elements in the feldspars do not show large variations within each type of nodule (Fig. 15), but K-feldspar in Type B nodule (NLM1-1d) generally has a higher REE- and Sr-content than those in Type A nodules (Fig. 15a). Some interesting features were recognized by comparing the trace element distribution of the K-feldspar and the plagioclase. Both minerals have similar trace element distribution pattern. Plagioclase has a Sr, a LREE (La, Ce) and a Eu concentration similar to K-feldspar, or even slightly higher. K-feldspar usually has higher Rb and Ba concentration compared to feldspar from the same sample.

Feldspars in the crystallized melt pockets are irregular and usually are too small to be analyzed without including some of the surrounding material in the analytical volume, especially with LA-ICP-MS. Analyzed feldspars from the melt pockets have more sodic compositions than the tabular ones. However, in most cases the compositions plot in the feldspar immiscibility field on the feldspar ternary diagram, reflecting the fact that multiple crystals and/or glass were included in the analysis.

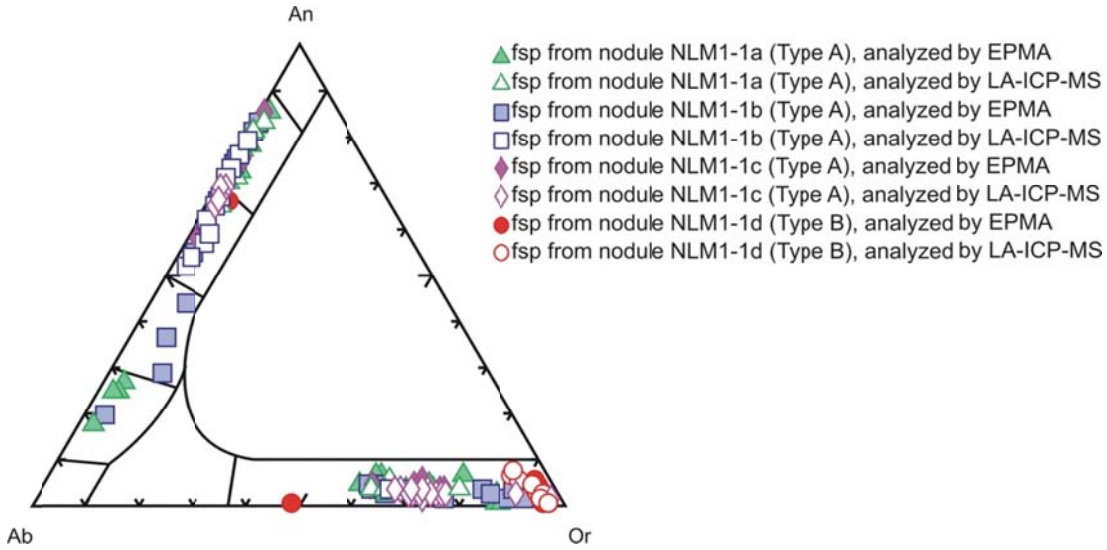

Figure 14. – Compositions of the feldspars (fsp) plotted on the Albite (Ab)-Anorthite (An)-Orthoclase (Or) ternary diagram.

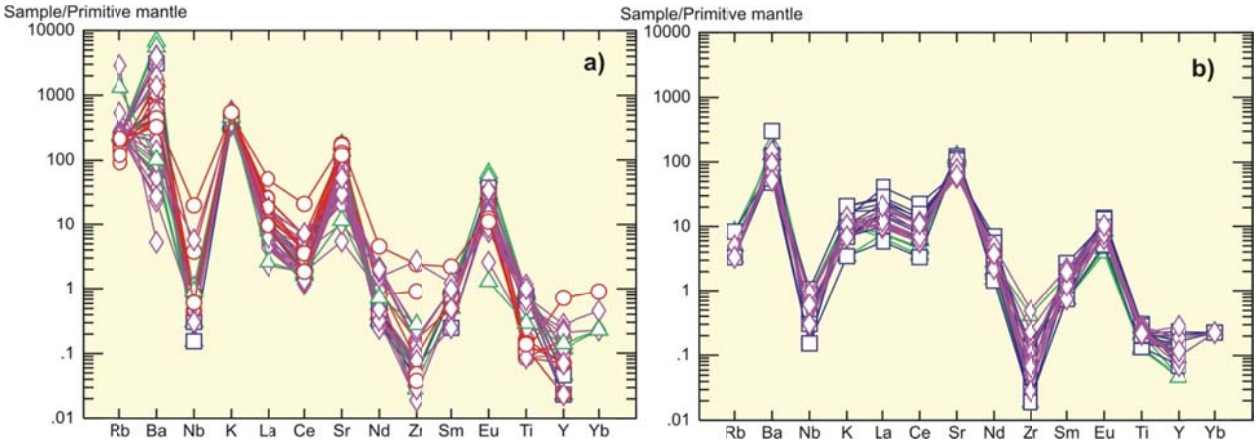

Figure 15. – Primitive mantle (pyrolite, McDonough and Sun, 1995) normalized trace element diagram of a) K-feldspar and b) plagioclase from the studied nodules. Samples are the same as in Fig. 14.

Mica appears in the groundmass in both types of nodules and has a high Mg-content and can be classified as biotite (Fig. 16). Biotite is less magnesian (more Fe-rich) in nodule NLM1-1a (Type A), while nodule NLM1-1d (Type B) usually contains less than 7 wt. % FeO (Table 6). In nodule NLM1-1a mica overgrowths around olivine have also been analyzed. These micas have higher Mg-content than those in the groundmass, indicating that they probably formed earlier. Mica in both types of nodules is very F-rich. In type A nodules the F-content of the mica is usually 2-4 wt. %, but it can be as high as 6.5 wt. %. In type B nodule the F-content of the mica is higher than in type A, at ~7-8 wt. %. The trace element composition of the micas in the two types of nodules is slightly different (Fig. 17.). Mica in Type B nodule (NLM1-1d) is more enriched in Ba and Sr, and slightly more enriched in La and Ce, but less enriched in Ti, Zr than those in Type A nodules. Also the trace element compositions of the micas show a wider range in Type A nodules, but no systematic variation with respect to the MgO-content can be recognized.

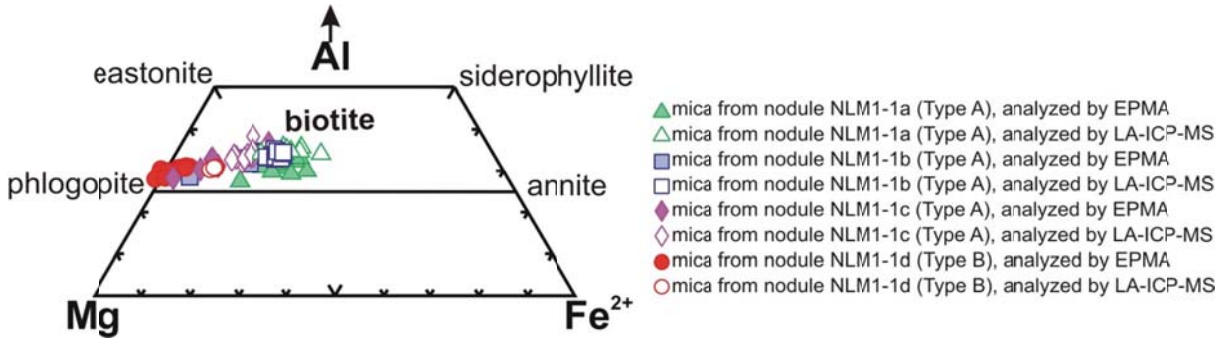

Figure 16. – Compositions of mica from Type A and Type B nodules.

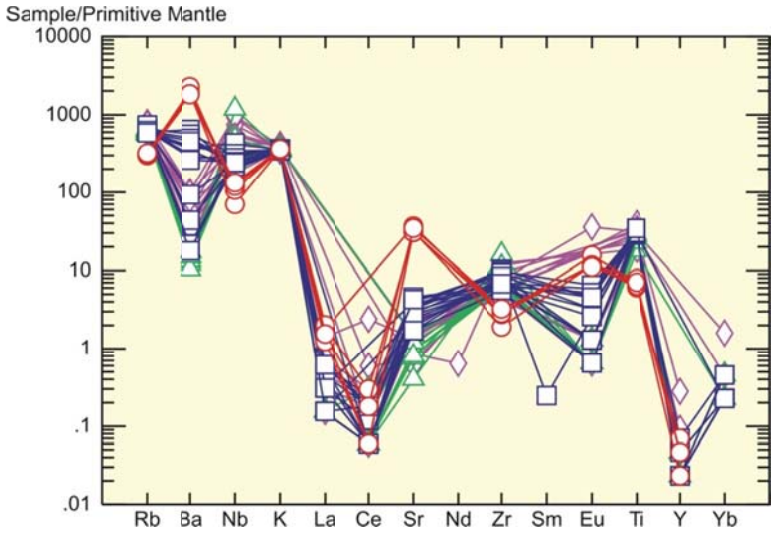

Figure 17. – Primitive mantle (pyrolite, McDonough and Sun, 1995) normalized trace element distribution diagram of micas from the studied nodules. Symbols are as on Fig. 16.

An ***unknown phase*** was observed in the groundmass of Type B nodule (NLM1-1d). The phase is colorless in transmitted light. On SEM images it is darker than amphibole or K-feldspar, suggesting a lower average atomic mass. During the analysis the electron beam damages the phase by leaving a large hole with a wide aura behind. The composition of this phase is reported in Table 2. in Klébesz et al. (2012). The low analytical total and the low F- and Cl-content suggest that it contains some other volatile, most likely H_2O. Data suggest that it is some kind of Ca-K-Al-silicate, but its composition does not correspond to any known mineral. Based on its occurrence it might be a primary phase, or a secondary phase that completely replaced an earlier primary phase. Owing to its very high H_2O-content, the latter interpretation is more likely.

Apatite appears in both types of nodules as an accessory mineral. It has a high F-content, up to 7.3 wt. %, which is higher than what can be accommodated in the stoichiometric formula. No significant differences were recognized between the apatites from the two different types of nodules (Table 2. in Klébesz et al., 2012).

Fe-Ti-oxide also occurs as an accessory mineral in both types of nodules. Due to its inhomogeneity it was analyzed only by LA-ICP-MS using a large beam diameter in an attempt to obtain the bulk composition of the phase. In both types of nodules the oxides are Ti-magnetites, but they contain much less Ti in Type B

nodule (NLM1-1d). TiO_2-content ranges of 20-27 wt. %, 14-24 wt. % and 3-6 wt. % were observed in NLM1-1a, -1b and -1c, and -1d, respectively (Table 7).

4.3. MI in Type A nodules

As mentioned above three rock samples were classified as Type A nodules, but only nodule NLM1-1a was suitable for MI studies due to sample preparation difficulties. In all three samples some of the feldspars in the groundmass contained clouds of tiny MI and some of the olivine crystals contain trails of tiny inclusions. MI in these minerals, however, were not suitable for detailed studies, owing to the small size of the inclusions and the highly fractured nature of the host. MI were only studied in clinopyroxene from nodule NLM1-1a.

MI in clinopyroxene from NLM1-1a are either randomly distributed in the crystals or occur along a growth zone and are, therefore, interpreted to be primary. However, in most crystals there are so many MI that it is impossible to define an MIA (Fig. 18a). The MI are usually 20-30 µm in maximum dimension, but range from about 5 to 60 µm, and have rounded to angular shape. They are partially to completely crystallized. Two groups of MI can be distinguished based on petrography (Fig. 18b). Type I MI are more common, representing 70-80% of total MI. Type I MI contain mica, Fe-Ti-oxide minerals and/or dark green spinel, clinopyroxene, feldspar and a vapor bubble. Volatiles (CO_2, H_2O) were not detected in the bubbles by Raman analysis (see Esposito *et al.*, 2011). Type II inclusions are generally lighter in color when observed in transmitted light and contain subhedral feldspar and/or glass and several black (opaque?) phases, most of which are confirmed to be oxides by SEM analysis. Some of the opaque-appearing phases that are below the surface may be tiny vapor bubbles. The two types of MI are spatially associated, *i.e.*, they appear adjacent to each other in the crystal.

Single phase elongated angular inclusions (Fig. 18c) and planes of two-phase irregularly-shaped inclusions (Fig. 18d) were also observed. These inclusions were originally thought to be FI, and were briefly examined. No phase change could be observed during slight cooling from room temperature or during heating to magmatic temperatures. Also volatile species were not detected in the inclusions by Raman spectroscopy, therefore these inclusions were not studied further and their composition and origin are currently unknown.

The homogenization temperatures, more precisely the quenching temperature (T_q), of MI in clinopyroxene from Type A nodule (NLM1-1a) cluster between 1202-1256 °C, but mostly between 1220-1250 °C. The quenching temperature does not necessarily reflect the trapping temperature (T_t) of the MI. Therefore, if the T_q is below the T_t then the MI can be depleted in the host mineral components, or if the T_q is above the T_t then the MI can be enriched in those components. The amount of host components in the melt affects the mg# [$Mg/(Mg+Fe^{2+})$] of the MI and thus the mg# of the calculated liquidus clinopyroxene in equilibrium with the melt (Danyushevsky and Lima, 2001). Calculations were performed using software PETROLOG3 (Danyushevsky and Plechov, 2011) at 100 KPa after Ariskin *et al.* (1993) assuming fO_2 values corresponding to the Ni-NiO oxygen buffer. The mg# of the calculated liquidus clinopyroxene ("calc host mg#" in Table 11) are usually higher than the mg# of the actual host (host mg# in Table 11). This implies that most inclusions were overheated during the experiments, *i.e.*, they are enriched in clinopyroxene compositions (Danyushevsky and Lima, 2001). However, ratios of

elements that are incompatible in the host and concentrations of elements that are present at similar levels in the melt and the host should not be affected significantly (Lima *et al.*, 2003).

The compositions of the analyzed MI are listed in Table 3. in Klébesz et al. (2012),Table 8. here and shown on Fig. 19-22. For crystallized MI that were analyzed by LA-ICP-MS, it was always possible to determine if the analyzed MI belongs to Type I or Type II based on petrography, but many exposed, previously homogenized MI for which no petrographic information was available were also analyzed. Therefore, for the crystallized MI analyzed by LA-ICP-MS the compositional classification Type I (open star) and Type II (open blue X) also denotes petrographic classification. For the previously homogenized MI the compositional classification as Type I (filled star) and Type II (filled blue X) is less certain and was not always confirmed by petrography. MI that had not been previously classified by petrography were classified as Type I if they had elevated alkali-content or as Type II if they had a basaltic composition (Fig. 19a). It is important to note that most of the MI classified as Type I based on composition could be confirmed petrographically. Few of the MI classified as Type II based on composition have petrographic information and these MI are referred to as "Type II" MI. Almost all of the petrographically confirmed Type II MI that were reheated first turned out to be inhomogeneous after exposing them on the surface (*e.g.*, Fig. 18e).

Based on the analyses of crystallized MI, it became evident that the MI differ not only in their petrographic characteristics, but they also have distinctive compositions. Type II MI are mainly basaltic, while Type I MI are more alkali-rich (Fig. 19a). In addition, Type II MI have much lower trace element (except Sr) concentrations compared to Type I MI (Fig. 19b). The compositions of the previously homogenized MI show much larger variations. The uncertain classification of the previously homogenized MI increases the compositional variation within each group, but the differences between the average compositions is smaller (Fig. 19b). However, the compositions of Type I MI that were identified based on petrography are similar to compositions of unhomogenized MI that were analyzed by LA-ICP-MS.

Petrographically confirmed Type II MI were heated to magmatic temperatures during homogenization experiments. Even though they were quenched when they appeared to heve homogenized, as mentioned above, most of the MI were heterogeneous (*i.e.*, contained crystalline phases) after polishing to exposing them on the surface. In most cases the MI contained a large, tabular solid phase surrounded by melt. When the phase was large enough to analyze it was confirmed to be plagioclase (filled green triangle). However, sometimes the phase was too small and some of the surrounding material was included in the analysis, resulting in elevated MgO, FeO and lower Al_2O_3 content (Fig. 21).

A few MI petrographically classified as Type II MI, and a few other MI without petrographic information that were either homogeneous or contained a very small solid phase that was not large enough to be analyzed were observed. The surrounding glass, however, was analyzed and its composition was found to be different from the compositions of the Type I MI or the other Type II MI. The glass is enriched in P_2O_5 and depleted in SiO_2 and has a high CaO/Na_2O ratio (Fig. 20), and the solid phase fluoresced under the focused electron beam. These characteristics indicate that these inclusions contain accidentally trapped apatite. When recalculated after subtracting the apatite contribution (assuming that all P represents apatite and using the stoichiometric formula $Ca_5[PO_4]_3OH$), compositions of these MI become similar to other MI (Fig. 20b).

MI data have been plotted on MgO *vs.* major oxide variation diagrams (Fig. 21a-e). While all MI data show considerable scatter, general trends are recognizable in the case of Type I MI (stars). The data show an increase in SiO_2, Al_2O_3, K_2O and also in P_2O_5 and Na_2O (not shown), and a decrease in CaO and FeO (not shown) with decreasing MgO, but no trend in the MgO *vs.* TiO_2 was observed. MI data also plotted on trace element variation diagrams. Most of the MI trace element data (Rb, Sr, Zr, Nb, Ba, La, Ce) show increasing trace element abundance with decreasing MgO content in for Type I inclusions, except for Cr, Sc and Mn. Some of the trace element data show significant scatter and no trend can be recognized for MgO *vs.* Y, Nd, Sm, Eu and Yb (not shown). Compositions of the homogenized MI and the crystallized MI partially overlap, however homogenized MI show a wider compositional range. The observed trends are consistent with compositional resulting from overheating of the MI or incorrect estimate of the MI/host ratio to interpret LA-ICP-MS analyses.

The differences between the crystallized Type I and Type II MI are evident on the variation diagrams (Fig. 21), but the difference is not as obvious for rehomogenized Type I and "Type II" MI. "Type II" form a continuing trend from Type I compositions towards more primitive compositions and towards the composition of the host clinopyroxene. However, on the trace element variation diagram (Fig. 21h) Type I and Type II compositions do not form a continuous trend. It is noteworthy that compositions of Type II and "Type II" MI always plot in between the compositions of the Type I MI, plagioclase and the host clinopyroxene. This trend is more evident on the Ba/Sr *vs.* 1000/Sr diagram (Fig. 21i), where mixing between endmembers defines straight lines. Therefore, the compositions of Type II and "Type II" can be derived from the mixing of plagioclase ± Type I melt ± host clinopyroxene. It is important to note that "Type II" MI are not in equilibrium with their host clinopyroxene and they are usually smaller than 20 µm.

Volatiles, such as F, Cl, S, H_2O and CO_2 were also analyzed in selected homogenized MI. The H_2O content was uniformly low, below 0.15 wt. %. The CO_2 varied between 131-1893 ppm but was mostly below 400 ppm. The F content ranged up to 4000 ppm but in some cases it is thought to be higher but the analytical conditions prevented us from determining the exact concentration (for details see chapter 3.5). The S and Cl contents also vary greatly, reaching maximum concentrations of 156 ppm and 2771 ppm, respectively. No correlation could be observed between the volatile abundances, except that the S concentration increases with increasing Cl concentration (Fig. 22).

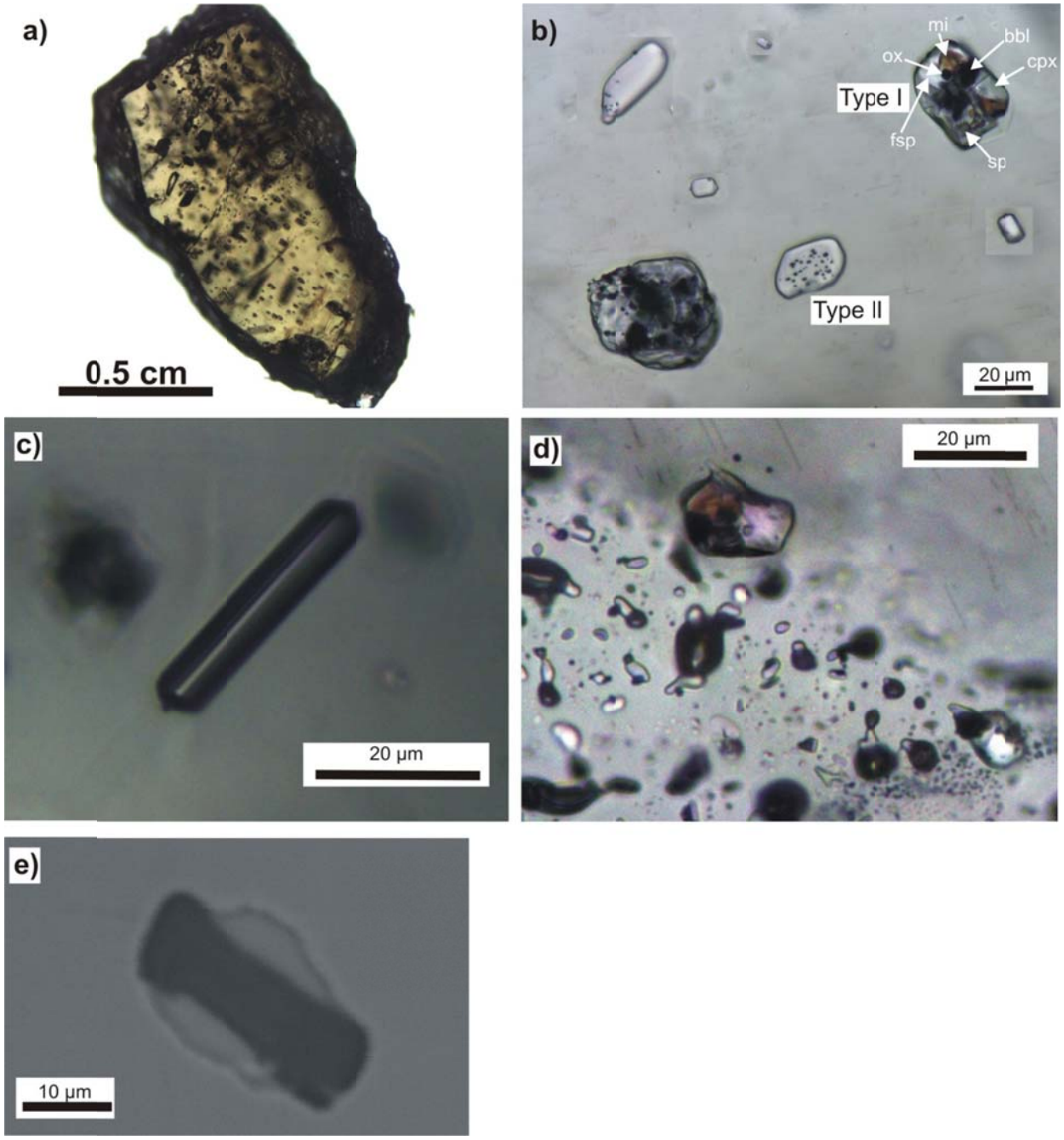

Figure 18. – a) Photomicrograph of a single clinopyroxene crystal containing numerous solid inclusions and MI. b) Photomicrograph of the two types of MI hosted by clinopyroxene in Type A nodules (cpx – clinopyroxene, sp – spinel, fsp – feldspar, ox – Fe-Ti-oxide, mi – mica, bbl – bubble). c) Photomicrograph of a single phase inclusion (FI?), and d) a plane of two phase irregular inclusions. e) SEM image of an exposed Type II inclusion after the heating experiment.

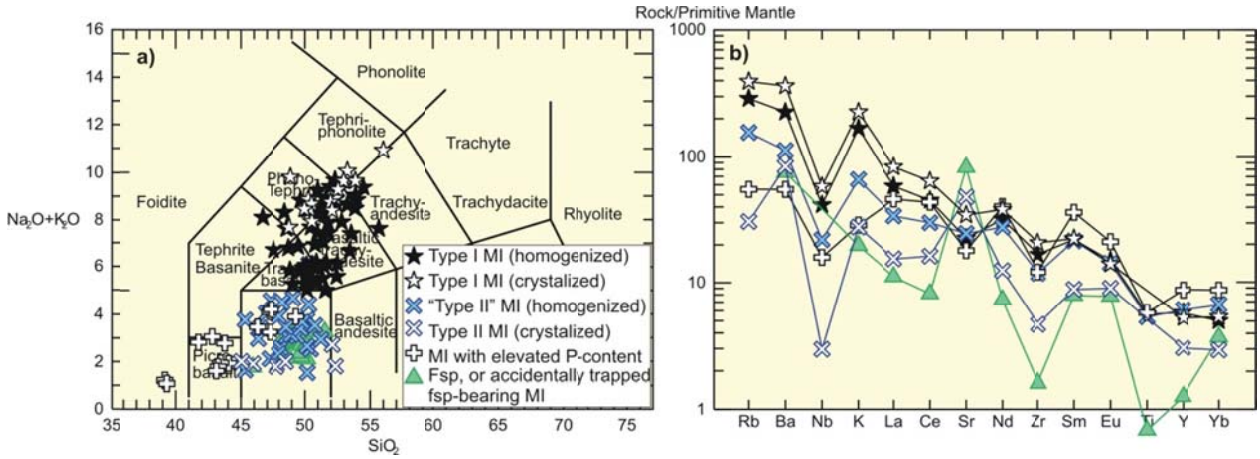

Figure 19. – Compositions of MI in clinopyroxene from Type A nodule (NLM1-1a) plotted on a) Total alkali silica diagram (Le Bas *et al.*, 1986) and the primitive mantle (pyrolite, McDonough and Sun, 1995) normalized average composition of the different MI types plotted on b) trace element "spider" diagram.

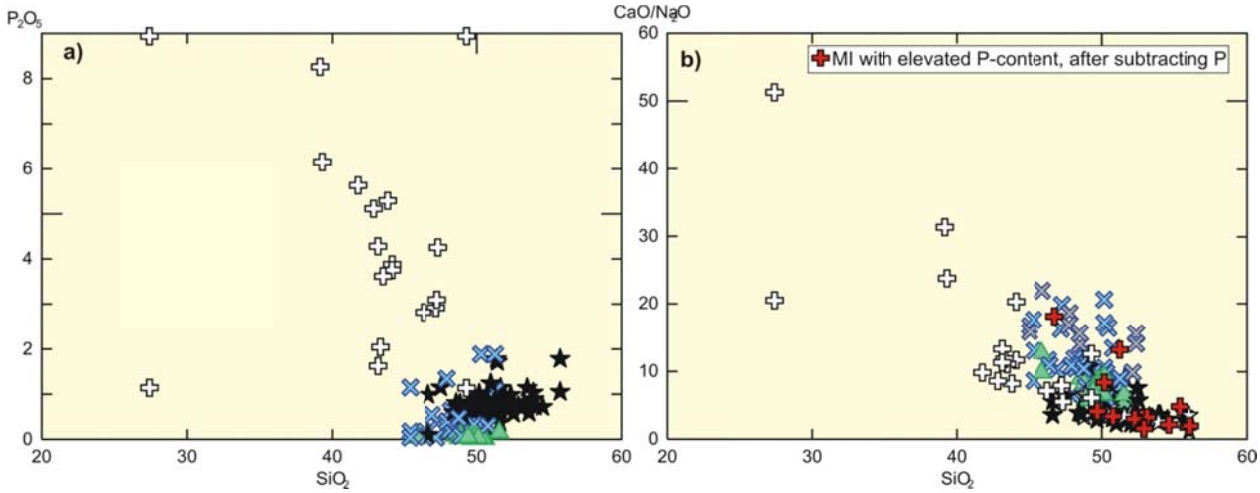

Figure 20. – Composition of the MI in clinopyroxene from Type A nodule (NLM1-1a) plotted on a) SiO_2 (wt. %) *vs.* P_2O_5 (wt. %) and b) SiO_2 *vs.* CaO/Na_2O diagram. Some of the inclusions have elevated P content and CaO/Na_2O ratio, indicating trapping of apatite. After subtracting the apatite (red crosses), the CaO/Na_2O ratio of the MI is closer to the ratios of Type I MI. Symbols are as in Fig. 19.

Figure 21. (Below) – Compositions of MI in clinopyroxene from Type A nodule (NLM1-1a) plotted on multi-element variation diagrams. Major oxides are in wt. %, trace elements are in ppm. See text for details. Symbols are as in Fig. 19.

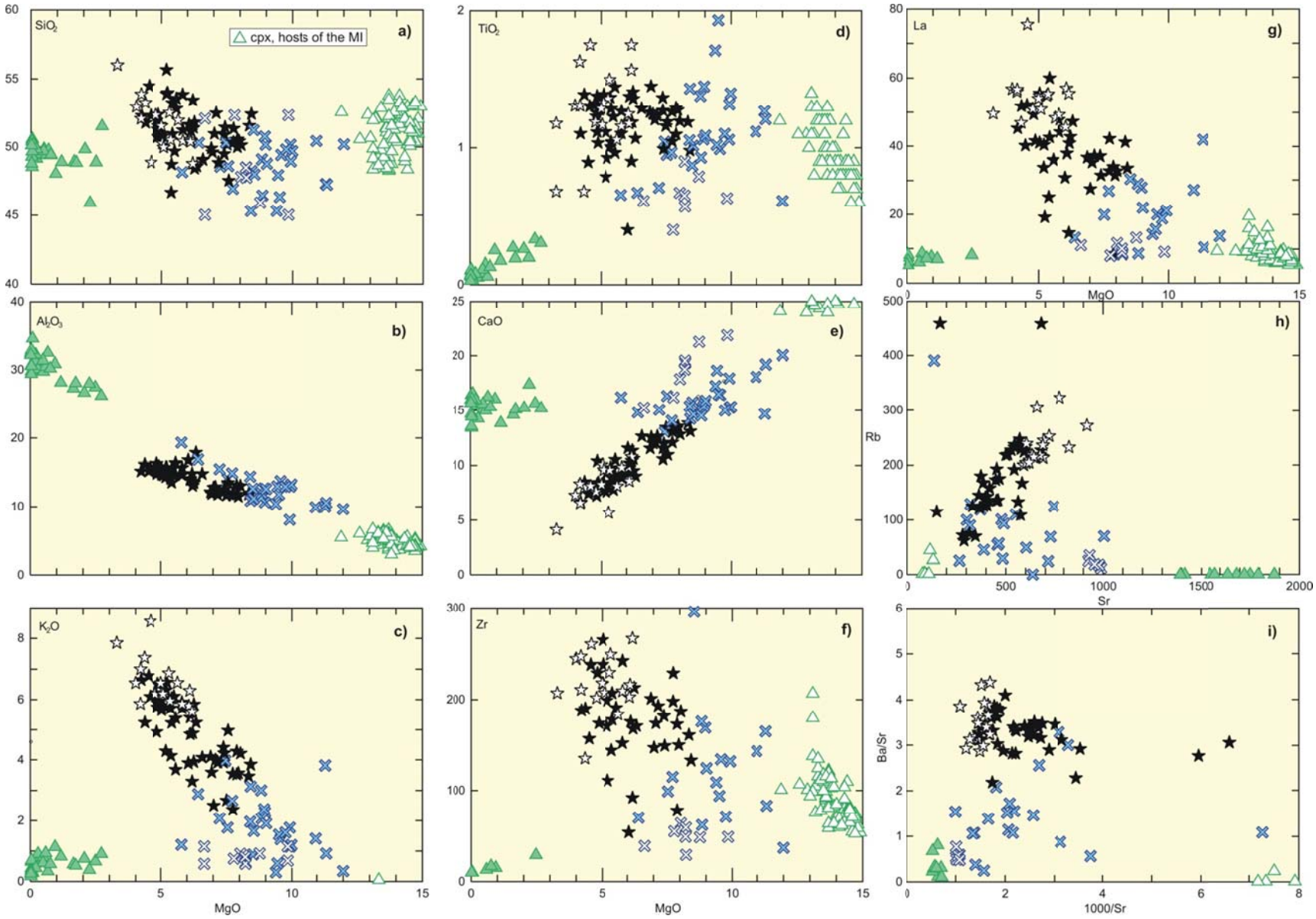
SiO2
cpx, hosts of the MI
a)
TiO2
d)
La
g)
Al2O3
b)
CaO
e)
Rb
h)
Sr
K2O
c)
Zr
f)
Ba/Sr
i)
MgO
MgO
1000/Sr

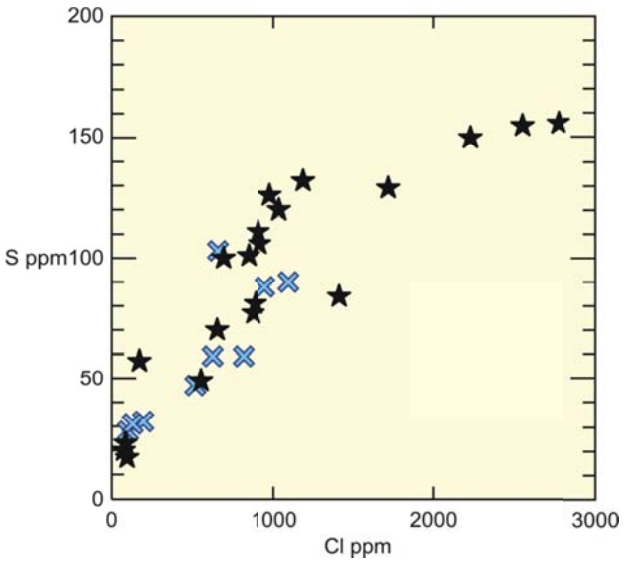

Figure 22. – Composition of MI in clinopyroxene from Type A nodule (NLM1-1a) plotted on Cl *vs.* S diagram. Symbols are as in Fig. 19.

4.4. MI in Type B nodules

Crystallized MI in hydrous minerals, like amphibole, cannot be rehomogenized in a heating stage and are not frequently studied. Halter et al. (2004) showed, however, that the composition of MI in amphibole can be successfully determined by LA-ICP-MS, and provide valuable information about petrogenetic processes. Clinopyroxene in sample NLM1-1d (Type B nodule) is very small and lack of useful MI, therefore only MI in amphibole could potentially provide information on the melt composition.

In some cases the amphiboles in Type B nodule (NLM1-1d), or at least some of the amphiboles are free of MI, or only a few randomly distributed MI can be observed (Fig. 23b). However, in most cases the amphiboles contain numerous polyphase MI and apatite and mica solid inclusions (Fig. 23a). The size of the polyphase inclusions is usually ~10 µm, but varies from 3 to 30 µm. The distribution of phases of the inclusions is difficult to determine petrographically. Under transmitted light the MI contain one or more colorless-light brown phases and often one or more dark rounded phases, possibly bubbles (Fig. 23c). SEM imaging confirmed the presence of bubbles and that the colorless-light brown phases are most likely micas based on their habit; alternatively the colorless phase could be apatite. The micas usually show strong compositional zoning, observed by SEM. Often another phase is observed adjacent to or surrounding the mica. This phase appear darker than mica, apatite, and the host amphibole on SEM images (Fig. 23d). This phase is interpreted to be glass, but due to the size of the inclusions it could not be analyzed by EPMA to confirm its composition. Based on petrographic observations, *i.e.*, the small amount or lack of glass, the lack of other mineral phases and the size and strong zoning of the micas, these MI probably do not represent homogeneously trapped melt droplets that later crystallized due to slow cooling, but rather were trapped heterogeneous mixture, *i.e.*, a mica crystal together with a small melt film and with a bubble. However, the bubble could represent a shrinkage bubble that formed later

due to cooling. The bubbles are rarely larger than 1 µm, therefore it is not possible to analyze the bubbles to determine if they contain any volatile components. Even though the polyphase inclusions are most likely not representative of the crystallizing melt, they were analyzed with LA-ICP-MS to confirm our interpretation.

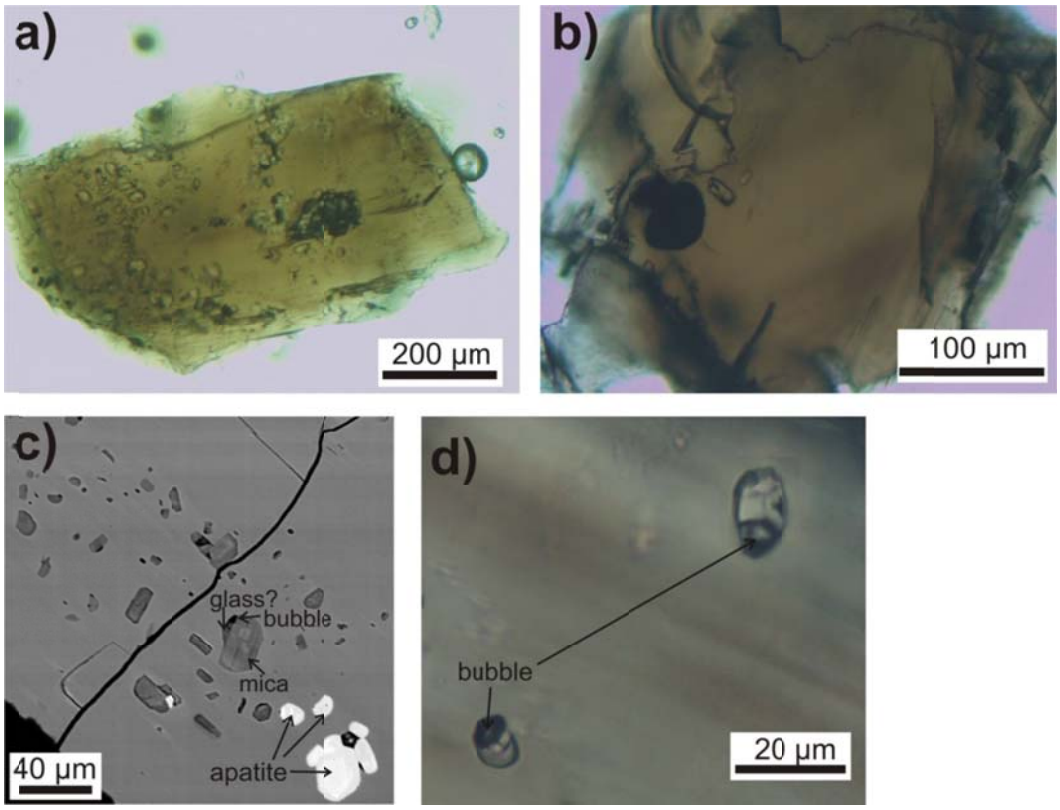

Figure 23. – Photomicrographs of amphibole phenocrysts from Type B nodule (NLM1-1d) with a) numerous inclusions and b) few inclusions. c) SEM image of the solid and polyphase inclusions in amphibole from Type B nodule. d) Photomicrograph of the polyphase inclusions in amphibole.

The complex host amphibole composition makes it more difficult to recognize the boundaries of the MI in the LA-ICP-MS signal (Fig. 24) compared to MI hosted in clinopyroxene. By monitoring the changes in the K, Rb and Ba signals it is possible to determine which part of the signal belongs to the inclusion plus host mixture. For an internal standard we chose an Al_2O_3 concentration of 18 wt. %, however it is important to note that the Al profile is flat in the LA-ICP-MS signal. In some cases, using an Al_2O_3 concentration of 18 wt. % as the internal standard results in a very small, or even negative *x* (ratio of MI to host) and/or greater than 100 wt. % concentration for some oxides. These results, of course, are not possible and these MI were not considered further. Thirteen (13) out of 40 inclusions showed x>0.2. An Al_2O_3 concentration of 13 wt. % was also tested as an internal standard, because the average alumina content of the phlogopite in NLM1-1d samples (Type B nodule) is 12.82 wt. %. If our assumption that the MI trapped mica is correct, then the alumina content of the inclusions should be approximately 13wt. %. In almost all cases using an Al_2O_3 concentration of 13 wt. % as the internal standard yielded to a larger than one, or a negative value for x value (Table 9).

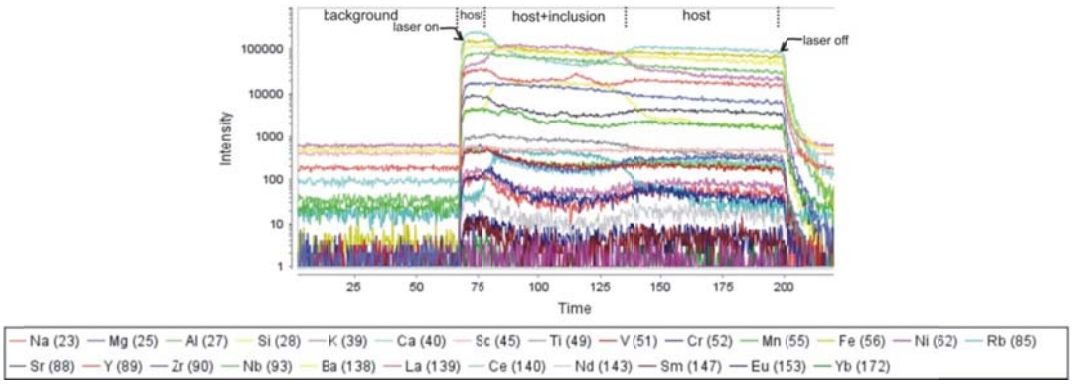

Figure 24. – Typical LA-ICP-MS spectra of an MI and the amphibole host.

According to the total alkali-silica diagram (Le Bas *et al.*, 1986), the polyphase inclusions in amphiboles from Type B nodule (NLM1-1d) have a foidite composition, due to their low silica and high alkali contents. One MI is classified as tephrite basanite, and another has a phono-tephrite composition, and a third has a tephra-phonolite composition (Fig. 25a). The silica content (37.5-42.8 wt. %, rarely up to 49.5 wt. %) and the Na_2O concentration (0.4-2.7 wt. %) of the MI vary little, but there is significant variation in the MgO (6.8-31.7 wt. %), K_2O (3.6-18.7 wt. %), CaO (from below detection up to 12.7 wt. %) and FeO (3.0-10.2 wt. %). In addition, a positive correlation is observed between MgO and K_2O, and TiO_2, and a negative correlation is observed between MgO and Na_2O and CaO. Also, a positive correlation is observed between MgO and Ba and MgO and Rb (Fig 26). The three inclusions with non-foidite compositions have not only higher silica content than the others, but also have higher Na_2O content, but lower K_2O and MgO contents. Significant variation is observed in trace element abundances (Fig. 25b). The inclusion with a phono-tephrite composition has significantly higher REE and Zr content than the other inclusions. Another inclusion has high Ba (up to 19557 ppm), Rb (36-514 ppm) and Sr (301-3851 ppm) contents. Variable REE and Zr (from below detection up to 691 ppm) contents are observed, but these elements do not show systematic variation with MgO content.

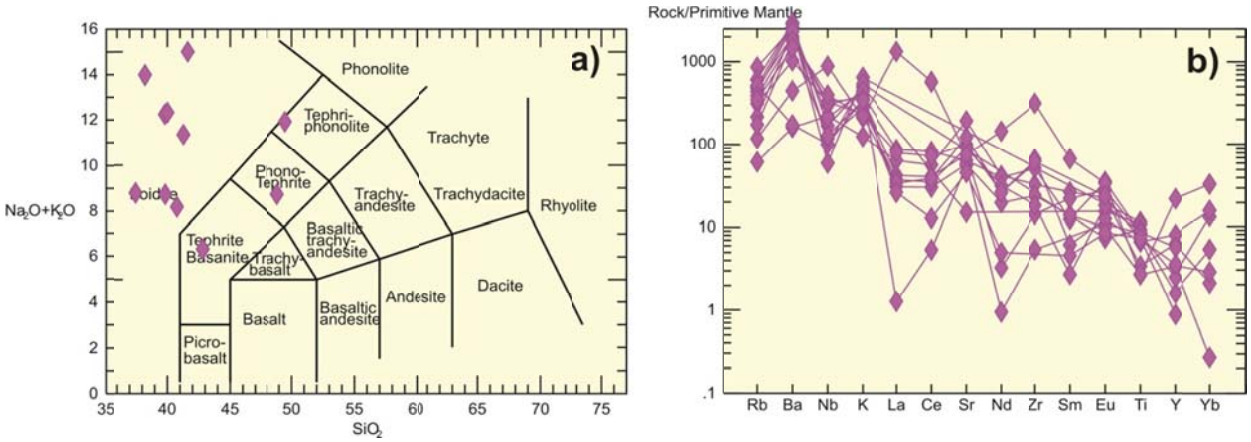

Figure 25. – a) Total alkali silica (Le Bas *et al.*, 1986) diagram and b) primitive mantle (pyrolite, McDonough and Sun, 1995) normalized trace element variation diagram of MI in amphibole from a Type B nodule (NLM1-1a).

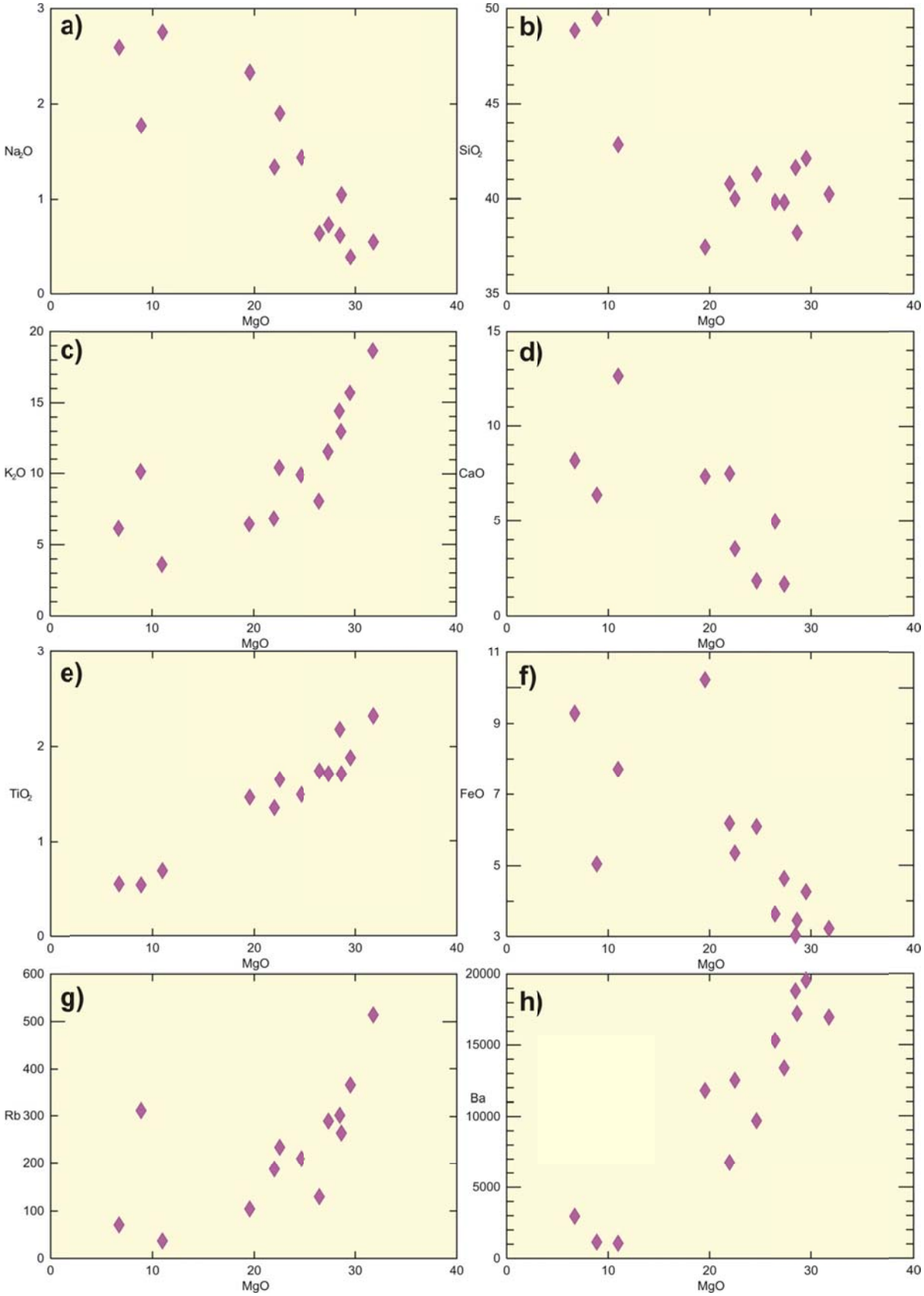

Figure 26. - Multi-element variation diagrams of MI in amphibole from a Type B nodule (NLM1-1d)

5. Discussion

5.1. Constrains on the origin of the nodules

This chapter summarizes our initial hypotheses for the origin of the nodules based on the preliminary results, which were published in the paper Klébesz *et al.* (2012). It is important to note that this hypothesis is based only on the crystallized MI analyzed by LA-ICP-MS. Data for the homogenized MI are not consistent with this hypothesis, as discussed later in chapter 5.2.

Based on the textures, both Type A and B nodules can be classified as "sub-effusive type" nodules as defined by Hermes and Cornell (1978). These workers suggest a crystal-mush zone in which the crystal/melt ratio was high for the origin of this type of nodule. The petrographic characteristics such as bimodal grain size (porphyrogranular texture), slight zonation of the phenocrysts, crystallized melt pockets, and "jagged" edges of crystals, are consistent with the interpretation of a crystal-mush origin, although Type A and B nodules clearly must have been derived from different parts of the magma chamber or conduit system based on their differing modal compositions and chemistry of the minerals. The MI geochemistry of Type A nodules is consistent with the crystal-mush origin.

Type I and Type II MI are spatially associated, which suggests a genetic relationship but the nature of this relationship is unclear. The melts represented by the two types of MI most likely have not differentiated from the same parent melt, as might be suggested from the close spatial association and their trace element distribution. Type I MI are interpreted to represent the melt from which the surrounding host clinopyroxene crystallized because the MI compositions are in or close to chemical equilibrium with the host, unlike Type II MI. This suggests that the compositions of Type II MI were modified by local processes. Accidental entrapment of solid phases in a Type I inclusion would modify the composition, or the MI compositions could reflect heterogeneities within the crystallizing melt. The major element composition (*i.e.*, high Ca, high Mg and low K contents) of Type II MI suggest that the trapping and/or dissolution of An-rich plagioclase in normal Type I inclusion and/or assimilation of dolomite at depth (either by trapping small dolomite crystals in the MI or incorporating dolomite into the parental magma before MI trapping) could produce the anomalous Type II composition. Plagioclase is observed as solid inclusions in clinopyroxene, therefore it is likely that some plagioclase would also be trapped together with a melt to form a MI. Mesozoic carbonates with a thickness of about 8 km that dip westward from the adjacent Apenninic belt have been detected at a depth of 2–3 km in the Mt. Somma-Vesuvius area (Bruno *et al.*, 1998; Cella *et al.*, 2007; De Natale *et al.*, 2004). Therefore, dolomite assimilation cannot be excluded, but stable isotopic data are required to confirm this hypothesis. MI compositions that are in equilibrium with their host occurring in the same crystal as MI with anomalous compositions (not in equilibrium with their host) have been described from several different environments (Danyushevsky *et al.*, 2004). Danyushevsky *et al.* (2004) explained the origin of these anomalous MI with "dissolution-reaction-mixing (DRM) processes". In the plumbing system the intruding magma batches can react with the much cooler wall rock and/or material in the semi-solidified crystal-mush zones. During this interaction, the intruding magma cools and mineral phases that are not in equilibrium with the intruded melt, may undergo partial dissolution. Subsequent mixing of the reaction products with the intruded melt may produce hybrid melts that can be trapped as MI. These

processes can lead to large localized melt heterogeneities. Danyushevsky *et al.* (2004) emphasize that these anomalous and commonly large inclusions are formed at the edges of the conduit system. Analogously, our hypothesis is that the observed MI types reflect real heterogeneities within the melt caused by DRM processes (Danyushevsky *et al.*, 2004) occurring near the magma chamber wall. This hypothesis is in agreement with the observed petrographic features.

On the other hand, the composition of the minerals is inconsistent with the hypothesized origin (*i.e.*, the mush-zone of the Sarno (PB) magma chamber as the origin of the nodules). In the plinian deposit of the Sarno (PB) eruption, Landi *et al.* (1999) described discrete crystals and crystal aggregates consisting of plagioclase or plagioclase, clinopyroxene, Ti-magnetite and occasionally sanidine and potassium-ferripargasitic amphibole, together with glass. Some of the discrete crystals in the aggregates were xenocrysts (*i.e.,* they have more evolved compositions than the minerals of the host rock). The chemical variations of the bulk rock are consistent with fractional crystallization and do not indicate significant syn-eruptive mixing. Therefore, Landi *et al.* (1999) interpreted the origin of the xenocrysts as disaggregation of the crystallizing mush zone at the upper part of the magma chamber, where trachytic magmas occurred. Comparing the mineral compositions from the nodules to the compositions of the xenocrysts and crystal aggregates described by Landi *et al.* (1999) shows that the feldspar compositions overlap, although it is important to note that there are large variations in feldspar composition. The clinopyroxene, amphibole and mica compositions, on the other hand, are generally less evolved in the samples from this study compared to those described by Landi *et al.* (1999). In addition, Landi *et al.* (1999) did not describe olivine as a phase in the plinian deposit, either as phenocryst or as xenocryst. This compositional difference, however, does not eliminate the hypothesized mush-zone origin for the nodules. The differences may indicate that the nodules studied here were formed in a region of the magma chamber that was not sampled during the plinian phase of the eruption (*e.g.,* from a more crystal-rich part that was closer to the margin) and might not have crystallized from the magma that was erupted during the Sarno (PB) eruption, or from a different depth in a layered magma chamber. The latter interpretation is consistent with results of Landi *et al.* (1999) who suggest that the magma chamber associated with the Sarno (PB) eruption was compositionally layered.

In summary, the results of the petrographic study and the preliminary results of the MI studies of Type A nodules are consistent with an interpretation that the nodules represent the crystal rich part of the crystallizing boundary layer at the walls of the magma chamber. It is not possible at this time to determine if the nodules represent the same magma which was erupted during the sustained column phase of the Sarno (PB) eruption, or if they crystallized from a melt associated with an older eruption.

5.2. Comparison of the MI data with MI and bulk rock data from the literature

5.2.1. MI from Type A nodule (NLM1-1a)

Based on new petrographic information and data obtained during the heating experiments and subsequent analyses of the reheated MI, an origin for the nodules in the mush zone of the Sarno (PB) magma chamber is not supported.

It was previously assumed that Type I and Type II MI record small scale heterogeneities within the melt, which is common at the edges of a magma conduit system (Danyushevsky *et al.*, 2004). However, Type II MI could not be homogenized by heating. This implies that Type II MI did not trap a single melt phase which subsequently crystallized during cooling, but rather trapped a solid phase together with melt. The solid phase was likely An-rich feldspar but in some cases it was apatite. This is supported by the chemical data, which show that the composition of the crystallized Type II MI can be derived by mixing of an An-rich feldspar and the host clinopyroxene. The compositions of "Type II" MI vary within wider ranges compared to Type II MI but they also can be derived from the mixing of plagioclase ± Type I melt ± host clinopyroxene. This implies that "Type II" inclusions are either overheated Type I inclusions that become enriched in clinopyroxene component as a result of overheating and/or trapped feldspar. This interpretation is supported by the fact that these inclusions are not in equilibrium with their host. The calculated liquidus composition for clinopyroxene is generally much more magnesian than the observed compositions. In addition, the inclusions with anomalous Mg concentrations are usually smaller than 20 µm. Therefore, if they are hosted in a mineral containing larger MI that were observed during the heating experiment, then the smaller MI might have homogenized at a lower temperature than the temperature from which the crystal was quenched, and would have therefore been overheated. Based on these observations, it is likely that only Type I MI are representative of the melt from which the clinopyroxene crystals grew. Therefore, only Type I MI compositions are compared with other data from the literature to investigate the possible origin of the nodules.

Compositions of MI in various host phases from nodules from different eruptions of Mt. Somma-Vesuvius have been compiled from the literature (Fig. 27). Unfortunately, data are only available from the 79 AD nodules and younger eruptions. MI in syenite nodules and skarns from the 472 AD eruption (Fulignati *et al.*, 2001; Fulignati and Marianelli, 2007) have significantly different compositions than any other MI reported in the literature or the MI of this study. Fulignati *et al.* (2001) interpreted nodules from the 472 AD eruption to represent the magma chamber-carbonate wall rock interface. In addition to the highly differentiated phonolitic MI, Fulignati *et al.* (2001) also found complex chloride-carbonate and hydrosaline melt inclusions, as well as unmixed silicate-salt melt inclusions. Compositions of MI in skarns from the 1944 eruption (Fulignati *et al.*, 2004) do not show such extreme compositions as those from the 472 AD eruption but still differ from the compositions of MI from cumulate nodules. MI from skarns of the 1944 eruption tend to have lower SiO_2 and MgO content, but higher Al_2O_3, MnO, Na_2O and Cl contents. In addition, hypersaline FI are commonly associated with these MI. The clinopyroxene host in skarns has much higher Al_2O_3 content, usually above 7 wt. %, compared to clinopyroxenes from the juvenile rocks (Fulignati *et al.*, 2004). The clinopyroxene in this study has significantly lower Al_2O_3 content, usually less than 6 wt. %, and lacks complex hydrosaline and chloride-carbonate inclusions, and the MI in this study show compositions similar to MI in cumulate nodules rather than those in skarns. Consequently, the nodules studied here do not represent an environment close to the carbonate wall rock. However, it is important to emphasize that this does not exclude the possibility that these nodules can represent the crystal-mush zone.

Klébesz et al. (2012) concluded that the petrographic features are consistent with a crystal mush origin but it is unclear whether these nodules represent the same magma that was erupted during the sustained column phase of the Sarno (PB) eruption or if they crystallized from a melt associated with an older eruption. In order to answer this question, compositions of MI in clinopyroxene from a Type A

nodule (NLM1-1a) were compared to bulk rock compositions of juvenile eruptive products of Mt. Somma-Vesuvius (Fig. 28 and Fig. 29). The volcanic products of Mt. Somma-Vesuvius and their temporal variability have been studied extensively (for references see Fig. 28. or Chapter 1.), however it is not the focus of the current research.

MI in this study show a continuous trend towards high CaO/Al_2O_3 when plotted against other indicators of magma evolution (Fig. 28 and 29). The least magnesian MI generally fit within the general trend defined by the Mt. Somma-Vesuvius rocks, whereas the MI with more primitive compositions (up to about 8 wt. % MgO) overlap or show a trend similar to recent Vesuvius volcanics. The recent Vesuvian volcanic rocks form tight compositional groupings at MgO> ~ 4wt. % and CaO/Al_2O_3> ~ 0.6, as has already been recognized by Danyushevsky and Lima (2001) and Marianelli *et al.* (1999). According to their interpretations, these rocks do not reflect true melt compositions, instead they reflect accumulations of clinopyroxene crystals. Hence, these volcanic rocks represent magmas formed by mixing of evolved melts and various amounts of clinopyroxene crystals inherited from the cumulate layers (Danyushevsky and Lima, 2001; Marianelli *et al.*, 1999). The similarities between the trends defined by these volcanics and the MI of this study support the interpretation that the observed compositional trends are caused by incorporating varying proportions of clinopyroxene component into the melt as a result of overheating the MI. However, there are still some important compositional features that cannot be explained by overheating.

As it can be seen on the plots for TiO_2, K_2O, P_2O_5 and MgO on Fig. 28, it is not possible to account for the disagreement in compositions of MI in clinopyroxene compared to the whole rock trend of the Sarno (PB) and younger eruption, regardless of the amount of clinopyroxene component added to the MI by overheating. In other words, the compositions of MI in this study are more enriched in MgO, K_2O, TiO_2 and P_2O_5 compared to any known compositions of volcanics from the Sarno (PB) eruption or any other eruptions from the first mega cycle. The same phenomenon can be observed with trace element systematics shown on Fig. 29. More specifically, the compositions of the MI from the nodules are more enriched in Sc, V, Cr and Ni but depleted in Sr, Y, Zr, Ba and Ce compared to the bulk rock compositions of the Sarno (PB) and younger volcanics of the first mega-cycle. In fact, the compositions of MI of this study are similar to the compositions of lava rocks from the older Somma (pre-Sarno) activity. Danyushevsky and Lima (2001) reported that these pre-Sarno (PB) rocks can be divided into two groups based on composition. The first group has a composition similar to rocks of the first and second mega-cycles (low K-group), while the second group has high KO_2 and SiO_2 and low Na_2O content (high-K group). The least magnesian compositions of MI in this study in most cases overlap with the compositions of the low-K group of older Somma rocks. This overlap is best illustrated on the major element diagrams (Fig. 28), but most of the trace elements also show similar behavior. However, the trace element data vary greatly in some cases. For example, Sm varies over a wide range, Sc and V concentrations in most MI are higher than in the lava rocks, while Sr seems to be lower. It is important to note that in some analyses the level of detection for Sc was relatively high (up to 60 ppm), therefore some inclusions are not plotted here because the Sc concentration was below the detection limit, and Sc concentrations in those MI might be well within the range of the older Somma volcanics. The lower Sr concentration might reflect some analytical error, or be the result of extensive plagioclase crystallization, depleting the remaining melt in Sr. However, an analytical error cannot be exluded, it is unlikely, because the MI compositions obtained during different analytical sessions are similar to each

other and define the same trend. Petrographic evidence suggests that An-rich plagioclase, which is enriched in Sr, crystallized together with the clinopyroxene, but it is not known if this process can explain the lower Sr content in the MI.

Despite some uncertainties in the trace element compositions, the host clinopyroxene crystals in nodule NLM1-1a are interpreted to have crystallized from a magma that was erupted during the early Somma activity, prior the Sarno (PB) eruption, and not from the magma that was erupted during the sustained column phase of the Sarno (PB) eruption. This, however, does not necessarily mean that the entire nodule crystallized from the same magma or that all of the other nodules crystallized from this "old" magma. It is likely that the entire NLM1-1a nodule formed from the same magma that was erupted during the early stage of evolution of Somma, because no chemical or petrographic evidence is observed that would suggest that the clinopyroxenes in the nodule are xenocrysts. Even though rare zoning can be observed, it is not common and resorbtion surfaces are absent. Also, the composition of the rims is similar to the composition of groundmass clinopyroxene. Therefore, if the rim and the groundmass crystallized from a different melt, two generations of MI would be expected; one with compositions similar to the Sarno (PB) rocks and one similar to what is observed during this study. However, the absence of the former type of MI can be a statistical error due to under sampling, but this is thought to be unlikely because of the absence of other indicators and because the host compositions sample the entire compositional range of observed clinopyroxene in NLM1-1a.

It is not possible to infer an origin of the other Type A nodules (NLM1-1a, and -1b) in the absence of MI data. Compositional zoning and resorbtion surfaces are more common in clinopyroxene of NLM1-1b and some Mg-rich cores were also observed, indicating that these nodules formed in a more dynamic environment than NLM1-1a. However, in general the compositions of the rock-forming minerals of the different Type A nodules more or less overlap, indicating probably that they formed from melts with similar compositions. Little mineral composition data are available for the older Somma lavas, and trace element data are almost nonexistent, eliminating the possibility to constrain the origin of these nodules.

The origins of the skarns and cumulate nodules are well constrained, not much information is available about the origin of sub-effusive type nodules in general. This type of nodules has been reported by Hermes and Cornell (1978) from several different eruptions, but they are little studied. Most commonly, they are interpreted as shallow plutonic rocks that are usually equivalent in chemistry to the erupted lavas or pyroclastics (Belkin and De Vivo, 1993; Hermes and Cornell, 1978) or intermediate between lava and cumulate compositions (Hermes and Cornell, 1978). Hermes and Cornell (1978) suggested that they represent the crystal rich part of the crystal mush zone but this hypothesis was never tested. Although, the origin of the nodules in this study cannot be determined with certainty, their presence in the Sarno (PB) eruption indicates that the magma that erupted during the Sarno (PB) eruption came from the same or deeper magma chamber(s) as the magma that erupted earlier, and the ascending magma accidentally picked up older, possibly already solidified rock fragments. If the interstitial liquid had not yet solidified, it would have quenched into glass, as observed in the cumulate nodules (*e.g.*, Hermes and Cornell, 1978).

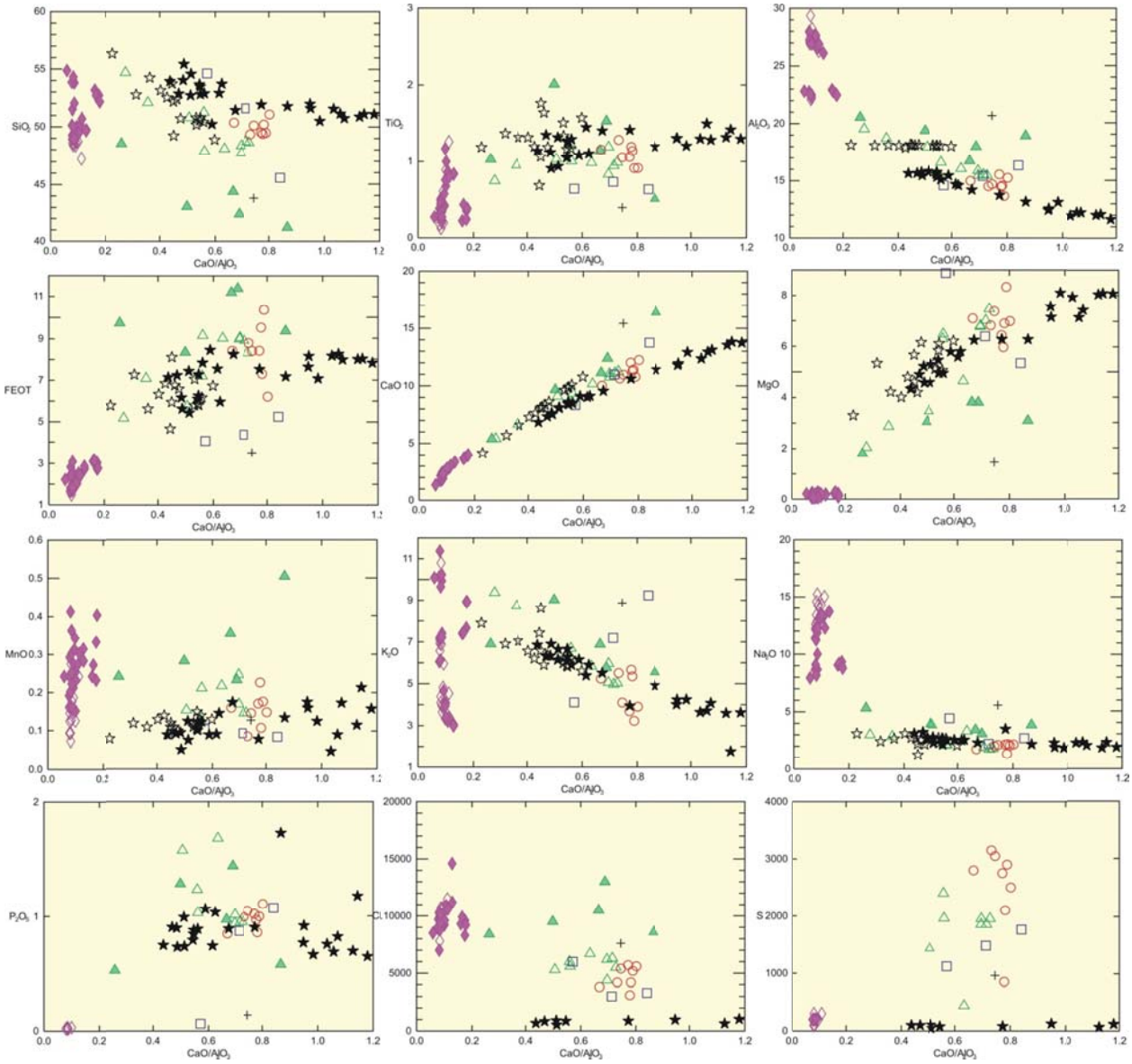

Figure 27. – Comparison of compositions of Type I MI (**open star** – crystallized, **filled star** – rehomogenized) in clinopyroxene from Type A nodule (NLM1-1a) with other MI in nodules reported in the literature. **Open triangle** – MI in cumulate nodules from the 1944 eruption (Hermes and Cornell, 1981; Lima *et al.*, 2003; 2007); **filled triangle** – MI in skarn nodules from the 1944 eruption (Fulignati *et al.*, 2004); **open squares** – MI in cumulate nodules from eruptions between 1440 and 1631 (Lima *et al.*, 2003); **open diamond** – MI in syenite nodules from the 472 AD eruption (Fulignati and Marianelli, 2007); **filled diamond** – MI in skarns from the 472 AD eruption (Fulignati *et al.*, 2001); **open circle** – MI in cumulate nodules from the 79 AD eruption (Lima *et al.*, 2007); **cross** – MI in cumulate nodule from a pre-79 AD eruption (Lima *et al.*, 2003). All data recalculated to 100 % anhydrous. See text for discussion.

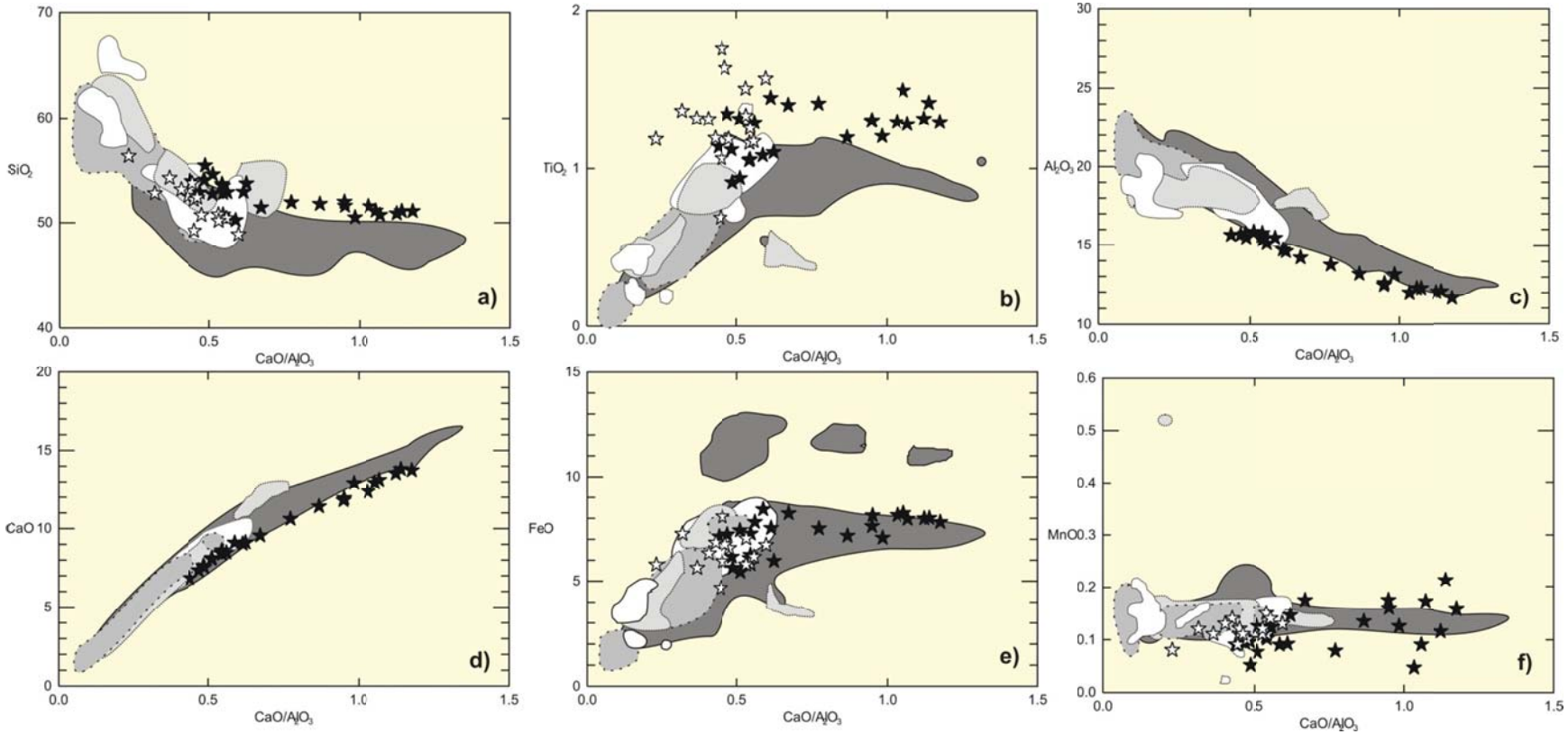

Figure 28. – Comparison of the compositions of Type I MI in clinopyroxene from a Type A nodule (NLM1-1a) with bulk rock compositions of juvenile eruptive rocks from Mt. Somma-Vesuvius on CaO/Al_2O_3 *vs.* major element diagrams. Bulk rock data from the literature (Ayuso et al., 1998; Barberi et al., 1981; Belkin et al., 1998; Belkin et al., 1993; Black et al., 1998; Cioni, 2000; Cioni et al., 1995; Cioni et al., 1998; Civetta et al., 1991; Fulignati and Marianelli, 2007; Joron et al., 1987; Lima et al., 1999; Marianelli et al., 1995; Marianelli et al., 1999; Marianelli et al., 2005; Marini et al., 1998; Mastrolorenzo et al., 1993; Mues-Schumacher, 1994; Paone, 2006; Paone, 2008; Piochi et al., 2006a; Raia et al., 2000; Rolandi et al., 1993a; Rosi and Santacroce, 1983; Santacroce et al., 1993; Santacroce et al., 2008; Schiano et al., 2004; Somma et al., 2001; Vaggelli et al., 1993; Villemant et al., 1993; Webster et al., 2001). All data recalculated to 100 % anhydrous. See text for discussion.

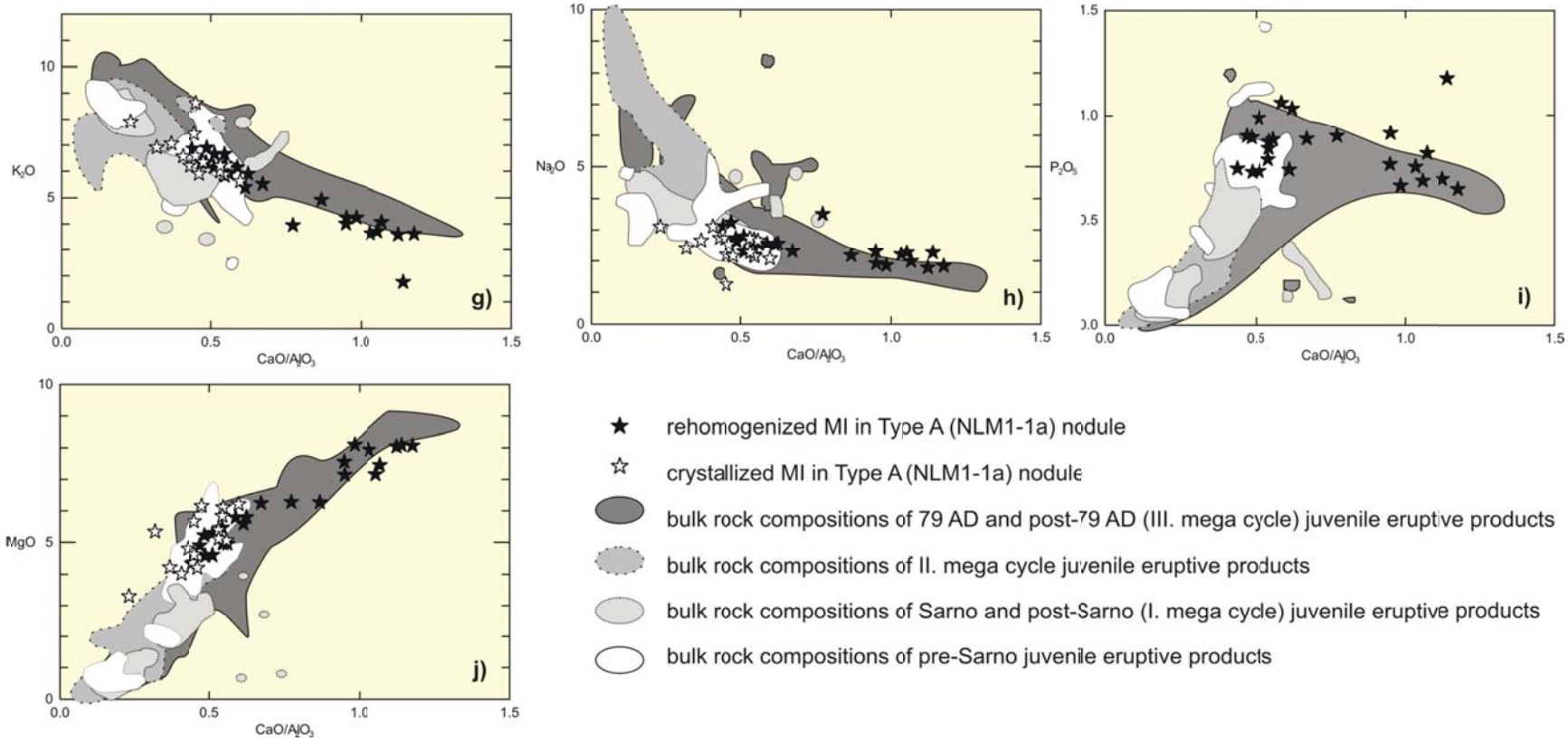

Figure 28. (cont.)

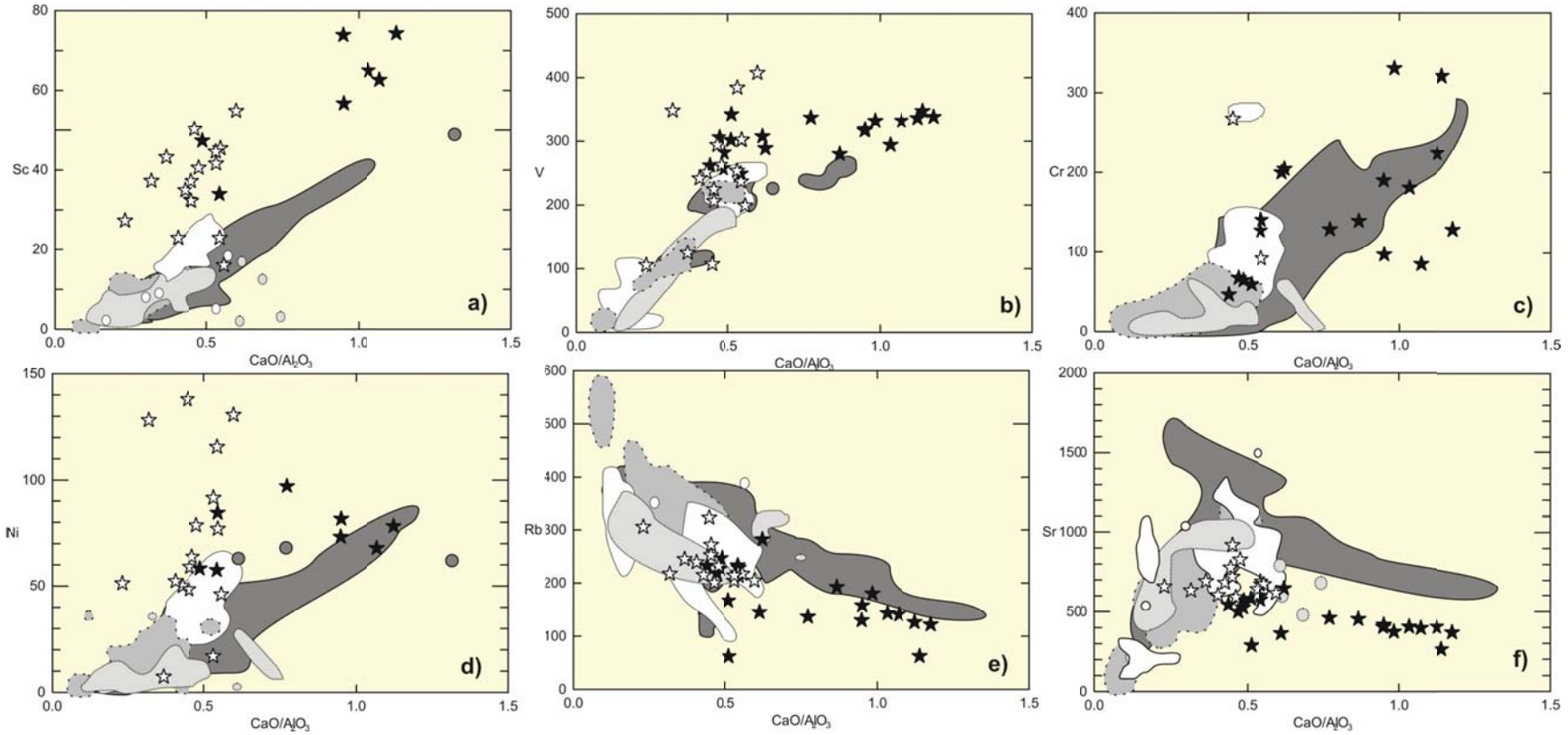

Figure 29. – Comparison of the compositions of Type I MI in clinopyroxene from a Type A nodule (NLM1-1a) with bulk rock data of juvenile eruptive rocks from Mt. Somma-Vesuvius on CaO/Al_2O_3 *vs.* selected trace elements diagrams. Symbols and data from the literature are the same as in Fig. 28. All data recalculated to 100 % anhydrous. See text for discussion.

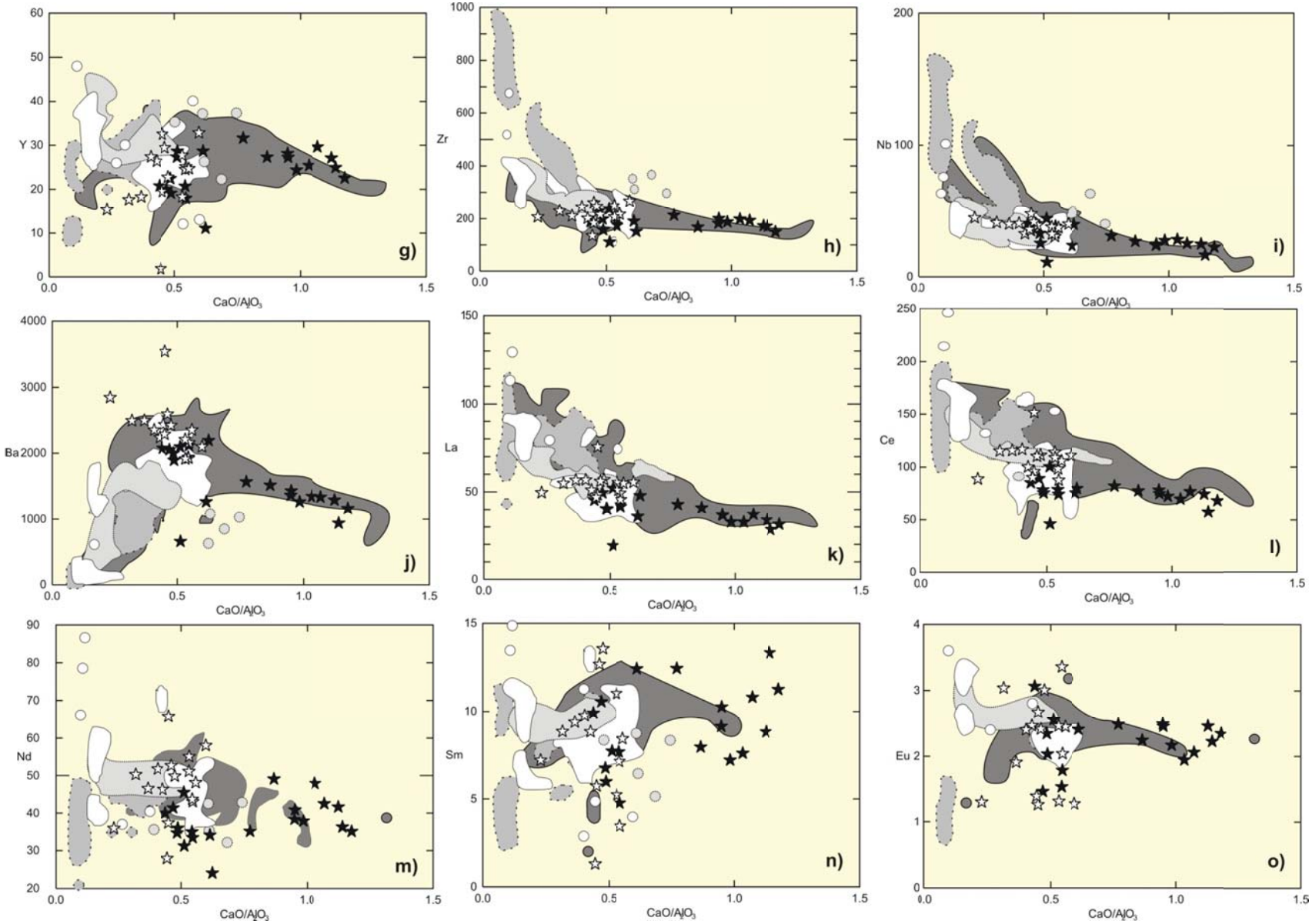

Figure 29. (cont.)

5.2.2. Inclusions in amphibole from the Type B nodule (NLM1-1d)

The compositions of multiphase inclusions in amphibole from Type B nodule (NLM1-1d) were compared with the host amphibole composition, with mica compositions from the same sample, and with Mt. Somma-Vesuvius bulk rock compositions (Fig. 30) in order to better constrain their petrogenesis. The major element compositions of the inclusions differ from all bulk rock compositions from Mt. Somma-Vesuvius (Fig. 30a-f). The inclusions have much higher Mg and K content but significantly lower Si and Na content. Their composition is much closer to the mica compositions than to any natural melt observed in the eruptive products of Mt. Somma-Vesuvius but the compositions of some elements (e.g., Mg, K, Ca) are even higher than the compositions of those elements in the mica. It is important to note that the anomalously high Mg content (up to 30 wt. % MgO) does not couple with high Cr content. In natural, primitive melts the Mg content is expected to correlate with the Cr content, as observed for the Mt. Somma-Vesuvius bulk rocks in which the rock with the highest Mg content has the highest Cr content, and Cr concentration decreases with decreasing Mg content (Fig. 30g). While the absolute concentrations of the elements, especially the major elements, depend greatly on the internal standard and the total used in data reduction (chapter 3.3.), trace element ratios should be unaffected. The trace element ratio variation diagrams (Fig. 30k-n) show that most of the inclusions plot more or less on a straight line between the composition of the host amphibole and the mica from the same sample. This suggests that the compositions of these inclusions can be derived by mixing amphibole and mica components and, perhaps, some amount of melt component, however, the end-member melt cannot be defined. The presence or absence of some amount of melt in the inclusion cannot be excluded or confirmed based on geochemistry. However, the presence of a dark grey phase adjacent to the mica and the bubble observed on SEM images suggests that, in some cases, some melt could have trapped along with the mica solid inclusion.

As described above, one of the inclusions has higher La, Ce and Zr concentration compared to the other inclusions. These characteristics cannot be explained by adding mica or amphibole components to the melt. The most plausible explanation is that the inclusion also trapped an apatite crystal. Petrographic observations confirm that in some cases the inclusions contain apatite, hence this interpretation is feasible and supported by observations. Bodnar and Student (2006) showed exaples of MI that trapped melt, melt + vapor, melt + feldspar, melt + apatite, melt + feldspar + apatite, so trapping multiple solids along with melt has been documented previously.

Some of the data (1-3 MI, depending on which element is plotted) that do not plot between the compositions of mica and amphibole but rather between or within the composition of Mt. Somma-Vesuvius bulk rock and amphibole. These inclusions might be MI that trapped only melt, but these were not studied further nor were more analyzed. Such inclusions are rare and even if enough could be found, their composition still cannot be precisely determined. The bulk rock composition of the rock is unknown, as well as its connection to the juvenile Mt. Somma-Vesuvius products. Therefore, identifying an appropriate internal standard would be difficult.

Little can be inferred about the origin of Type B nodule (NLM1-1d) without MI data. The mineral chemistry, however, indicates that Type B nodule formed from a melt containing less TiO_2, and perhaps more Sr and light REE, compared to those melts of which Type A nodules were formed.

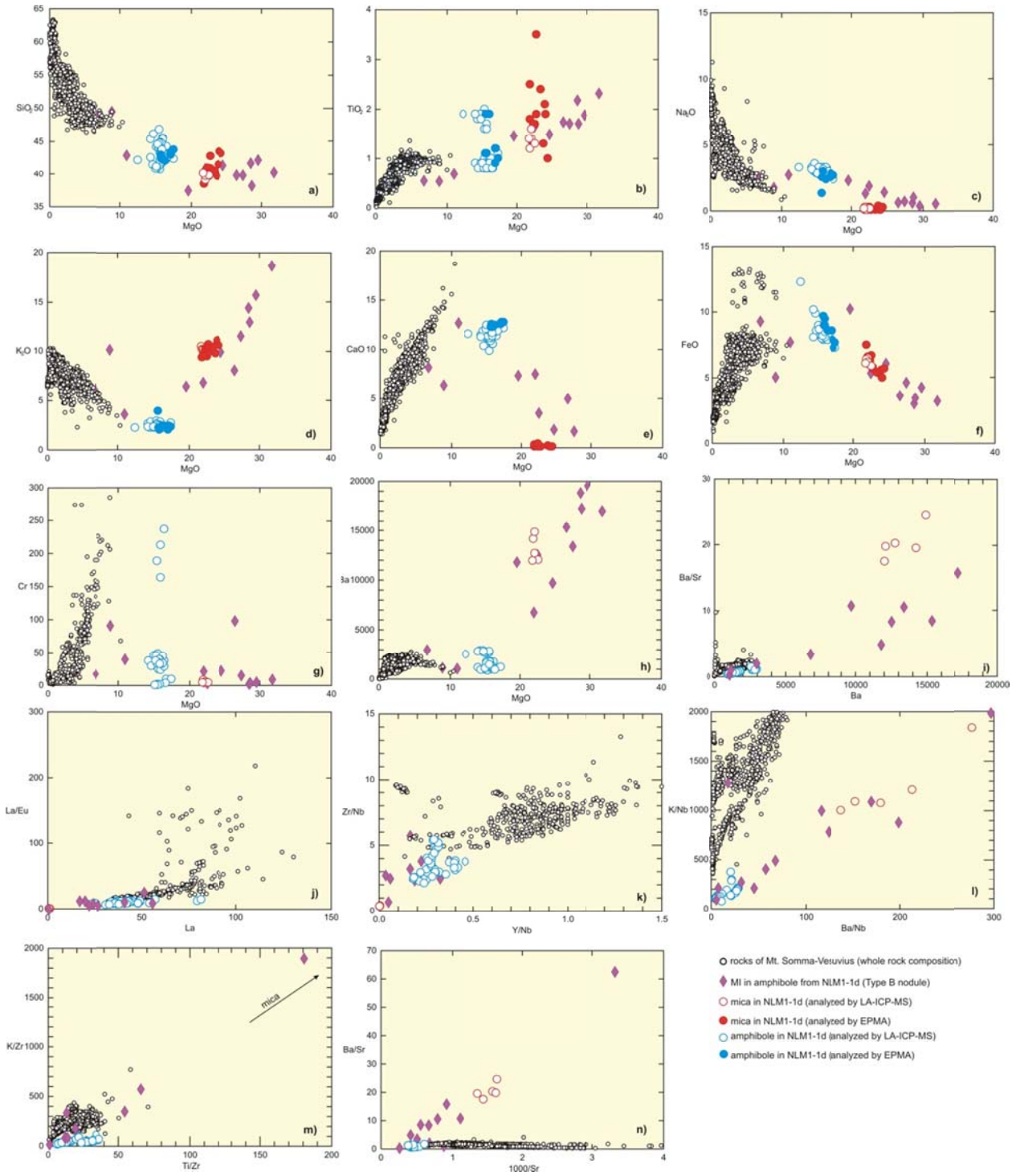

Figure 30. – Comparison of the compositions of inclusions in amphibole from Type B nodule (NLM1-1d) with their amphibole host, with mica from the same sample, and with the bulk rock composition of Mt. Somma-Vesuvius rocks on multi-element variation diagrams.

5.3. Pressure and temperature of formation of the nodules

One of the original goals of this research was to estimate the formation conditions of the nodules, and use this information to constrain the depth of magma chamber(s) during the early history of the Mt. Somma-Vesuvius volcanic system. The volatile content of the melt trapped in MI is pressure dependent; therefore, the volatile concentration can be used to estimate the trapping pressure. In addition, both types of nodules contain minerals or mineral assemblages that can be used as thermobarometers.

The goal was to use experimental data for H_2O and CO_2 solubilities in melts for example, as is used in the model developed by Papale *et al.* (2006), to estimate the pressure of trapping of the MI in clinopyroxene (NLM1-1a, Type A nodule). The model requires as input the composition of the MI, including H_2O and CO_2 concentrations, the melt temperature, an initial estimate of the weight fraction of H_2O in the system, and the pressure. The model also assumes that the melt is saturated in volatiles, otherwise it only provides a minimum pressure, not the actual trapping pressure. Evidence for volatile saturation was not observed in the samples of the Sarno (PB) eruption. For example, during the homogenization experiments the bubble was not the last phase that disappeared, suggesting that the melt was not saturated in volatiles. Therefore, the MI data only provide a minimum pressure. Due to the uniformly low H_2O content of the MI (generally less than 0.15 wt. %), the model (Papale *et al.*, 2006) failed to estimate the pressure, possibly because a melt with trachy-basaltic to trachy-andesitic composition must contain a higher amount of H_2O at volatile saturation. Thus, the volatile contents of the MI cannot be used to infer a trapping pressure because the melts are too "dry".

Several thermobarometers that are based on mineral composition, or on MI and its host composition, were also tested to estimate the pressure. As previously mentioned, sample NLM1-1d (Type B nodule) contains amphibole. Several thermobarometers are based on the co-crystallization of amphibole, more specifically hornblende and plagioclase (*e.g.*, Blundy and Holland, 1990; Holland and Blundy, 1994). These models were not used because, after extensive search, I found only two plagioclase crystals in the sample. There are also geobarometers that are based on only the composition of the amphibole and do not require the estimation of temperature. The model by Johnson and Rutherford (1989) estimates the pressure based on the Al content in the tetrahedral site of the amphibole. The accuracy of the method is ±0.5 kbar. This model was tested here, despite the fact that it was calibrated for hornblende in equilibrium with melt, fluid, biotite, quartz, sanidine, plagioclase, sphene and magnetite or ilmenite (Johnson and Rutherford, 1989). Based on compositions of eight amphibole crystals, the Johnson and Rutherford (1989) model predicted pressures ranging from 3.9 to 4.7 kbar. The model for the same equilibrium assemblage developed by Schmidt (1992) estimates pressure based on the total Al content of the amphibole. The precision of this model is ±0.6 kbar, and it predicted considerably higher pressure (6.5 to 7.3 kbar) for the same sample compared to the model of Johnson and Rutherford (1989). Ridolfi *et al.* (2010) and Ridolfi and Renzulli (2012) developed two models that estimate the pressure based on amphibole composition, and the model also estimates the temperature and oxygen fugacity and H_2O content of the melt based on the estimated pressure and amphibole composition. The first model was calibrated for calcic amphiboles in calc-alkaline magmas, the second model expands the earlier model to include alkaline magmas. The first model (Ridolfi *et al.*, 2010) gave a pressure of 2.2 to 4.3 kbar, with a maximum error of 0.5 kbar, based on compositions of eight amphiboles. The estimated temperature ranges from 891 to 1011 °C, and the one sigma error is 22

°C. The estimated oxygen fugacity is ΔNNO +1.3 to +2.0, the one sigma error of the estimate is 0.4 log units. The estimated H_2O content of the melt is 1.1-2.7 wt. %, with a maximum error of 0.4 wt. %. It is important to emphasize that this model was calibrated for calc-alkaline magmas, and the estimated P-T and T-$melt_{H2O}$ field is out of the stability field of amphiboles (Ridolfi *et al.*, 2010). The extended model by Ridolfi and Renzulli (2012) appears to be the only model that is suitable for sample NLM1-1d. Ridolfi and Renzulli (2012) provide the composition of the amphiboles and the host rock bulk composition that were used for the calibration. Only seven of the eight amphiboles from this study had compositions within the required range, and these seven compositions were also at the edge of the compositional range, due to their high K content. The pressure estimated by this model (Ridolfi and Renzulli, 2012) is remarkably higher than any of the other models tested, and ranges from 8.1 to 10.9 kbar, and in one case up to 14 kbar. The estimated temperature is 926-956 °C. The estimated oxygen fugacity (ΔNNO +7.2 to +9.3) and the estimated H_2O content of the melt (9.6 to 13.4 wt. %) are unrealistically high, and such extreme values have not yet been reported from Mt. Somma-Vesuvius to our knowledge. The one sigma uncertainty of the pressure estimate is 11.5%, of the temperature estimate is 23.5 °C, of the oxygen fugacity estimate is 0.37 log units, and of the H_2O content estimate is 0.78 wt. % (Ridolfi and Renzulli, 2012). If we plot the results against the data that were used for the calibration, it becomes clear that most of the results are out of the P-T and T-X_{H2O} field for which the model was calibrated (Fig. 31), and for all of the amphiboles the model predicted much higher oxygen fugacity than the model was calibrated for (not shown on figure). Therefore, the oxygen fugacity estimate certainly cannot be trusted, and perhaps neither the pressure estimate.

In summary, none of the pressure estimates obtained from the various models overlap. The first three models (Johnson and Rutherford, 1989; Ridolfi *et al.*, 2010; Schmidt, 1992) were not calibrated for such an alkaline system and high-K amphibole, and therefore the estimates from those models are likely inaccurate. In the case of the last model (Ridolfi and Renzulli, 2012), it is difficult to assess the reliability. The oxygen fugacity is most likely overestimated because it is out of the range of the experiments which were used for calibration. The pressure, temperature and H_2O-content might be incorrect, because the model might not be applicable to the compositions of the studied sample as for less alkaline compositions. However, if the estimates are accurate, it means that the amphibole crystallized at a pressure of at least 8 kbar, equivalent to ~24 km in depth.

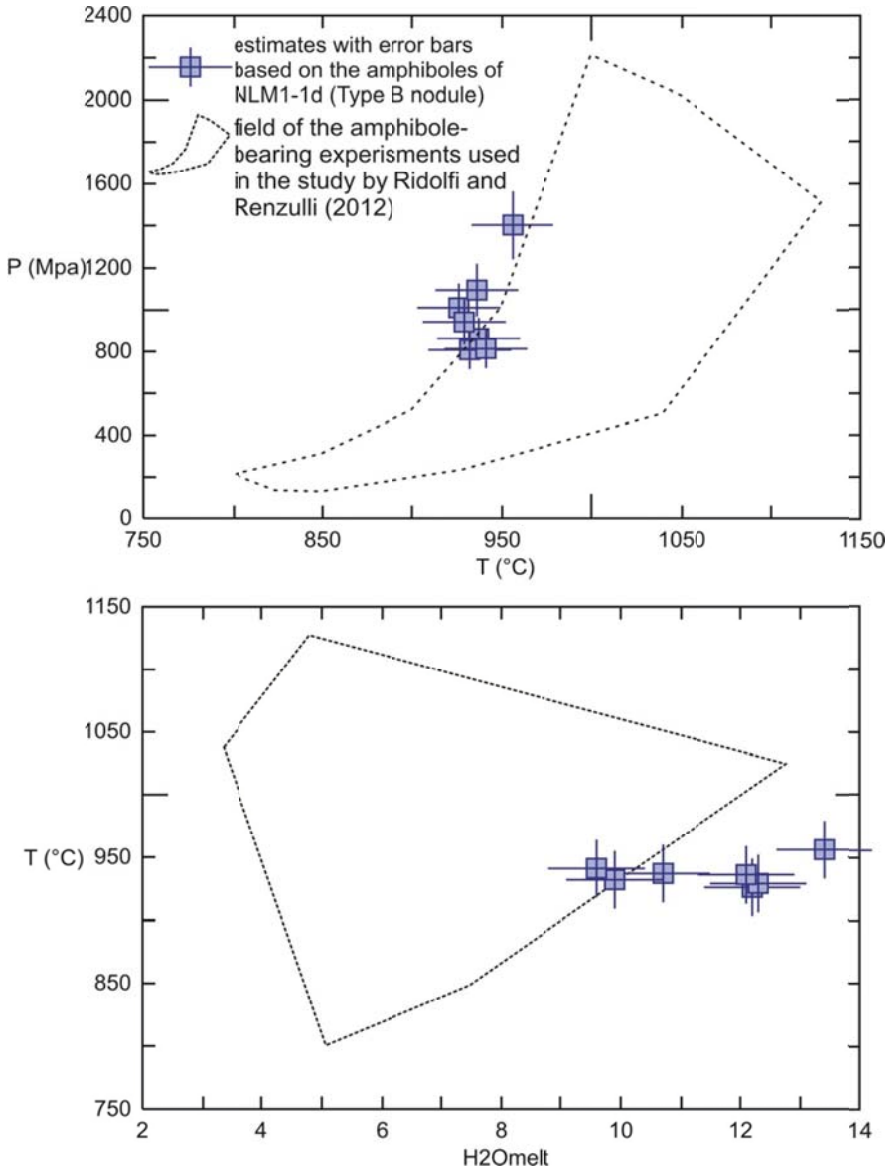

Figure 31. – P-T and T-H_2O_{melt} diagrams for comparison of the results of this study and the experiments selected for developing the model by Ridolfi and Renzulli (2012)

Clinopyroxenes and their MI compositions were used to estimate the formation conditions for Type A nodule NLM1-1a. The electronic attachment of the chapter by Putirka (2008), RiM69_Ch03_cpx_P-T.xls was used. It includes the previously published models of Putirka *et al.* (1996) and Putirka *et al.* (2003) as well as newer models. As discussed above, MI may have become enriched in their host clinopyroxene component as a result of overheating. Published models were unable to correct for overheating, and only those MI that had compositions closest to the equilibrium composition with their host were used. According to Putirka (2008), one way to test for equilibrium is to compare the Fe-Mg exchange coefficient ($K_D(Fe\text{-}Mg)^{cpx\text{-}liq}$) calculated from the MI and its host clinopyroxene composition to a constant value of 0.28±0.08 derived from 1245 experimental observations. Because the exchange coefficient can vary from 0.04-0.68, with a roughly normal distribution (Putirka, 2008), 18 MI-host pairs

where the Fe-Mg coefficient was lower than 0.40 were used here. Applying the various thermobarometer models on the selected MI-host pairs the temperature can be constrained with reasonable certainty, but the pressure varies within wide ranges. The model of Putirka *et al.* (1996) predicted a temperature between 1043 °C-1246 °C, with an average value of 1186 °C, while it predicts a pressure range of 1.2-16.3 kbar, the average is 6.1 kbar, with 10 out of 18 pairs falling between 4 and 8 kbar. The accuracy of the thermobarometer for a single pair is at least ±1.4 kbar and ±27K, and probably ±1.0 kbar and ±15K when averaged over multiple pairs (Putirka *et al.*, 1996). The model of Putirka *et al.* (2003) estimated temperatures of 980 °C to 1309 °C, with an average value of 1152 °C. The pressure calculations yielded negative values in two cases, which were not considered for the average calculations, which is 7.6 kbar. The estimated pressure, in this case, ranges from -2.8 to 11.6, and 11 out of 18 estimates are between 6 and 10 kbar. The standard error of the pressure estimate is 1.7 kbar, and for temperature it is 33 K (Putirka *et al.*, 2003). Several newer thermobarometer equations were also developed by Putirka (2008). Most of these require the input of the H_2O content of the liquid (MI). These equations were not used because the H_2O-content in most cases was not measured, and even, when it was, it appeared to be very low (≤0.15 wt. %) and it is unclear whether it is representative or not.

Putirka (2008) also developed a thermobarometer based on clinopyroxene composition only. Large number (212) of clinopyroxene compositions (several analyses from each crystal) were used to constrain the pressure and temperature of formation. The temperature estimate is in good agreement with the results of the previously mentioned thermometers. The estimated temperature of the clinopyroxenes from this study varies between 1019 °C and 1366 °C, with an average of 1184 °C. The pressure varies widely, from 1.6 to 24.8 kbar. Over half of the estimates fall between 4 and 8 kbar, with an average of 7.8 kbar. The standard error of estimate for pressure is ±3.1 kbar, and for temperature is ±58 °C (Putirka, 2008). In summary, clinopyroxene probably crystallized at slightly under 1200 °C. The pressure of clinopyroxene crystallization is not well constrained. Based on the results, clinopyroxenes crystallized in relatively deep magma chamber, most likely at ≥4 kbar but perhaps at ≥6 kbar, corresponding to a depth of at least 12 km.

The magma feeding system beneath Mt. Somma-Vesuvius consists of three main magma storage levels, the two deepest of which are probably long-lived reservoirs (Piochi *et al.*, 2006b). Isotopic, MI and FI data (Belkin and De Vivo, 1993; Belkin et al., 1985; Cioni, 2000; Lima et al., 2003; 2007; Marianelli et al., 1999; Piochi et al., 2006b) indicate a shallow reservoir at <5 km, which typically hosts the magmas that produce the plinian eruptions. A deeper magma chamber, located at about 8-12 km depth, supplies the interplinian and subplinian eruptions, whereas the deepest reservoir is located at >15 km. However, recent solubility data of volatiles in phonolitic-trachytic melts suggest, that the depths of the magma chambers (<5 km) supplying the plinian eruptions are underestimated (Webster et al., , submitted to J. Petrol.). Webster et al. (submitted) found that the accurate interpretation of previous MI compositions predict phenocryst crystallization and magma differentiation at pressures of ca. 350 - 600 MPa (3.5-6 kbar).

The deep structure of the plumbing system of the volcanic complex is supported by geophysical evidence as well (De Gori et al., 2001; De Natale et al., 2001; De Natale et al., 2006; Nunziata and Costanzo, 2010; Nunziata et al., 2006). A low velocity layer is recognized at ~15-35 km depth, which could be interpreted as the deep root for the shallow crustal magma chambers (De Gori et al., 2001; De Natale et al., 2001; De Natale et al., 2006; Nunziata et al., 2006).

The Type B nodule (NLM1-1d) containing amphibole might have sampled the deepest reservoir. Type A nodules likely sample the magma chamber at intermediate depth (8-12 km), or possibly also the deepest reservoir. If the results of the thermobarometry studies are reliable, then the PB-Sarno (PB) eruption was fed from magma chambers that are deeper than the magma chambers that supplied the other plinian eruptions (*e.g.*, 79 AD or Avellino). This is in partial agreement with the findings of Landi *et al.* (1999), who also predicted a deep magma chamber that fed the Sarno (PB) eruption but at slightly shallower depths of about 9-12 km. Due to the large variations in the estimated pressures, it cannot be stated with certainty whether a deeper reservoir already existed beneath Mt. Somma-Vesuvius prior the Sarno (PB) eruption, whether the samples came from the same reservoir that fed the main, "plinian phase" (Landi *et al.*, 1999) of the Sarno (PB) eruption. The results of this study is also in agreement with the findings of Webster et al. (submitted), which predicts at least 3.5 kbar (~10.5 km) for the depth of the plinian magma chambers.

6. Summary and conclusions

Four, “sub-effusive” nodules from the Sarno (PB) plinian eruption were examined in this study. All four nodules have porphyrogranular texture, but they differ in terms of modal composition. Three of the four nodules contain clinopyroxene and olivine as phenocrysts (Type A nodules), whereas one contains amphibole (Type B). The groundmass in both cases is fully crystallized, and fully crystallized melt pockets were also recognized in the interstitial space. The observed textural characteristics neither exclude nor prove the assumed crystal mush origin.

MI were observed in several phases within the nodules and were studied in clinopyroxene from a Type A nodule. All of the observed MI were crystallized indicating relatively slow cooling after entrapment. Two types of spatially associated MI were recognized. After the heating experiment, however, only one of the two types was found to be representative of the crystallizing melt (Type I). The composition of Type II inclusions is strongly modified by accidentally trapped An-rich feldspar. During the heating experiments some of the MI were slightly overheated, which enriched the MI in clinopyroxene components, but some differences and similarities with the bulk rock compositions of Mt. Somma-Vesuvius that cannot be explained by overheating were still recognized. The comparative study revealed that the MI are similar in bulk composition to the pre-Sarno, older Somma lava rocks, rather than the Sarno (PB) volcanics. Therefore, the NLM1-1a nodule and perhaps the other two Type A nodules are interpreted to have formed from the same melt or a melt with a composition similar to the melt erupted during the early history of Mt. Somma. The nodules were most likely already crystallized by the time they were incorporated into the upwelling magma of the Sarno (PB) eruption. Finding older, crystallized material in the younger eruptive products indicates that the Sarno (PB) magma erupted from the same, or from a deeper, magma chamber(s) that fed the older eruptions.

MI were also studied in amphibole from Type B nodules. The petrographic and geochemical studies revealed that the compositions of these inclusions are strongly modified by trapped phlogopite, and, sometimes apatite.

Although the “sub-effusive” type of nodule is usually interpreted as representing shallow plutonic rocks that have been entrained into the upwelling magma, thermobarometry calculations of these nodules predicted a deep origin. Unfortunately, the thermobarometer models that are available do not constrain the formation pressure of either type of nodules with high precision. Recognizing these limitations, the NLM1-1a nodule formed at a depth of at least 12 km, while Type B nodules formed at a depth of at least 24 km. These depths are not improbable considering our understanding of the plumbing system of Mt. Somma-Vesuvius. It suggests that the nodules sampled the intermediate or perhaps the deepest reservoirs of the underlying plumbing system. The data confirm that the Sarno (PB) eruption was fed from a greater depth the younger plinian eruptions, and the older, pre-Sarno eruptions may have also been sourced from these deeper magma chambers.

References

Anderson , A.T., 2003. An introduction to melt (glass±crystals) inclusions. In: I. Samson, A. Anderson and D. Marshall (Editors), Fluid inclusions: Analysis and Interpretation. Mineralogical Association of Canada, Short Course, pp. 353-364.

Andronico, D., Calderoni, G., Cioni, R., Sbrana, A., Sulpizio, R. and Santacroce, R., 1995. Geological map of Somma_Vesuvius volcano. Period. Mineral., 64: 77-78.

Ariskin, A.A., Frenkel, M.Y., Barmina, G.S. and Nielsen, R.L., 1993. Comagmat: a Fortran program to model magma differentiation processes. Comput. Geosci., 19(8): 1155-1170.

Arnó, V., Principe, C., Rosi, M., Santacroce, R., Sbrana, A. and Sheridan, M.F., 1987. Eruptive History. In: R. Santacroce (Editor), Somma-Vesuvius. CNR Quaderni Ricerca Scientifica, pp. 53-103.

Aulinas, M., Civetta, L., Di Vito, M., Orsi, G., Gimeno, D. and Férnandez-Turiel, J., 2008. The "Pomici di mercato" Plinian eruption of Somma-Vesuvius: magma chamber processes and eruption dynamics. Bull. Volcanol., 70(7): 825-840.

Ayuso, R.A., De Vivo, B., Rolandi, G., Seal, R.R. and Paone, A., 1998. Geochemical and isotopic (Nd-Pb-Sr-O) variations bearing on the genesis of volcanic rocks from Vesuvius, Italy. J. Volcanol. Geotherm. Res., 82(1-4): 53-78.

Balcone-Boissard, H., Boudon, G., Ucciani, G., Villemant, B., Cioni, R., Civetta, L. and Orsi, G., 2012. Magma degassing and eruption dynamics of the Avellino pumice Plinian eruption of Somma–Vesuvius (Italy). Comparison with the Pompeii eruption. Earth Planet. Sci. Lett., 331–332(0): 257-268.

Barberi, F., Bizouard, H., Clocchiatti, R., Metrich, N., Santacroce, R. and Sbrana, A., 1981. The Somma-Vesuvius magma chamber: a petrological and volcanological approach. Bull. Volcanol., 44(3): 295-315.

Barberi, F. and Leoni, L., 1980. Metamorphic carbonate ejecta from Vesuvius plinian eruptions: Evidence of the occurrence of shallow magma chambers. Bulletin Volcanologique, 43(1): 107-120.

Belkin, H.E. and De Vivo, B., 1993. Fluid inclusion studies of ejected nodules from plinian eruptions of Mt. Somma-Vesuvius. J. Volcanol. Geotherm. Res., 58(1-4): 89-100.

Belkin, H.E., De Vivo, B., Roedder, E. and Cortini, M., 1985. Fluid inclusion geobarometry from ejected Mt. Somma-Vesuvius nodules. Am. Mineral., 70: 288-303.

Belkin, H.E., De Vivo, B., Török, K. and Webster, J.D., 1998. Pre-eruptive volatile content, melt-inclusion chemistry, and microthermometry of interplinian Vesuvius lavas (pre-A.D. 1631). J. Volcanol. Geotherm. Res., 82(1–4): 79-95.

Belkin, H.E., Kilburn, C.R.J. and de Vivo, B., 1993. Sampling and major element chemistry of the recent (A.D. 1631-1944) Vesuvius activity. J. Volcanol. Geotherm. Res., 58(1-4): 273-290.

Bertagnini, A., Landi, P., Rosi, M. and Vigliargio, A., 1998. The Pomici di Base plinian eruption of Somma-Vesuvius. J. Volcanol. Geotherm. Res., 83(3-4): 219-239.

Black, S., Macdonald, R., DeVivo, B., Kilburn, C.R.J. and Rolandi, G., 1998. U-series disequilibria in young (A.D. 1944) Vesuvius rocks: Preliminary implications for magma residence times and volatile addition. J. Volcanol. Geotherm. Res., 82(1-4): 97-111.

Blundy, J.D. and Holland, T.J.B., 1990. Calcic amphibole equilibria and a new amphibole-plagioclase geothermometer. Contrib. Mineral. Petrol., 104(2): 208-224.

Bodnar, R.J., 2003. Introduction to fluid inclusions. In: I. Samson, A. Anderson and D. Marshall (Editors), Fluid inclusions: Analysis and Interpretation. Mineralogical Association of Canada, Short Course, pp. 1-8.

Bodnar, R.J. and Student, J.J., 2006. Melt inclusion in plutonic rocks: petrography and microthermometry. In: J.D. Webster (Editor), Melt inclusions in plutonic rocks. Short Course Series Volume. Mineralogical Association of Canada, pp. 1-25.

Botcharnikov, R.E., Behrens, H., Holtz, F., Koepke, J. and Sato, H., 2004. Sulfur and chlorine solubility in Mt. Unzen rhyodacitic melt at 850 °C and 200 MPa. Chem. Geol., 213(1-3): 207-225.

Brocchini, D., Principe, C., Castradori, D., Laurenzi, M.A. and Gorla, L., 2001. Quaternary evolution of the southern sector of the Campanian Plain and early Somma-Vesuvius activity: insights from the Trecase 1 well. Mineral. Petrol., 73(1): 67-91.

Bruno, P.P.G., Cippitelli, G. and Rapolla, A., 1998. Seismic study of the Mesozoic carbonate basement around Mt. Somma-Vesuvius, Italy. J. Volcanol. Geotherm. Res., 84(3-4): 311-322.

Carroll, M.R. and Webster, J.D., 1994. Solubility of sulfur, noble gases, nitrogen, chlorine, and fluorine in magmas. In: M.R. Carroll and J.R. Holloway (Editors), Volatiles in magmas. Mineralogical Society of America, Washington, D.C., pp. 231-279.

Cella, F., Fedi, M., Florio, G., Grimaldi, M. and Rapolla, A., 2007. Shallow structure of the Somma-Vesuvius volcano from 3D inversion of gravity data. J. Volcanol. Geotherm. Res., 161: 303-217.

Cioni, R., 2000. Volatile content and degassing processes in the AD 79 magma chamber at Vesuvius (Italy). Contrib. Mineral. Petrol., 140(1): 40-54.

Cioni, R., Civetta, L., Marianelli, P., Metrich, N., Santacroce, R. and Sbrana, A., 1995. Compositional Layering and Syn-eruptive Mixing of a Periodically Refilled Shallow Magma Chamber: the AD 79 Plinian Eruption of Vesuvius. J. Petrol., 36(3): 739-776.

Cioni, R., Marianelli, P. and Santacroce, R., 1998. Thermal and compositional evolution of the shallow magma chambers of Vesuvius, evidence from pyroxene phenocrysts and melt inclusions. J. Geophys. Res., 103(B8): 18277-18294.

Cioni, R., Santacroce, R. and Sbrana, A., 1999. Pyroclastic deposits as a guide for reconstructing the multi-stage evolution of the Somma-Vesuvius caldera. Bull. Volcanol., 61: 207-222.

Cioni, R., Sulpizio, R. and Garruccio, N., 2003. Variability of the eruption dynamics during a Subplinian event: the Greenish Pumice eruption of Somma-Vesuvius (Italy). J. Volcanol. Geotherm. Res., 124(1-2): 89-114.

Civetta, L., Galati, R. and Santacroce, R., 1991. Magma mixing and convective compositional layering within the Vesuvius magma chamber. Bull. Volcanol., 53(4): 287-300.

Civetta, L. and Santacroce, R., 1992. Steady stata magma supply in the last 3400 years of Vesuvius activity. Acta Vulcanologica, 2: 147-159.

Cortini, M., Lima, A. and De Vivo, B., 1985. Trapping temperatures of melt inclusions from ejected Vesuvian mafic xenoliths. J. Volcanol. Geotherm. Res., 26(1-2): 167-172.

Cundari, A., 1982. Petrology of clinopyroxenite ejecta from Somma-Vesuvius and their genetic implications. Tscherm. Mineral. Petrogr. Mitt., 30(1): 17-35.

Danyushevsky, L.V., Leslie, R.A.J., Crawford, A. and Durance, P., 2004. Melt Inclusions in Primitive Olivine Phenocrysts: the Role of Localized Reaction Processes in the Origin of Anomalous Compositions. J. Petrol., 45(12): 2531-2553.

Danyushevsky, L.V. and Lima, A., 2001. Relationship between Campi Flegrei and Mt. Somma volcanism: evidence from melt inclusions in clinopyroxene phenocrysts from volcanic breccia xenoliths. Mineral. Petrol., 73: 107-119.

Danyushevsky, L.V., McNeill, A.W. and Sobolev, A.V., 2002. Experimental and petrological studies of melt inclusions in phenocrysts from mantle-derived magmas: an overview of techniques, advantages and complications. Chem. Geol., 183(1-4): 5-24.

Danyushevsky, L.V. and Plechov, P., 2011. Petrolog3: Integrated software for modeling crystallization processes. Geochem. Geophys. Geosyst., 12(7): n/a-n/a.

De Gori, P., Cimini, G.B., Chiarabba, C., De Natale, G., Troise, C. and Deschamps, A., 2001. Teleseismic tomography of the Campanian volcanic area and surrounding Apenninic belt. J. Volcanol. Geotherm. Res., 109(1–3): 55-75.

De Natale, G., Troise, C., Pingue, F., De Gori, P. and Chiarabba, C., 2001. Structure and dynamics of the Somma-Vesuvius volcanic complex. Mineral. Petrol., 73(1): 5-22.

De Natale, G., Troise, C., Pingue, F., Mastrolorenzo, G. and Pappalardo, L., 2006. The Somma-Vesuvius volcano (Southern Italy): Structure, dynamics and hazard evaluation. Earth-Science Reviews, 74(1-2): 73-111.

De Natale, G., Troise, C., Trigila, R., Dolfi, D. and Chiarabba, C., 2004. Seismicity and 3-D substructure at Somma-Vesuvius volcano: evidence for magma quenching. Earth Planet. Sci. Lett., 221(1-4): 181-196.

De Vivo, B., Lima, A., Kamenetsky, V.S. and Danyushevsky, L.V., 2006. Fluid and melt inclusions in the sub-volcanic environments from volcanic systems: Examples from the Neapolitan area and Pontine Islands, Italy, Mineralogical Association of Canada Short Course 36, Montreal, Quebec, pp. 211-237.

De Vivo, B., Petrosino, P., Lima, A., Rolandi, G. and Belkin, H., 2010. Research progress in volcanology in the Neapolitan area, southern Italy: a review and some alternative views. Mineral. Petrol., 99(1): 1-28.

De Vivo, B., Rolandi, G., Gans, P.B., Calvert, A., Bohrson, W.A., Spera, F.J. and Belkin, H.E., 2001. New constraints on the pyroclastic eruptive history of the Campanian volcanic Plain (Italy). Mineral. Petrol., 73(1): 47-65.

Del Moro, A., Fulignati, P., Marianelli, P. and Sbrana, A., 2001. Magma contamination by direct wall rock interaction: constraints from xenoliths from the walls of a carbonate-hosted magma chamber (Vesuvius 1944 eruption). J. Volcanol. Geotherm. Res., 112(1-4): 15-24.

Delibrias, G., Di Paola, G.M., Rosi, M. and Santacroce, R., 1979. La storia eruttiva del comlesso vulcanico Somma Vesuvio ricostruita dalle successioni piroclastiche del Monte Somma. Rend. Soc. Ital. Mineral. Petrol., 35: 411-438.

Di Renzo, V., Di Vito, M.A., Arienzo, I., Carandente, A., Civetta, L., D'antonio, M., Giordano, F., Orsi, G. and Tonarini, S., 2007. Magmatic History of Somma–Vesuvius on the Basis of New Geochemical and Isotopic Data from a Deep Borehole (Camaldoli della Torre). J. Petrol., 48(4): 753-784.

Di Vito, M.A., Sulpizio, R., Zanchetta, G. and D'Orazio, M., 2008. The late Pleistocene pyroclastic deposits of the Campanian Plain: New insights into the explosive activity of Neapolitan volcanoes. J. Volcanol. Geotherm. Res., 177(1): 19-48.

Esposito, R., Bodnar, R.J., Danyushevsky, L.V., De Vivo, B., Fedele, L., Hunter, J., Lima, A. and Shimizu, N., 2011. Volatile Evolution of Magma Associated with the Solchiaro Eruption in the Phlegrean Volcanic District (Italy). J. Petrol., 52(12): 2431-2460.

Esposito, R., Bodnar, R.J., Hunter, J. and De Vivo, B., 2010. Do melt inclusions record the pre-eruptive volatile content of magmas?, PanAmerican Current Research on Fluid Inclusions, University of Nevada Las Vegas, Las Vegas, Nevada, U.S.A. June 8-10. 2010., pp. 1-2.

Esposito, R., Klebesz, R., Bartoli, O., Klyukin, Y., Moncada, D., Doherty, A. and Bodnar, R., 2012. Application of the Linkam TS1400XY heating stage to melt inclusion studies. Central European Journal of Geosciences, 4(2): 208-218.

Frezzotti, M.L., Tecce, F. and Casagli, A., 2012. Raman spectroscopy for fluid inclusion analysis. J. Geochem. Explor., 112(0): 1-20.

Fulignati, P., Kamenetsky, V.S., Marianelli, P. and Sbrana, A., 2005. Fluid inclusion evidence of second immiscibility within magmatic fluids (79 AD eruption of Mt. Vesuvius). Periodico di Mineralogia, 74(1): 43-54.

Fulignati, P., Kamenetsky, V.S., Marianelli, P., Sbrana, A. and Mernagh, T.P., 2001. Melt inclusion record of immiscibility between silicate, hydrosaline, and carbonate melts: Applications to skarn genesis at Mount Vesuvius. Geology, 29(11): 1043-1046.

Fulignati, P. and Marianelli, P., 2007. Tracing volatile exsolution within the 472 AD "Pollena" magma chamber of Vesuvius (Italy) from melt inclusion investigation. J. Volcanol. Geotherm. Res., 161(4): 289-302.

Fulignati, P., Marianelli, P., Santacroce, R. and Sbrana, A., 2000. The skarn shell of the 1944 Vesuvius magma chamber. Genesis and P-T-X conditions from melt and fluid inclusion data. Eur. J. Mineral., 12: 1025-1039.

Fulignati, P., Marianelli, P., Santacroce, R. and Sbrana, A., 2004. Probing the Vesuvius magma chamber-host rock interface through xenoliths. Geol. Mag., 141(4): 417-428.

Fulignati, P., Marianelli, P. and Sbrana, A., 1998. New insights on the thermometamorphic-metasomatic magma chamber shell of the 1944 eruption of Vesuvius. Acta Vulcanologica, 10(1): 47-54.

Giaccio, B., Isaia, R., Fedele, F.G., Di Canzio, E., Hoffecker, J., Ronchitelli, A., Sinitsyn, A.A., Anikovich, M., Lisitsyn, S.N. and Popov, V.V., 2008. The Campanian Ignimbrite and Codola tephra layers: Two temporal/stratigraphic markers for the Early Upper Palaeolithic in southern Italy and eastern Europe. J. Volcanol. Geotherm. Res., 177(1): 208-226.

Gilg, H.A., Lima, A., Somma, R., Belkin, H.E., De Vivo, B. and Ayuso, R.A., 2001. Isotope geochemistry and fluid inclusion study of skarns from Vesuvius. Mineral. Petrol., 73(1): 145-176.

Goldstein, R.H. and Reynolds, T.J., 1994. Systematics of fluid inclusions in diagenetic minerals. SEPM, 199 pp.

Gunther, D., Audetat, A., Frischknecht, R. and A. Heinrich, C., 1998. Quantitative analysis of major, minor and trace elements in fluid inclusions using laser ablation-inductively coupled plasmamass spectrometry. J. Anal. At. Spectrom., 13(4): 263-270.

Halter, W.E., Heinrich, C.A. and Pettke, T., 2004. Laser-ablation ICP-MS analysis of silicate and sulfide melt inclusions in an andesitic complex II: evidence for magma mixing and magma chamber evolution. Contrib. Mineral. Petrol., 147(4): 397-412.

Halter, W.E., Pettke, T., Heinrich, C.A. and Rothen-Rutishauser, B., 2002. Major to trace element analysis of melt inclusions by laser-ablation ICP-MS: methods of quantification. Chem. Geol., 183(1-4): 63-86.

Heinrich, C.A., Pettke, T., Halter, W.E., Aigner-Torres, M., Audétat, A., Günther, D., Hattendorf, B., Bleiner, D., Guillong, M. and Horn, I., 2003. Quantitative multi-element analysis of minerals, fluid and melt inclusions by laser-ablation inductively-coupled-plasma mass-spectrometry. Geochim. Cosmochim. Acta, 67(18): 3473-3497.

Helo, C., Longpre, M.A., Shimizu, N., Clague, D.A. and Stix, J., 2011. Explosive eruptions at mid-ocean ridges driven by CO_2-richmagmas. Nat. Geosci., 4: 260-263.

Hermes, O.D. and Cornell, W.C., 1978. Petrochemical significance of xenolithic nodules associated with potash-rich lavas of Somma-Vesuvius volcano. NSF final technical report, University of Rhode Island.

Hermes, O.D. and Cornell, W.C., 1981. Quenched crystal mush and associated magma compositions as indicated by intercumulus glasses from Mt. Vesuvius, Italy. J. Volcanol. Geotherm. Res., 9(2-3): 133-149.

Hermes, O.D. and Cornell, W.C., 1983. The significance of mafic nodules in the ultra-potassic rocks from central Italy - reply. J. Volcanol. Geotherm. Res., 16(1–2): 166-172.

Hervig, R.L., Mazdab, F.K., Moore, G. and McMillan, P.F., 2003. Analyzing hydrogen (H_2O) in silicate glass by secondary ion mass spectrometry and reflectance Fourier transform infrared spectroscopy. In: B. De Vivo and R.J. Bodnar (Editors), Melt Iclusions in Volcanic Systems: Methods, Applications, Problems. Development in Volcanology. Elsevier Press, Amsterdam, pp. 83-103.

Holland, T. and Blundy, J., 1994. Non-ideal interactions in calcic amphiboles and their bearing on amphibole-plagioclase thermometry. Contrib. Mineral. Petrol., 116(4): 433-447.

Holloway, J.R. and Blank, J.G., 1994. Application of experimental results to C-O-H species in natural melts. In: M.R. Carroll and J.R. Holloway (Editors), Volatiles in magmas. Mineralogical Society of America, Washington, D.C., pp. 187-230.

Johnson, M.C. and Rutherford, M.J., 1989. Experimental calibration of the aluminum-in-hornblende geobarometer with application to Long Valley caldera (California) volcanic rocks. Geology, 17(9): 837-841.

Joron, J.L., Metrich, N., Rosi, M., Santacroce, R., Sbrana, A. and METRICH N., R.M., SANTACROCE R., SBRANA A. ; CHEMISTRY AND PETROGRAPHY| SOMMA VESUVIUS (SANTACROCE, R. (ED.)), CNR, QUADERNI DE LA RICERCA SCIENTIFICA, ROMA 114 NO. 8 [1987] 105-174, 1987. Chemistry and Petrography In: R. Santacroce (Editor), Somma-Vesuvius. CNR Quad. Ric. Sci. , Roma, pp. 105-174.

Kamenetsky, V.S., Naumov, V.B., Davidson, P., van Achterbergh, E. and Ryan, C.G., 2004. Immiscibility between silicate magmas and aqueous fluids: a melt inclusion pursuit into the magmatic-hydrothermal transition in the Omsukchan Granite (NE Russia). Chem. Geol., 210(1–4): 73-90.

Klébesz, R., Bodnar, R., De Vivo, B., Török, K., Lima, A. and Petrosino, P., 2012. Composition and origin of nodules from the ≈20 ka Pomici di Base (PB)-Sarno eruption of Mt. Somma — Vesuvius, Italy. Central European Journal of Geosciences, 4(2): 324-337.

Landi, P., Bertagnini, A. and Rosi, M., 1999. Chemical zoning and crystallization mechanisms in the magma chamber of the Pomici di Base plinian eruption of Somma-Vesuvius (Italy). Contrib. Mineral. Petrol., 135(2): 179-197.

Le Bas, M.J., Le Maitre, R.W., Streckeisen, A. and Zanettin, B., 1986. A chemical classification of volcanic rocks based on the total alkali-silica diagram. J. Petrol., 27: 745-750.

Leake, B.E., Woolley, A.R., Arps, C.E.S., Brich, W.D., Gilbert, M.C., Grice, J.D., Hawthorne, F.C., Kato, A., Kisch, H.J., G., K.V., Kees, L., Laird, J., Mandarino, J.A., Maresch, W.V., Nickel, E.H., Rock, N.M.S., Schumacher, J.C., Smith, D.C., Stephenson, N.C.N., Ungaretti, L., Whittaker, E.J.W. and Youzhi, G., 1997. Nomenclature of amphiboles: report of the subcommittee on amphiboles of the International Mineralogical Assiciation, Commission on new minerals and mineral names. The Canadian Mineralogist, 35: 219-246.

Lima, A., Belkin, H.E. and Török, K., 1999. Understanding Vesuvius magmatic processes: evidence from primitive silicate-melt inclusions in medieval scoria clinopyroxenes (Terzigno Formation). Mineral. Petrol., 65(3): 185-206.

Lima, A., Danyushevsky, L.V., De Vivo, B. and Fedele, L., 2003. A model for the evolution of the Mt. Somma-Vesuvius magmatic system based on fluid and melt inclusion investigations. In: B. De Vivo and R.J. Bodnar (Editors), Melt Inclusions in Volcanic Systems: Methods, Applications, Problems. Developments in Volcanology. Elsevier Press, Amsterdam, pp. 227-249.

Lima, A., De Vivo, B., Fedele, L., Sintoni, F. and Milia, A., 2007. Geochemical variations between the 79 AD and 1944 AD Somma-Vesuvius volcanic products: Constraints on the evolution of the hydrothermal system based on fluid and melt inclusions. Chem. Geol., 237(3-4): 401-417.

Lowenstern, J.B., 2003. Melt Inclusions Come of Age: Volatiles, Volcanoes and Sorby's Legacy. In: B. De Vivo and R.J. Bodnar (Editors), Melt Iclusions in Volcanic Systems: Methods, Applications, Problems. Development in Volcanology. Elsevier Press, Amsterdam, pp. 1-22.

Marianelli, P., Metrich, N., Santacroce, R. and Sbrana, A., 1995. Mafic magma batches at Vesuvius: a glass inclusion approach to the modalities of feeding stratovolcanoes. Contrib. Mineral. Petrol., 120(2): 159-169.

Marianelli, P., Métrich, N. and Sbrana, A., 1999. Shallow and deep reservoirs involved in magma supply of the 1944 eruption of Vesuvius. Bull. Volcanol., 61(1): 48-63.

Marianelli, P., Sbrana, A., Métrich, N. and Cecchetti, A., 2005. The deep feeding system of Vesuvius involved in recent violent strombolian eruptions. Geophys. Res. Lett., 32(2): L02306.

Marini, L., Chiappini, V., Cioni, R., Cortecci, G., Dinelli, E., Principe, C. and Ferrara, G., 1998. Effect of degassing on sulfur contents and $\delta^{34}S$ values in Somma-Vesuvius magmas. Bull. Volcanol., 60(3): 187-194.

Mastrolorenzo, G., Munno, R. and Rolandi, G., 1993. Vesuvius 1906: a case study of paroxymal eruption and its relation to eruption cycles. J. Volcanol. Geotherm. Res., 58: 217-237.

McDonough, W.F. and Sun, S.-s., 1995. The composition of the Earth. Chem. Geol., 120(3-4): 223-253.

Moore, G., 2008. Interpreting H_2O and CO_2 Contents in Melt Inclusions: Constraints from Solubility Experiments and Modeling. In: K.D. Putirka and F.J. Tepley III (Editors), Minerals, Inclusions and Volcanic Processes, pp. 333-361.

Mues-Schumacher, U., 1994. Chemical variation of the A.D. 79 pumice deposits of Vesuvius. Eur. J. Mineral., 6: 387-395.

Mutchler, S., Fedele, L. and Bodnar, R.J., 2008. Analysis Management System (AMS) for reduction of laser ablation ICPMS data. In: P. Sylvester (Editor), Laser-Ablation-ICPMS in the Earth Sciences: Current Practices and Outstanding Issues. Mineralogical Association of Canada, Vancouver, BC, pp. 318-327.

Newman, S. and Lowenstern, J.B., 2002. VolatileCalc: a silicate melt–H_2O–CO_2 solution model written in Visual Basic for excel. Comput. Geosci., 28: 597-604.

Norman, M.D., Pearson, N.J., Sharma, A. and Griffin, W.L., 1996. Quantitative analysis of trace elements in geological materials by laser ablation ICPMS: Instrumental Operating Conditions and Calibration Values of NIST Glasses. Geostand. Newslett., 20(2): 247-261.

Nunziata, C. and Costanzo, M., 2010. Low VS crustal zones in the Campanian Plain (Southern Italy). Mineral. Petrol., 100(3): 215-225.

Nunziata, C., Natale, M., Luongo, G. and F. Panza, G., 2006. Magma reservoir at Mt. Vesuvius: Size of the hot, partially molten, crust material detected deeper than 8 km. Earth Planet. Sci. Lett., 242(1–2): 51-57.

Paone, A., 2006. The geochemical evolution of the Mt. Somma-Vesuvius volcano. Mineral. Petrol., 87(1): 53-80.

Paone, A., 2008. Fractional crystallization models and B–Be–Li systematics at Mt Somma-Vesuvius volcano (Southern Italy). Int. J. Earth Sci., 97(3): 635-650.

Papale, P., Moretti, R. and Barbato, D., 2006. The compositional dependence of the saturation surface of H_2O + CO_2 fluids in silicate melts. Chem. Geol., 229(1-3): 78-95.

Piochi, M., Ayuso, R.A., De Vivo, B. and Somma, R., 2006a. Crustal contamination and crystal entrapment during polybaric magma evolution at Mt. Somma-Vesuvius volcano, Italy: Geochemical and Sr isotope evidence. Lithos, 86(3-4): 303-329.

Piochi, M., De Vivo, B. and Ayuso, R.A., 2006b. The magma feeding system of Somma-Vesuvius (Italy) strato-volcano: new inferences from a review of geochemical and Sr, Nd, Pb and O isotope data. In: B. De Vivo (Editor), Volcanism in the Campania Plain: Vesuvius, Campi Flegrei and Ignimbrites. Elsevier B. V., pp. Chapter 9: 181-202.

Putirka, K., 2008. Thermometers and Barometers for Volcanic Systems. In: K. Putirka and F.J. Tepley III (Editors), Minerals, inclusions and volcanic processes. Reviews in Mineralogy & Geochemistry. Mineralogical Society of America, pp. 61-120.

Putirka, K., Johnson, M.C., Kinzler, R. and Walker, D., 1996. Thermobarometry of mafic igneous rocks based on clinopyroxene-liquid equilibria, 0-30 kbar. Contrib. Mineral. Petrol., 123: 92-108.

Putirka, K.D., Mikaelian, H., Ryerson, F. and Shaw, H., 2003. New clinopyroxene-liquid thermobarometers for mafic, evolved, and volatile-bearing lava compositions, with applications to lavas from Tibet and the Snake River Plain, Idaho. Am. Mineral., 88(10): 1542-1554.

Raia, F., Webster, J.D. and De Vivo, B., 2000. Pre-eruptive volatile contents of Vesuvius magmas: constraints on eruptive history and behavior. I - The medieval and modern interplinian activities. Eur. J. Mineral., 12: 179-193.
Ridolfi, F. and Renzulli, A., 2012. Calcic amphiboles in calc-alkaline and alkaline magmas: thermobarometric and chemometric empirical equations valid up to 1,130°C and 2.2 GPa. Contrib. Mineral. Petrol., 163(5): 877-895.
Ridolfi, F., Renzulli, A. and Puerini, M., 2010. Stability and chemical equilibrium of amphibole in calc-alkaline magmas: an overview, new thermobarometric formulations and application to subduction-related volcanoes. Contrib. Mineral. Petrol., 160(1): 45-66.
Roedder, E., 1979. Origin and significance of magmatic inclusions. Bull. Mineral., 102: 487-510.
Roedder, E., 1984. Fluid inclusions. Mineral. Soc. Amer., 643 pp.
Roedder, E., 1992. Fluid inclusion evidence for immiscibility in magmatic differentiation. Geochim. Cosmochim. Acta, 56: 5-20.
Roedder, E. and Bodnar, R.J., 1980. Geologic pressure determinations from fluid inclusion studies. Annual Review of Earth and Planetary Sciences, 8: 263-301.
Rolandi, G., 1997. The eruptive history of Somma-Vesuvius. In: M. Cortini and B. De Vivo (Editors), Volcanism and Archeology in Mediterranean Area. Reserch Signpost. Trivandrum, pp. 77-88.
Rolandi, G., Barrella, A.M. and Borrelli, A., 1993a. The 1631 eruption of Vesuvius. J. Volcanol. Geotherm. Res., 58(1–4): 183-201.
Rolandi, G., Bellucci, F. and Cortini, M., 2004. A new model for the formation of the Somma Caldera. Mineral. Petrol., 80(1): 27-44.
Rolandi, G., Bellucci, F., Heizler, M.T., Belkin, H.E. and De Vivo, B., 2003. Tectonic controls on the genesis of ignimbrites from the Campanian Volcanic Zone, southern Italy. Mineral. Petrol., 79(1): 3-31.
Rolandi, G., Maraffi, S., Petrosino, P. and Lirer, L., 1993b. The Ottaviano eruption of Somma-Vesuvius (3760y BP): a magmatic alternating fall and flow-forming eruption. J. Volcanol. Geotherm. Res., 58: 43-65.
Rolandi, G., Petrosino, P. and Mc Geehin, J., 1998. The interplinian activity at Somma-Vesuvius in the last 3500 years. J. Volcanol. Geotherm. Res., 82(1-4): 19-52.
Rosi, M. and Santacroce, R., 1983. The 472 A.D. 'Pollena' eruption: volcanological and petrological data for this poorly known plinian-type event at Vesuvius. J. Volcanol. Geotherm. Res., 17: 249-271.
Ryan, C.G., Heinrich, C.A., van Achterbergh, E., Ballhaus, C. and Mernagh, T.P., 1995. Microanalysis of ore-forming fluids using the scanning proton microprobe. Nuclear Instruments and Methods in Physics Research Section B: Beam Interactions with Materials and Atoms, 104(1–4): 182-190.
Santacroce, R. (Editor), 1987. Somma-Vesuvius. CNR Quaderni della Ricerca Scientifica 114, 251 pp.
Santacroce, R., Bertagnini, A., Civetta, L., Landi, P. and Sbrana, A., 1993. Eruptive dynamics and petrogenetic processes in a very shallow magma reservoir: The 1906 eruption of Vesuvius. J. Petrol., 34: 383-425.
Santacroce, R., Cioni, R., Marianelli, P., Sbrana, A., Sulpizio, R., Zanchetta, G., Donahue, D.J. and Joron, J.L., 2008. Age and whole rock-glass compositions of proximal pyroclastics from the major explosive eruptions of Somma-Vesuvius: A review as a tool for distal tephrostratigraphy. J. Volcanol. Geotherm. Res., 177(1): 1-18.
Savelli, C., 1968. The problem of rock assimilation by Somma-Vesuvius magma. Contrib. Mineral. Petrol., 18(1): 43-64.
Schiano, P., Clocchiatti, R., Ottolini, L. and Sbrana, A., 2004. The relationship between potassic, calc-alkaline and Na-alkaline magmatism in South Italy volcanoes: A melt inclusion approach. Earth Planet. Sci. Lett., 220(1-2): 121-137.
Schmidt, M.W., 1992. Amphibole composition in tonalite as a function of pressure: an experimental calibration of the Al-in-hornblende barometer. Contrib. Mineral. Petrol., 110(2): 304-310.

Siani, G., Sulpizio, R., Paterne, M. and Sbrana, A., 2004. Tephrostratigraphy study for the last 18,000 ^{14}C years in a deep-sea sediment sequence for the South Adriatic. Quat. Sci. Rev., 23: 2485-2500.

Somma, R., Ayuso, R.A., De Vivo, B. and Rolandi, G., 2001. Major, trace element and isotope geochemistry (Sr-Nd-Pb) of interplinian magmas from Mt. Somma-Vesuvius (Southern Italy). Mineral. Petrol., 73(1): 121-143.

Sorby, H.C., 1858. On the Microscopical, Structure of Crystals, indicating the Origin of Minerals and Rocks. Quarterly Journal of the Geological Society, 14(1-2): 453-500,.

Sulpizio, R., Cioni, R., Di Vito, M., Mele, D., Bonasia, R. and Dellino, P., 2010. The Pomici di Avellino eruption of Somma-Vesuvius (3.9 ka BP). Part I: stratigraphy, compositional variability and eruptive dynamics. Bull. Volcanol., 72(5): 539-558.

Sulpizio, R., Zanchetta, G., Paterne, M. and Siani, G., 2003. A review of tephrostratigraphy in central and southern Italy during the last 65 ka. Il Quaternario, 16: 91-108.

Thomas, J.B. and Bodnar, R.J., 2002. A technique for mounting and polishing melt inclusions in small (<1mm) crystals. Am. Mineral., 87: 1505-1508.

Thomas, R., 2000. Determination of water contents of granite melt inclusions by confocal laser Raman microprobe spectroscopy. Am. Mineral., 85: 868-872.

Vaggelli, G., De Vivo, B. and Trigila, R., 1993. Silicate-melt inclusions in recent Vesuvius lavas (1631-1944): II. Analytical chemistry. J. Volcanol. Geotherm. Res., 58(1-4): 367-376.

Varekamp, J.C., 1983. The significance of mafic nodules in the ultra-potassic rocks from central Italy - discussion. J. Volcanol. Geotherm. Res., 16(1–2): 161-165.

Villemant, B., Trigila, R. and DeVivo, B., 1993. Geochemistry of Vesuvius volcanics during 1631–1944 period. J. Volcanol. Geotherm. Res., 58(1–4): 291-313.

Webster, J.D., 2004. The exsolution of magmatic hydrosaline chloride liquids. Chem. Geol., 210(1–4): 33-48.

Webster, J.D., Goldoff, B., Sintoni, F. and De Vivo, B., 2012. Solubilities of H-O-C-S-Cl volatiles in fluids and silicate melts and their control on magmatic processes. Mineral. Mag., 76: 2532.

Webster, J.D., Goldoff, B., Sintoni, M.F., Shimizu, N. and De Vivo, B., C-O-H-S-Cl-F Volatile Solubilities, Partitioning, and Mixing Properties in Phonolitic-Trachytic Melts and Aqueous-Carbonic Vapor ± Saline Liquid at 200 MPa. Submitted to Journal of Petrology.

Webster, J.D., Raia, F., De Vivo, B. and Rolandi, G., 2001. The behavior of chlorine and sulfur during differentiation of the Mt. Somma-Vesuvius magmatic system. Mineral. Petrol., 73(1): 177-200.

Webster, J.D., Sintoni, M.F. and De Vivo, B., 2006. Chapter 11: The role of sulfur in promoting magmatic degassing and volcanic eruption at Mt. Somma-Vesuvius. In: B. De Vivo (Editor), Volcanism in the Campanian Plain: Vesuvius, Campi Flegrei and Ignimbrites. Development in Volcanology. Elsevier B. V., pp. 219-233.

Webster, J.D., Sintoni, M.F. and De Vivo, B., 2009. The partitioning behavior of Cl, S, and H_2O in aqueous vapor- ± saline-liquid saturated phonolitic and trachytic melts at 200 MPa. Chem. Geol., 263(1-4): 19-36.

Wood, B.J. and Trigila, R., 2001. Experimental determination of aluminous clinopyroxene-melt partition coefficients for potassic liquids, with application to the evolution of the Roman province potassic magmas. Chem. Geol., 172(3-4): 213-223.

Zajacz, Z., Halter, W.E., Malfait, W.J., Bachmann, O., Bodnar, R.J., Hirschmann, M.M., Mandeville, C.W., Morizet, Y., Muntener, O., Ulmer, P. and Webster, J.D., 2005. A composition-independent quantitative determination of the water content in silicate glasses and silicate melt inclusions by confocal Raman spectroscopy. Contrib. Mineral. Petrol., 150(6): 631-642.

Zambonini, F., 1910. Mineralogia Vesuviana. Atti R. Accad. Sci. Fis., Mat. Ser. 2°.

Tables

Table 1. – LA–ICPMS instrument and data acquisition parameters

Excimer 193–nm ArF laser GeoLasPro	
Output Energy	150 mJ
Energy Density on sample	~ 7 – 10 J/cm^2
Repetition Rate	5 Hz
Pit Size	Between 10 and 60 □m
Ablation Cell Volume	~ 1.5 cm^3
Cell Gas Flow (He)	~ 1 L/min
Agilent 7500ce quadrupole ICP–MS	
Auxiliary gas flow	1.03 l/min Ar
RF power	1500 V
Detector Mode	Dual 8 orders of magnitude linear dynamic range
Quadrupole Settling Time	2 ms
Data acquisition parameters	
Sweeps per reading	1
Reading per replicate	200 – 300
Replicates	1
Dwell time per isotope	10 ms
Points per peak	1 per measurement
External Standard	NIST610 glass
Isotopes Analyzed	^{23}Na, ^{25}Mg, ^{27}Al, ^{28} Si, ^{39}K, ^{40}Ca, ^{45}Sc, ^{49}Ti, ^{51}V, ^{52}Cr, ^{55}Mn, ^{56}Fe, ^{62}Ni, ^{85}Rb, ^{88}Sr, ^{89}Y, ^{90}Zr, ^{93}Nb, ^{138}Ba, ^{139}La, ^{140}Ce, ^{143}Nd, ^{147}Sm, ^{153}Eu, ^{172}Yb

Table 2. - Heating schedules used for experiments on clinopyroxene crystals from nodule NLM1-1a.

Temperature °C	Heating rate °C/min	Waiting time (min)	Sample
25-900	100	2	cpx01
900-1000	50	2	cpx02
1000-1100	25	2	cpx03
1100-1200	10	2	
from 1200	5		
			cpx05, cpx06
			cpx07, cpx08
25-1000	100	2	cpx101, cpx102
1000-1100	50	2	cpx104_area1, _area2
1100-1200	25	2	cpx105_area1, _area2
from 1200	10		cpx106, cpx107
			cpx108, cpx109
			cpx114
25-1000	100	2	cpx110, cpx113
1000-1100	50	2	cpx115, cpx116
1100-1200	25	2	cpx117, cpx118
1200-1220	10		cpx 119
from 1220	5		
25-1000	100	2	cpx121, cpx122
1000-1100	50	2	cpx123, cpx124
1100-1200	25	2	cpx125, cpx126
1200-1240	10		cpx127, cpx128
from 1240	5		cpx129, cpx130
			cpx133, cpx134
			cpx135_area1, cpx136
25-1000	100	2	cpx137, cpx138, cpx139
1000-1100	50	2	cpx140, cpx141, cpx143
1100-1170	25	1	cpx144, cpx145, cpx146
1170-1200	10	1	cpx147, cpx148, cpx149
1200-1240	5		cpx150, cpx151, cpx152
from 1240	2		cpx153, cpx154, cpx155
			cpx156, cpx157, cpx158
			cpx159, cpx160, cpx161
			cpx162, cpx164, cpx165

Table 3. - Representative LA-ICP-MS data of clinopyroxenes from the nodules.

	Type A			Type B	
Sample ID	**165_host**	**139_host1**	**151_host**	**NLM1-1d_cpx904**	**NLM1-1d_cpx905**
SiO_2	49.3	50.4	52.1	49.3	45.9
TiO_2	1.1	1.0	0.6	0.8	1.2
Al_2O_3	5.3	5.0	3.6	5.3	6.7
FeO	7.2	7.5	6.2	11.5	12.7
MnO	0.2	0.2	0.2	0.5	0.8
MgO	14.3	14.0	15.5	10.0	8.8
CaO	22.2	21.3	21.3	21.9	22.7
Na_2O	0.3	0.3	0.3	0.6	0.7
total	99.8	99.7	99.7	99.8	99.6
Sc	126	117	109	38	32
V	461	435	396	283	72
Cr	699	541	1203	-	-
Ni	81	94	93	25	14
Rb	-	-	-	-	2
Sr	92	89	84	314	87
Y	28	30	19	50	74
Zr	91	85	52	801	1737
Nb	0.4	0.4	-	5.3	45.7
Ba	0.4	0.3	0.2	0.8	5.0
La	8.7	8.4	5.4	44.7	141.9
Ce	31	31	21	133	380
Nd	31	31	21	90	126
Sm	9.5	10.0	5.8	20.9	24.5
Eu	2.0	2.1	1.2	4.4	5.8
Yb	2.2	2.9	1.4	5.3	11.5
mg#	0.85	0.77	0.82	0.62	0.69
En	41.7	41.8	45.2	30.7	27.0
Wo	46.5	45.7	44.7	48.5	49.9
Fs	11.7	12.6	10.1	20.8	23.2

mg#=Mg/(Mg+Fe2+), oxides in wt%, trace elements in ppm. "-" - below detection limit

Table 4. – Representative LA-ICP-MS data of amphibole from Type B nodule

Sample ID	NLM1-1d_amph3_host4	NLM1-1d_amph9_host4	NLM1-1d_amph906
SiO_2	42.9	42.8	42.8
TiO_2	1.0	0.9	1.6
Al_2O_3	12.3	12.8	12.4
MgO	16.4	16.1	15.8
CaO	12.0	12.0	11.7
MnO	0.2	0.2	0.2
FeO	8.1	8.4	8.5
Na_2O	2.1	2.1	1.8
K_2O	2.5	2.3	2.5
total	97.3	97.4	97.2
Sc	67	72	40
Ti	5916	5108	9760
V	188	163	292
Cr	237	33	0
Mn	1523	1365	1543
Ni	43	53	40
Rb	6.8	8.5	5.9
Sr	2320	2231	2448
Y	29	47	30
Zr	470	825	309
Nb	115	155	102
Ba	1777	1383	2856
La	43	57	33
Ce	111	134	104
Nd	58	73	62
Sm	10.8	15.8	14.5
Eu	3.2	3.7	4.3
Yb	2.5	4.9	2.7

Oxides are in wt%, trace elements are in ppm.

Table 5. - Representative LA-ICP-MS analyses of feldspar from the nodules.

	Type A			Type B	
Sample ID	**NLM1-1a_fp908**	**NLM1-1a_fp209**	**NLM1-1a_fp901**	**NLM1-1d_fp906**	**NLM1-1d_fp905**
SiO_2	57.3	49.6	62.7	61.7	61.2
Al_2O_3	23.2	32.6	21.6	21.2	20.8
CaO	1.0	13.5	0.7	0.6	0.9
Na_2O	3.0	3.0	3.6	0.5	0.5
K_2O	9.6	0.3	11.0	15.2	14.8
BaO	5.0	0.1	0.1	0.3	1.2
Total	99.1	99.0	99.6	99.6	99.3
Sc	31	28	44	29	22
Ti	1086	257	1073	103	195
V	1.8	2.0	0.7	-	-
Mn	1	31	-	-	13
Rb	137	2	152	83	72
Sr	3531	2314	665	1360	3549
Y	0.5	0.2	-	0.3	0.3
Zr	0.4	0.2	0.8	0.8	0.8
Nb	-	-	0.2	-	0.3
Ba	44695	849	556	3076	10568
La	8.0	5.0	5.2	8.0	9.4
Ce	3.9	7.6	3.9	7.3	6.4
Nd	0.5	2.3	0.5	1.4	-
Sm	0.3	0.3	-	0.3	-
Eu	9.5	0.8	2.5	3.1	4.9
Yb	-	-	-	-	-
Ab	30	28	32	4	4
An	6	70	3	3	5
Or	64	2	65	92	91

Oxides are in wt. %, trace elements are in ppm. "-" - below detection limit

Table 6. - Representative LA-ICP-MS data of mica from the nodules

	Type A			Type B
Sample ID	**NLM1-1a_mi901**	**NLM1-1a_mi905**	**NLM1-1b_mi906**	**NLM1-1d_mi901**
SiO_2	37.2	38.6	37.5	39.2
TiO_2	5.6	5.2	5.8	1.6
Al_2O_3	14.7	14.1	14.9	14.6
FeO	14.6	13.2	11.8	6.5
MnO	0.2	0.2	0.2	0.2
MgO	12.7	14.1	14.9	22.0
CaO	0.0	0.0	0.0	0.0
Na_2O	0.6	0.6	0.6	0.3
K_2O	10.3	10.0	10.2	10.2
BaO	0.01	0.01	0.03	1.42
total	95.9	95.9	95.8	95.9
Sc	20	24	26	17
Ti	33772	30882	34465	9464
V	211	159	378	114
Cr	0	0	9	4
Mn	1434	1236	1155	1380
Ni	94	117	170	70
Rb	373	355	399	189
Sr	19	16	34	630
Y	0.2	0.2	0.1	0.2
Zr	71	66	89	20
Nb	188	220	227	46
Ba	88	100	243	12742
La	0.1	0.1	0.1	1.1
Ce	0.3	0.1	0.3	0.1
Nd	-	-	-	-
Sm	-	-	-	-
Eu	0.1	0.1	0.2	1.8
Yb	0.1	0.1	0.1	-
mg#	0.61	0.66	0.69	0.86

Oxides are in wt%, trace elements are in ppm. mg#=$Mg/(Mg+Fe^{TOT})$
"-" – below detection limit

Table 7. - LA-ICP-MS data of the oxides from the nodules

	Type A		Type B	
Sample ID	**NLM1-1a_ox909_2**	**NLM1-1a_ox908_1**	**NLM1-1d_ox911**	**NLM1-1d_ox905_3**
SiO_2	0.10	0.13	0.32	0.11
TiO_2	22.71	26.82	4.05	5.93
Al_2O_3	3.55	3.33	5.91	3.02
Cr_2O_3	0.00	0.00	0.03	-
FeO	71.10	66.98	86.92	88.50
MnO	1.07	1.12	1.50	1.25
NiO	0.02	0.02	0.03	0.02
MgO	0.53	0.71	0.81	0.76
CaO	0.02	0.02	0.01	0.02
Total	99.10	99.13	99.58	99.61
Sc	-	-	-	-
V	4041	4280	1925	925
Cr	2	4	171	-
Mn	8269	8689	11616	9718
Ni	191	183	198	177
Rb	-	-	-	-
Sr	-	-	2.5	1.4
Y	0.3	-	0.3	3.1
Zr	799	498	2	64
Nb	335	228	8	87
Ba	0.4	-	2.8	2.5
La	-	0.2	0.9	5.4
Ce	0.3	0.1	0.9	10.4
Nd	-	-	-	3.9
Sm	-	-	-	0.5
Eu	-	-	-	-
Yb	0.2	-	-	0.5

Oxides are in wt%, trace elements are in ppm. "-" - below detection limit

Table 8. - Representative compositions of rehomogenized MI in clinopyroxene from NLM1-1a (Type A) nodule

Sample ID	NLM1-1a_cpx165_A	NLM1-1a_cpx151_D	NLM1-1a_cpx139_B
P_2O_5	0.638	0.725	0.738
SiO_2	50.432	53.98	52.824
TiO_2	1.279	0.927	1.446
Al_2O_3	11.491	15.661	14.665
MgO	7.964	5.236	5.573
CaO	13.556	8.034	9.012
MnO	0.156	0.076	0.092
FeO	7.715	5.377	7.517
Na_2O	1.812	2.269	2.518
K_2O	3.574	6.569	5.38
Total	98.675	98.854	99.765
Sc	-	-	-
V	338	342	307
Cr	128	547	200
Mn	1051	997	1018
Ni	-	-	-
Rb	122	62	145
Sr	368	289	364
Y	23	29	29
Zr	150	111	191
Nb	23	11	24
Ba	1163	660	1267
La	31.5	19.2	36.0
Ce	68.3	46.1	75.6
Nd	35.1	31.2	34.1
Sm	11.3	-	12.4
Eu	2.3	-	2.4
Yb	1.4	-	1.9
CO_2	856	220	
H_2O	0.07	0.04	
F		1364	
S	120	49	
Cl	1035	547	
T_q	1229	1224	1243
T_{calc}	1210.3	1157.6	1154.2
host mg#	0.84	0.82	0.77
calc host mg#	0.89	0.88	0.84

Oxides and H2O are in wt%, other volatiles and trace elements are in ppm. "-" below detection limit

Table 9. - Representative compositions of the inclusions in amphibole from nodule NLM1-1d (Type B)

Sample ID	**NLM1-1d_amph1_102**	**NLM1-1d_amph1_102**	**NLM1-1d_amph9_102**	**NLM1-1d_amph9_102**
x	3.782	0.279	3.71	0.472
Na_2O	1.9	0.6	2.1	2.6
MgO	16.3	28.5	14.3	6.8
Al_2O_3	13.0	18.0	13.0	18.0
SiO_2	42.9	41.6	45.2	48.8
K_2O	3.4	14.4	3.1	6.1
CaO	10.2	-	10.9	8.2
TiO_2	1.1	2.2	0.8	0.6
MnO	0.2	0.1	0.2	0.6
FeO	8.4	3.0	8.2	9.3
Sc	57	16	62	30
V	166	69	148	84
Cr	46	2	32	17
Mn	1279	759	1584	4477
Ni	39	78	32	22
Rb	32	303	15	71
Sr	2047	301	2064	1480
Y	31	-	46	95
Zr	406	-	941	3319
Nb	167	111	195	580
Ba	2354	18819	1798	2959
La	40	-	141	857
Ce	104	-	207	962
Nd	56	-	78	181
Sm	12.0	-	15.1	27.1
Eu	3.4	2.4	4.0	5.2
Yb	2.9	-	4.7	14.7

Oxides are in wt%, trace elements are in ppm. "-" - below detection limit

Publications

Klébesz, R., Bodnar, R., De Vivo, B., Török, K., Lima, A. and Petrosino, P., 2012. Composition and origin of nodules from the ≈20 ka Pomici di Base (PB)-Sarno eruption of Mt. Somma — Vesuvius, Italy. Central European Journal of Geosciences, 4(2): 324-337.

Esposito, R., Klebesz, R., Bartoli, O., Klyukin, Y., Moncada, D., Doherty, A. and Bodnar, R., 2012. Application of the Linkam TS1400XY heating stage to melt inclusion studies. Central European Journal of Geosciences, 4(2): 208-218.

Cent. Eur. J. Geosci.
DOI: 10.2478/s13533-011-0059-6

VERSITA

Central European Journal of **Geosciences**

Composition and origin of nodules from the ≈20 ka Pomici di Base (PB)-Sarno eruption of Mt. Somma – Vesuvius, Italy

Research Article

Rita Klébesz[1,2*], Robert J. Bodnar[1†], Benedetto De Vivo[2‡], Kálmán Török[3§], Annamaria Lima[2¶], Paola Petrosino[2]

1 *Dept. of Geosciences, Virginia Polytechnic Institute and State University, 4044 Derring Hall, Blacksburg, VA 24061, USA*

2 *Dept. of Earth Sciences, University of Naples "Federico II", Via Mezzocannone 8, Naples 80134, Italy*

3 *Eötvös Loránd Geophysical Institute of Hungary, Columbus u. 17.-23., Budapest 1145, Hungary*

Received 7 November 2011; accepted 6 February 2012

Abstract: Nodules (coarse-grain "plutonic" rocks) were collected from the ca. 20 ka Pomici di Base (PB)-Sarno eruption of Mt. Somma-Vesuvius, Italy. The nodules are classified as monzonite-monzogabbro based on their modal composition. The nodules have porphyrogranular texture, and consist of An-rich plagioclase, K-feldspar, clinopyroxene (ferroan-diopside), mica (phlogopite-biotite) ± olivine and amphibole. Aggregates of irregular intergrowths of mostly alkali feldspar and plagioclase, along with mica, Fe-Ti-oxides and clinopyroxene, in the nodules are interpreted as crystallized melt pockets.

Crystallized silicate melt inclusions (MI) are common in the nodules, especially in clinopyroxenes. Two types of MI have been identified. Type I consists of mica, Fe-Ti-oxides and/or dark green spinel, clinopyroxene, feldspar and a vapor bubble. Volatiles (CO_2, H_2O) could not be detected in the vapor bubbles by Raman spectroscopy. Type II inclusions are generally lighter in color and contain subhedral feldspar and/or glass and several opaque phases, most of which are confirmed to be oxide minerals by SEM analysis. Some of the opaque-appearing phases that are below the surface may be tiny vapor bubbles. The two types of MI have different chemical compositions. Type I MI are classified as phono-tephrite – tephri-phonolite – basaltic trachy-andesite, while Type II MI have basaltic composition. The petrography and MI geochemistry led us to conclude that the nodules represent samples of the crystal mush zone in the active plumbing system of Mt. Somma-Vesuvius that were entrained into the upwelling magma during the PB-Sarno eruption.

Keywords: Mt. Somma-Vesuvius • nodules • melt inclusions • crystal mush zone

*E-mail: krita@vt.edu
†E-mail: rjb@vt.edu
‡E-mail: bdevivo@unina.it
§E-mail: torokklm@elgi.hu
¶E-mail: anlima@unina.it
E-mail: petrosin@unina.it

1. Introduction

Nodules are foreign materials (xenoliths) found in erupted volcanic rocks. The term nodule usually refers specifically to coarse-grained "plutonic" xenoliths (e.g. [1–3]). In the Mt. Somma-Vesuvius literature, the term "nodules" has been used to describe a wide variety of rock types and textures. Hermes & Cornell [4] divided Mt. Somma-Vesuvius nodules into four groups: (1) biotite-bearing pyroxenite, wehrlite, and dunite "accumulative" rocks; (2) "skarns", represented by metasomatized carbonates; (3) recrystallized carbonate hornfels and (4) shallow plutonic rocks ("sub-effusive rocks"). Previous workers have studied these nodules extensively, especially the skarn and cumulate nodules from the younger Mt. Somma-Vesuvius eruptions [4–12]. Minerals in these nodules contain several different types of inclusions, including silicate melt, hydrosaline melt, and S-rich or CO_2-rich fluids. The nodules and their inclusions could provide tools for understanding magmatic processes associated with the Mt. Somma-Vesuvius system, including crystallization and mixing histories of magmas, as well as hydrothermal processes, including ore metal transport and deposition [10].

Nodules from the Pomici di Base (PB)-Sarno eruption at Mt. Somma-Vesuvius, which are the focus of this investigation, have not been previously studied to our knowledge. These nodules are found almost exclusively in the final products of the PB-Sarno eruption, which are comprised of lithic-rich fall deposits, surges and flows. In other eruptions of Mt. Somma-Vesuvius (e.g. Avellino and 79 AD eruptions), nodules are also found in the early ash and pumice airfall phase. Our goal in this study is to constrain the origin of the PB-Sarno nodules, and to determine what additional information they might provide concerning the underlying magmatic system prior to the PB-Sarno eruption. In this paper we present a detailed description of the nodules found in the final products of the PB-Sarno eruption, including their petrography and mineral chemistry and preliminary results of melt inclusion (MI) studies.

2. Geological setting

Mt. Somma-Vesuvius is located at the southern end of the Campanian Plain, near the city of Naples in southern Italy. The Mt. Somma-Vesuvius volcanic complex comprises the older, truncated edifice of Mt Somma, and Vesuvius, which forms a cone that developed within the older caldera by predominantly effusive activity (Fig. 1). Eruptive activity associated with the volcanic complex started after the huge Campanian Ignimbrite eruption (39 ka [13]), but other volcanic activity in the area which is not related to Mt. Somma-Vesuvius dates back to ca 400 ka [14, 15] (and references therein). According to Santacroce et al. [15] the PB eruption represents the first explosive event of the Somma volcano, dated at ca 22 ka. Other authors [16, 17] refer to this event as the Sarno eruption, and report that it follows an older explosive event, the Codola eruption. We use the term PB-Sarno eruption to recognize the fact that the two different names are commonly used in the literature to refer to the same eruptive event.

Eruptive activity at Mt. Somma-Vesuvius is cyclical, and three mega-cycles can be distinguished based on bulk rock compositional data [18] (and references therein). Within each mega-cycle the primary magma composition remains the same, but a new mega-cycle is characterized by a different composition [17]. The compositions of the eruptive products of the 3 mega-cycles change from slightly, to mildly, to highly silica-undersaturated [15, 18]. The products of the first mega-cycle are slightly silica-saturated (K-trachyte, K-latite) evolving toward slightly silica-undersaturated [17, 18]. The products of the second mega-cycle are mildly silica-undersaturated (phonotephrites to phonolites; [15, 17, 19]). The third mega-cycle is characterized by strongly silica-undersaturated rocks with tephrite to tephriphonolite-foidite composition [15, 19]. Each mega-cycle is made up of several shorter cycles, each starting with a plinian or sub-plinian eruption, followed by a strombolian-vulcanian "interplinian" stage. The first mega-cycle lasted from >25 ka to about 14 ka, the second from 8 ka to 2.7 ka. The third mega-cycle began after ≈800 years of repose with the 79 AD eruption that destroyed Pompeii. The last eruption at Mt. Somma-Vesuvius took place in 1944 and it is not clear if this represents the closing event of the third mega-cycle, or if it represents the beginning of a repose time within the shorter cycle that began in 1631. As noted by De Vivo et al. [18], the current repose time (68 years) is anomalous for the 1631-1944 interplinian cycle in which eruption cyclicity was between 7 and 30 years [18] (and references therein).

The PB-Sarno eruption occurred in three phases: (1) the opening phase consisting of ash and minor pumice fall, followed by: (2) a plinian phase comprising up to 6.5 m of compositionally zoned (trachyte to latite) fallout deposits with minor surge deposits; and (3) the closing phreatomagmatic phase characterized by lithic-rich fall, surge and flow deposits [20, 21]. According to Bertagnini et al. [20] this was the largest eruptive event in the history of Mt. Somma-Vesuvius on the basis of the thickness and areal distribution of the erupted material.

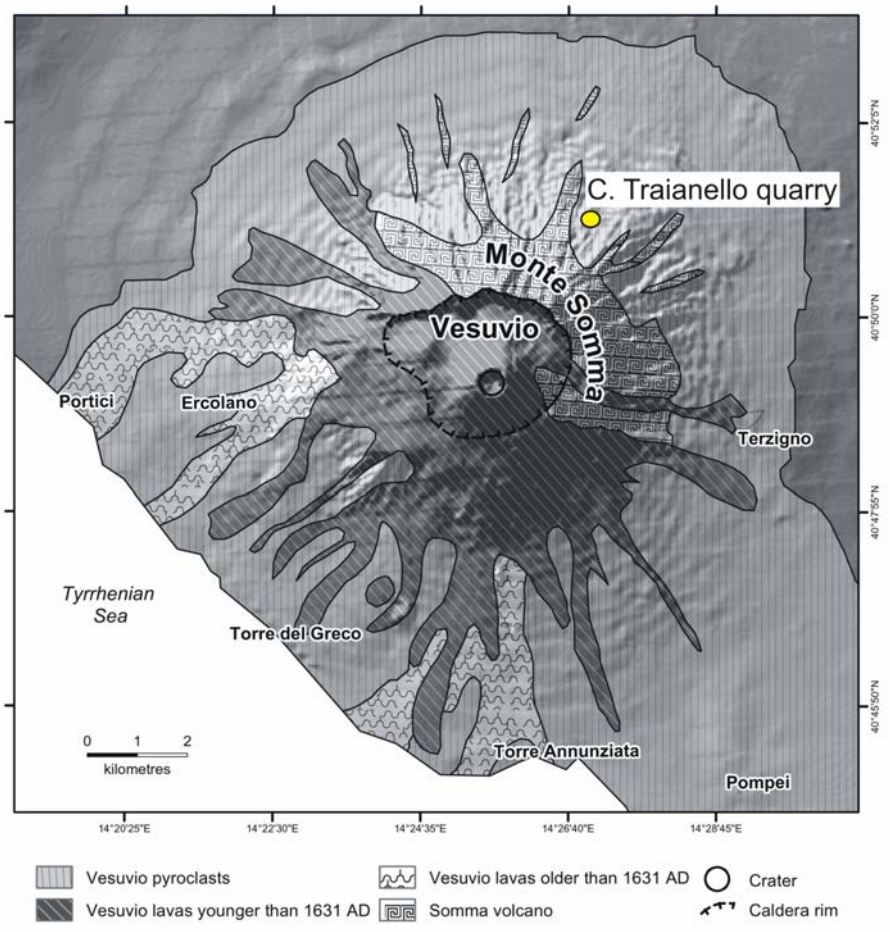

Figure 1. Map of Mt. Somma-Vesuvius – adapted from Peccerillo [40] – and the sample location within the C. Traianello quarry.

3. Samples and analytical methods

Samples were collected from the C. Traianello quarry, located on the NE slope of Mt. Somma (Fig. 1). All samples were collected from the topmost unit (about 1.5 m thick at the sample location) that consists of a pyroclastic flow deposit (Fig. 2). The studied nodules are coarse-grained (grain size up to 7 mm) igneous rocks with rounded to slightly angular equant to elongated shape. Nodule size varies from 1 to 5 cm. Nodules were divided into two sub-equal portions, and one portion was gently crushed by hand and clinopyroxene phenocrysts were handpicked under a binocular microscope. Single clinopyroxene crystals were polished on both sides, following procedures described by Thomas and Bodnar [22]. The other part of the nodule was used to prepare a doubly-polished thin section for analysis of phenocrysts by Cameca SX50 electron microprobe (EMPA) at Virginia Tech (Blacksburg, VA, USA). A beam current of 20 nA and an accelerating voltage of 15 kV were used during the analyses for olivine, clinopyroxene, amphibole and mica. A 5 µm defocused beam was used for feldspars, with analytical conditions similar to those described above for other minerals. The one sigma relative error is always less than 5%, and is usually under 1%, if the concentration of the element is >1 wt%.

Individual crystallized MI in single crystals extracted from the nodules during crushing were analyzed using an Excimer laser-ablation inductively-coupled plasma mass spectrometry (LA-ICPMS) system at Virginia Tech following the method described in Halter et al. [23]. Details of run conditions are reported in Table 1. The pit size was selected to be slightly larger than the inclusion diameter for each inclusion. The chemical composition of MI is quantified following the procedure described in Halter et al. [23], using the software package AMS [24]. The uncertainities are estimated to be 2-4% relative [25]. For

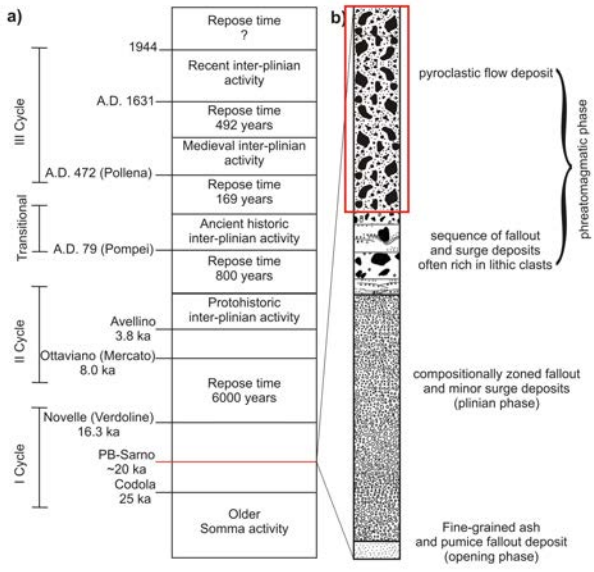

Figure 2. a) Stratigraphy of volcanic activity of Mt. Somma-Vesuvius, modified from Piochi et al. [25]. b) Schematic stratigraphic column of the PB-Sarno eruptive products, adapted from Bertagnini et al. [20]. The rectangular box near the top of the expanded column on the right indicates the portion of the unit that contains the nodules.

the internal standard, a value of Al_2O_3=18 wt% was used, because the aluminum content of the magma varies little (15.2 to 19.8 wt%) during the early history (megacycle I and earlier) of Mt. Somma [17, 19, 21].

4. Petrography

In this study we have recognized two types of nodules (Type A and B) based on their modal composition. All of the samples display a porphyrogranular texture (larger crystals in a finer-grained polycrystalline matrix) and are compositionally classified as monzonite-monzogabbro.

Type A nodules contain euhedral clinopyroxene and euhedral to subhedral olivine phenocrysts (Fig. 3**a-b**). The clinopyroxene phenocrysts show minor compositional zoning, and they contain olivine, apatite and Fe-Ti-oxide mineral inclusions, as well as MI. The rims of the crystals are irregular and show abundant embayments ("jagged" rims), suggesting that locally the clinopyroxenes were out of equilibrium with the melt. Mica ± clinopyroxene overgrowths are often observed around the olivine phenocrysts. The groundmass is completely crystallized, and consists of euhedral to subhedral (tabular) feldspar, clinopyroxene, mica, F-apatite and Fe-Ti-oxides. We also observed crystal aggregates comprised of irregular intergrowths of alkali feldspar and plagioclase, with lesser mica, Fe-Ti-oxides and clinopyroxene (Fig. 3**c**). The size of the aggregates ranges from about 100 μm up to a few mm. Crystals in the aggregates are much smaller than those in the groundmass. Based on the petrographic characteristics described above, we interpreted the aggregates to represent crystallized melt pockets.

Table 1. LA-ICPMS instrument and data acquisition parameters.

Excimer 193-nm ArF laser GeoLasPro	
Output Energy	150 mJ
Energy Density on sample	~7 – 10 J/cm^2
Repetition Rate	5 Hz
Pit Size	Between 16 and 60 mm
Ablation Cell Volume	~1.5 cm^3
Cell Gas Flow (He)	~1 L/min
Agilent 7500ce quadrupole ICP-MS	
Auxiliary gas flow	1.03 l/min Ar
RF power	1500 V
Detector Mode	Dual 8 orders of magnitude linear dynamic range
Quadrupole Settling Time	2 ms
Data acquisition parameters	
Sweeps per reading	1
Reading per replicate	200 – 300
Replicates	1
Dwell time per isotope	10 ms
Points per peak	1 per measurement
External Standard	NIST610 glass
Isotopes Analyzed	^{23}Na, ^{25}Mg, ^{27}Al, ^{28}Si, ^{39}K, ^{40}Ca, ^{45}Sc, ^{49}Ti, ^{51}V, ^{52}Cr, ^{55}Mn, ^{56}Fe, ^{62}Ni, ^{85}Rb, ^{88}Sr, ^{89}Y, ^{90}Zr, ^{93}Nb, ^{138}Ba, ^{139}La, ^{140}Ce, ^{143}Nd, ^{147}Sm, ^{153}Eu, ^{172}Yb

The dominant phenocryst in Type B nodules is sub- to anhedral amphibole (Fig. 3**d-e**). A reaction rim, consisting of mica, clinopyroxene and feldspar, is sometimes observed around the amphiboles. The edges of the amphibole phenocrysts are more irregular compared to the clinopyroxene phenocrysts in type A nodules. The groundmass consists of clinopyroxene, K-feldspar, Fe-Ti oxide, F-apatite and an unidentified Ca-K-silicate phase. Crystal aggregates are also observed and consist of irregular intergrowths of K-feldspar and the same unidentified Ca-K-phase as in the groundmass, with abundant mica and Fe-Ti-oxides. The crystal aggregates range up to a few hundred microns. The aggregates and the groundmass show similar textures, except that the aggregates are finer grained. Based on the petrographic characteristics we interpret the aggregates to represent crystallized melt pockets, similar to those in Type A nodules.

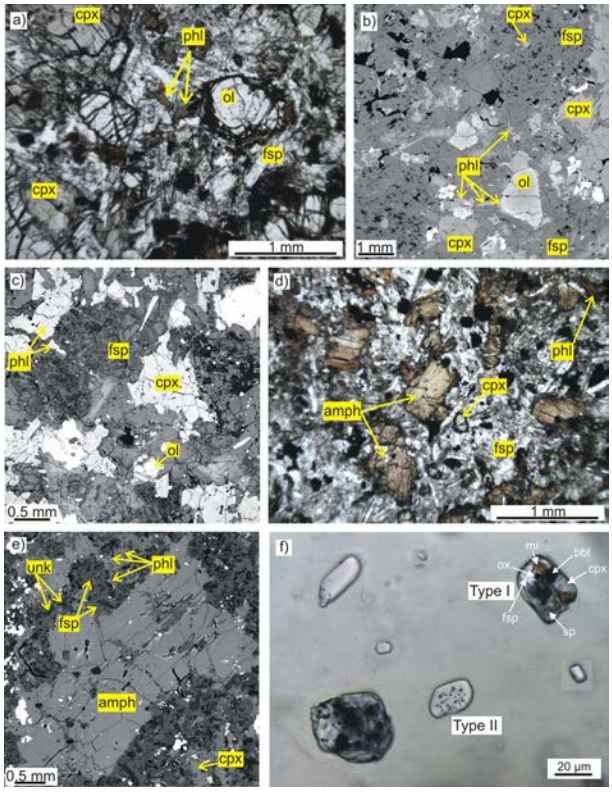

Figure 3. Photomicrographs showing mineral textures and melt inclusions in the nodules. a) Photomicrograph (in plane polarized light) of Type A nodule showing a porphyrogranular texture with clinopyroxene (cpx) and olivine (ol) phenocrysts. The matrix consists of feldspar (fsp), phlogopite (phl), apatite and Fe-Ti-oxides. b) Scanning electron microscope back-scattered (BSE) image of Type A nodule. Aggregates of cpx, phl and irregular intergrowths of alkali feldspar and plagioclase can be observed. c) BSE image of Type A nodule at higher contrast and higher magnification compared to image "b". The irregular intergrowth of feldspars in the groundmass is highlighted (lighter areas are alkali feldspar, and darker areas are plagioclase). d) Photomicrograph (in plane polarized light) of Type B nodule showing a porphyrogranular texture with amphibole (amph) phenocrysts. The matrix consists of cpx, phl, fsp, apatite and Fe-Ti-oxides. e) BSE image of Type B nodules. Note the irregular intergrowth of phl, fsp and an unknown phase (unk) adjacent to the amph phenocryst. f) Photomicrograph of Type I and Type II melt inclusions in cpx from Type A nodule. Type I consists of mica (mi), Fe-Ti-oxides (ox) and/or dark green spinel (sp), clinopyroxene (cpx), feldspar (fsp) and a vapor bubble (bbl). Type II Inclusions are generally lighter in color and they contain feldspar and/or glass and several dark phases that are possibly oxide minerals and/or tiny vapor bubbles.

5. Mineral chemistry

Compositions of representative mineral phases in the nodules are listed in Table 2. Clinopyroxene is present as phenocrysts and in the groundmass in Type A nodules, while it only appears in the groundmass in Type B nodules. Clinopyroxenes have diopside-ferroan diopside compositions ($En_{49-33}Wo_{46-47}Fs_{5-20}$) in Type A nodules, and a ferroan diopside composition ($En_{39-24}Wo_{48-49}Fs_{13-27}$) in Type B nodules (Fig. 4**a**). The mg# ($Mg/(Mg+Fe^{tot})$) ranges from 0.92 to 0.63 in Type A nodules, and from 0.79 to 0.49 in Type B nodules. The clinopyroxenes generally show normal zoning, but rarely show reverse zoning. The composition of the clinopyroxene in the groundmass is similar to the composition of the rims of clinopyroxene phenocrysts, suggesting that the groundmass clinopyroxenes crystallized as a result of rapid cooling of the same melt that was crystallizing at the rims of clinopyroxene phenocrysts.

Olivine phenocrysts were only observed in Type A nodules. The Fo content of olivine ($Mg^*100/(Mg+Fe)$) ranges from 76 to 54. The olivines have uniformly low NiO (<0.16 wt%) and relatively high CaO content (up to 0.36 wt%).

Micas in both nodule types are fluorine-rich phlogopites, but the composition in Type A nodules has a wider range (Fig 4**b**). The mg# ($Mg/(Mg+Fe^{tot})$) ranges from 0.88 to 0.59 and from 0.90 to 0.86, in Type A and B nodules, respectively. The F content ranges from 6.5 wt% to 2.3 wt% in Type A, and from 8.3 wt% to 7.2 wt% in Type B nodules.

Feldspar is the main component of the groundmass. K-feldspar and plagioclase are equally abundant in type A nodules, but K-feldspar is much more abundant than plagioclase in type B nodules. Intergrowth feldspars in Type A nodules are enriched in K and Na compared to the tabular feldspars in the same nodule (Fig. 4**c**). Many tabular K-feldspars have a Ba-rich core (up to 6 wt%), with Ba content decreasing gradually towards the rim to, in some cases, below detection limit.

Magnesio-hastingsite amphiboles with small variations in FeO (7.3-9.7 wt%), MgO (15.6-17.4 wt%) and F content (3.6-4.8 wt%) occur as phenocrysts in Type B nodules. Accessory apatite in both types of nodules is extremely F-rich (up to 6 wt%).

Landi et al. [21] described both polycrystalline and plagioclase-only aggregates in the pumice and scoria that were deposited during the plinian phase of the PB-Sarno eruption. They interpreted the aggregates to represent fragments of the crystal mush zone at the upper margins of the magma chamber that were entrained into the erupting material. The compositions of plagioclase and sanidine in the aggregates described by Landi et al. [21] are similar to those in our samples (Fig. 4**c**). They also report clinopyroxene, but with a more evolved composition (Fs_{20-24}) compared to that found in this study, and potassium-ferripargasite amphibole, which is also different from the magnesio-hastingsite amphibole in our samples.

Table 2. Representative microprobe analyses of the mineral phases in Type A and B nodules from the Sarno eruption (gm - groundmass, agg. - irregular intergrowth of feldspar in the aggregates, mg#=Mg/(Mg+Fe), b.d. -below detection).

Sample	Clinopyroxene								
	Type A							Type B	
	core	rim	core	zone	rim	gm	gm	gm	gm
SiO_2	54.60	51.16	51.46	51.98	51.26	50.69	49.10	50.64	50.91
TiO_2	0.22	1.01	0.98	0.82	1.16	1.50	1.43	0.73	0.67
Al_2O_3	1.93	4.09	4.06	4.00	3.29	3.73	6.50	4.60	3.33
FeO	2.88	7.99	7.52	6.54	8.57	9.18	7.76	8.07	10.64
MnO	0.05	0.16	0.16	0.13	0.13	0.17	0.23	0.21	0.45
MgO	17.88	14.28	14.48	14.77	13.84	13.13	13.25	13.02	11.27
CaO	22.95	22.02	22.02	22.83	22.32	22.34	22.42	23.05	22.75
Na_2O	0.19	0.36	0.36	0.27	0.34	0.38	0.34	0.38	0.49
Total	100.69	101.06	101.03	101.34	100.91	101.12	101.02	100.70	100.51
En	50	41	42	42	40	38	39	38	33
Wo	46	46	46	47	46	47	48	48	48
Fs	5	13	12	11	14	15	13	14	18

Sample	Amphibole			
	Type B			
		core	rim	
SiO_2	43.10	43.29	42.90	
TiO_2	0.85	1.21	1.08	
Al_2O_3	11.77	11.85	11.75	
FeO	8.64	7.31	9.71	
MnO	0.15	0.16	0.31	
MgO	16.95	17.15	15.57	
CaO	12.71	12.84	12.33	
Na_2O	1.92	1.81	0.93	
K_2O	2.06	2.50	4.02	
F	4.64	4.43	3.59	
Cl	0.10	0.10	0.10	
total	102.89	102.64	102.28	

Sample	Mica		
	Type A		Type B
SiO_2	38.20	39.90	40.92
TiO_2	4.88	6.80	1.94
Al_2O_3	13.72	12.97	13.33
FeO	16.43	8.39	5.71
MnO	0.16	0.07	0.22
MgO	13.50	18.26	22.75
CaO	0.03	0.16	0.01
Na_2O	0.65	0.54	0.11
K_2O	9.45	9.53	9.94
F	3.00	4.25	7.70
Cl	0.11	0.07	0.04
total	100.14	100.95	102.67
mg#	0.59	0.80	0.88

Sample	Feldspar						
	TypeA						Type B
	core	rim			agg.	agg.	
SiO_2	62.10	65.55	64.95	48.42	63.51	61.79	65.17
Al_2O_3	19.90	19.13	19.83	32.35	23.12	22.81	19.38
CaO	0.90	0.75	1.06	16.69	5.05	0.61	0.78
Na_2O	3.45	3.56	4.10	2.00	8.17	0.42	0.38
K_2O	9.83	11.09	10.31	0.09	0.52	15.60	15.99
BaO	3.73	0.14	0.03	0.05	0.04	0.03	0.18
Total	99.90	100.22	100.29	99.60	100.40	101.25	101.87
Ab	33	32	36	13	72	4	3
An	5	4	5	87	25	3	4
Or	62	65	59	0	3	93	93

Sample	Olivine		
	Type A		
SiO_2	38.27	35.24	
FeO	24.23	33.44	
MnO	0.34	0.87	
NiO	0.03	b.d.	
MgO	37.14	29.82	
CaO	0.35	0.26	
Total	100.36	99.64	
Fo	73	61	

Sample	Apatite	
	Type A	Type B
P_2O_5	38.79	39.67
SiO_2	0.33	1.03
CaO	54.70	54.03
FeO	0.43	0.28
F	6.48	6.23
Cl	0.32	0.08
Total	101.05	101.32

Sample	Unknown phase	
	Type B	
SiO_2	37.39	37.55
TiO_2	b.d.	b.d.
Al_2O_3	28.96	29.68
Cr_2O_3	b.d.	b.d.
MgO	b.d.	b.d.
CaO	13.58	14.62
MnO	0.02	0.04
FeO	b.d.	b.d.
Na_2O	0.97	1.33
K_2O	4.20	4.61
F	0.36	b.d.
Cl	0.04	b.d.
Total	85.53	88.10

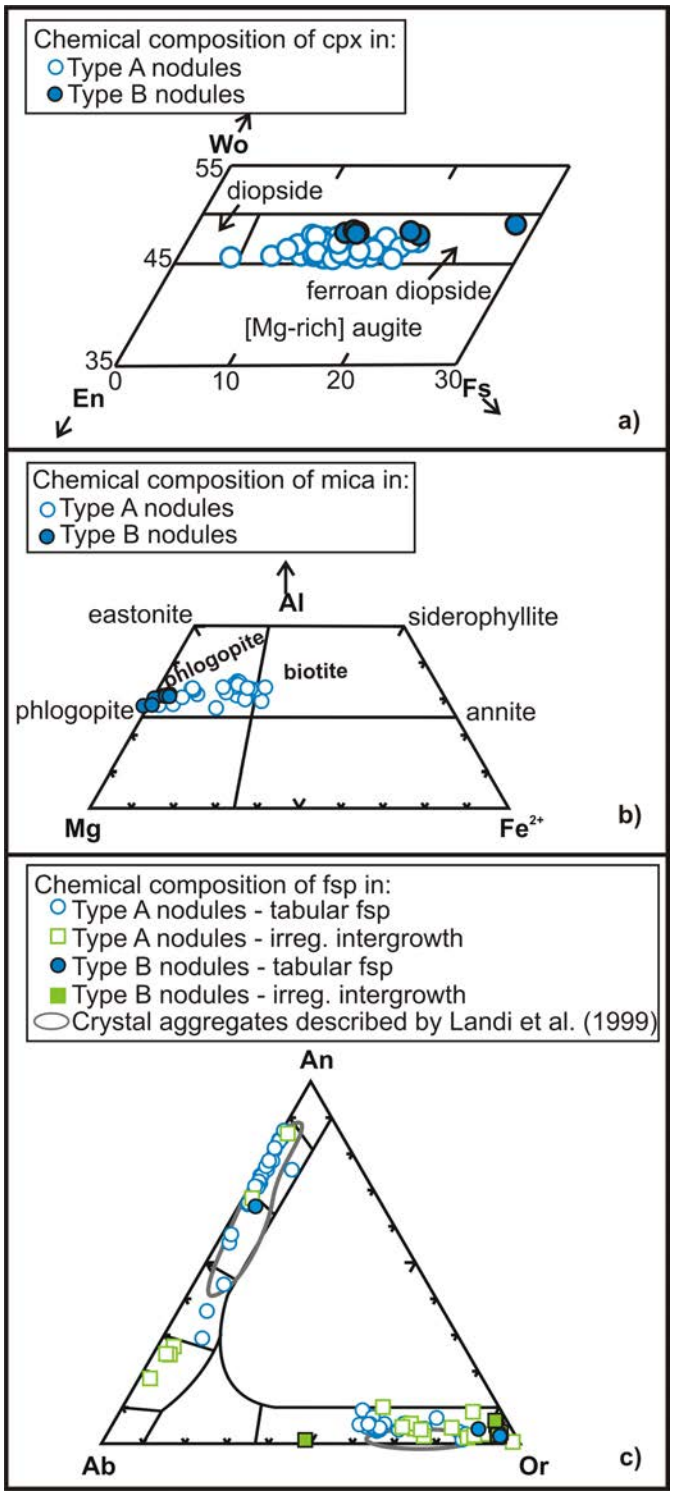

Figure 4. Chemical composition of minerals in Type A and B nodules: a) clinopyroxene (cpx), b) mica, and c) feldspar (fsp) compositions. For comparison, compositions of feldspars in crystal aggregates reported by Landi et al. [21] have been plotted.

Table 3. Representative LA-ICP-MS analysis of crystallized silicate-melt inclusions in clinopyroxene host from Type A nodule.

Sample	Type I					Trans.	Type II		
(wt%)									
SiO_2	52.35	48.89	52.97	56.01	52.09	49.44	48.53	52.34	45.03
TiO_2	1.19	1.75	1.31	1.18	1.63	1.00	0.90	0.40	0.63
Al_2O_3	17.83	18.01	18.01	18.01	18.00	17.92	18.00	18.01	18.00
FeO	6.81	8.03	6.30	5.75	6.71	6.09	2.48	2.82	2.16
MnO	0.14	0.12	0.13	0.08	0.11	0.11	0.11	0.08	0.11
MgO	4.78	4.58	4.00	3.28	4.18	7.24	8.23	7.79	9.84
CaO	7.60	8.11	7.26	4.12	8.30	13.21	19.55	16.19	21.89
Na_2O	2.73	1.24	3.09	3.08	2.52	1.37	1.40	1.04	1.31
K_2O	6.18	8.56	6.54	7.85	5.86	3.24	0.58	0.75	0.68
Total	99.61	99.29	99.61	99.36	99.40	99.62	99.78	99.42	99.65
(ppm)									
Ni	50	59	52	51	64	65	84	136	21
Cr	< 0.156	267	<0.108	768	447	146	<0.314	2265	616
V	251	206	242	106	294	320	253	201	183
Sc	35	32	23	27	50	54	66	75	89
Rb	215	272	239	306	201	111	4	17	10
Ba	2237	3541	2350	2847	2589	1294	562	476	552
Nb	33	48	41	45	42	14	1	3	1
Sr	682	918	604	658	591	771	1008	979	1051
Zr	202	261	244	207	247	113	59	55	49
Y	26	33	27	15	29	20	17	11	14
La	51	76	57	50	56	29	9	8	9
Ce	100	152	117	89	110	62	29	25	24
Nd	46	66	52	36	53	35	17	17	16
Sm	8.8	15.3	9.8	7.2	12.7	4.1	1.5	3.1	7.4
Eu	2.5	2.7	2.4	1.3	2.4	2.6	2.3	0.7	1.4
Yb	2.5	2.3	2.7	<0.06	3.2	1.7	1.6	0.5	2.1
MF	0.29	0.20	0.37	0.24	0.31	0.36	0.27	0.23	0.21
host composition	$En_{43}Wo_{46}$	$En_{41}Wo_{45}$	$En_{42}Wo_{45}$	$En_{41}Wo_{45}$	$En_{43}Wo_{45}$	$En_{43}Wo_{45}$	$En_{41}Wo_{44}$	$En_{42}Wo_{45}$	$En_{43}Wo_{44}$

MF - mass factor (mass of inclusion/total mass ablated); Trans. - Transitional type MI

6. Melt inclusions

MI are abundant in clinopyroxenes in Type A nodules. All MI examined are partially to completely crystallized, which is typical of MI that cooled relatively slowly after trapping [26, 27]. The MI are mostly 20–30 µm in maximum dimension, but range from about 5 to 60 µm, and have rounded to angular shape.

MI are grouped into two types based on petrography (Fig. 3**f**). Type I consists of mica, Fe-Ti-oxide minerals and/or dark green spinel, clinopyroxene, feldspar and a vapor bubble. No volatiles (CO_2, H_2O) were detected in the bubbles by Raman spectroscopy [28]. Type II inclusions are generally lighter in color when observed in transmitted light and contain subhedral feldspar and/or glass and several black (opaque?) phases, most of which are confirmed to be oxides by SEM analysis. Some of the opaque-appearing phases that are below the surface may be tiny vapor bubbles. The MI are either randomly distributed in the crystals or occur along a growth zone and are, therefore, interpreted to be primary. The two types of MI are spatially associated, appearing in the same area within the crystals. Type I MI comprises 70 to 80% of total melt inclusions observed. Moreover, some MI appear to be transitional between Types I and II in both their petrographic features and compositions. Only MI in clinopyroxenes from Type A nodules were analyzed.

Abundant data are available in the literature for comparison with our MI data. These include:

1. bulk rock compositions of pumices erupted during the plinian phase of the PB-Sarno eruption [17, 21]

2. bulk compositions of lavas erupted between 35-25 ka [17, 19]

3. bulk rock compositions of lava and scoria erupted after 25 ka but before the PB-Sarno eruption [19]

4. compositions of MI in clinopyroxene from lavas erupted between 35-25 ka, as well as compositions of MI from lavas that are younger than 25 ka but older than the PB-Sarno eruption [29]

The various types of data listed above have been plotted along with our MI data on various chemical discrimination diagrams, including total alkali-SiO_2 classification diagram (Fig. 5**a**; [30]), primitive mantle normalized [31] trace element diagrams (Fig. 5**b-d**), and major element variation diagrams (Fig. 5**e-g**). Because the Codola eruption (~25 ka) cannot be related to a specific Campanian source (i.e., Mt. Somma-Vesuvius, Campi Flegrei, or elsewhere in the Campanian region) [15, 16], it is not included in the comparison on Figure 5.

Our results indicate that Type I MI can be classified as phono-tephrite – tephri-phonolite – basaltic trachyandesite (Fig. 5**a**), and are similar to compositions of other MI from related eruptions [29]. The compositions of Type I MI from this study overlap with the compositions of the older Somma lavas (<35 ka but older than the PB-Sarno eruption) and show trends on major element variation diagrams that are similar to trends for MI from the literature [29] (Fig. 5**e-g**). The PB-Sarno pumices have a more evolved composition compared to the MI compositions of this study. However, trace element patterns for the Type I MI are similar to the older Somma lavas and the PB-Sarno pumices when plotted on primitive mantle normalized [31] trace element diagrams (Fig. 5**b-d**). Furthermore, the MI show enrichment in LILE (Rb, Ba, Th, K) and, to a lesser extent, HFSE (Nb, Zr) with respect to the primitive mantle.

Type II MI are mainly basaltic in composition, and show more primitive compositions with lower silica, alkalies and higher Ca and Mg content compared to published MI and bulk rock compositions (Fig. 5**a, e-f**). Type II MI show less enrichment in LILE and HFSE with respect to the primitive mantle, compared to Type I MI (Fig. 5**b**). Some MI could be classified as either type I or type II, based on petrography alone. These transitional MI appear to also show intermediate compositions (squares in Fig. 5).

Equilibrium between the MI and host was tested based on the Fe-Mg exchange reaction between clinopyroxene and host. Using the models in Putirka [32] that are based on the Fe and Mg content of the melt and crystal, equilibration temperatures range from 1058 to 1264°C and pressures ranging from 3.9 to 10.6 kbar. Entering these temperatures into equation (35) of Putirka [32] predicts $K_D(Fe\text{-}Mg)^{cpx-liq}$ ranging from 0.25-0.29 over this range of temperatures, assuming that the melt and crystal are in equilibrium. However, the $K_D(Fe\text{-}Mg)^{cpx-liq}$ predicted from [32] for Type I MI ranges mostly from 0.3 to 0.45 (with a few values up to 0.6). This suggests that Type I MI were not in complete equilibrium with the host. The $K_D(Fe\text{-}Mg)^{cpx-liq}$ predicted for Type II MI are all >1, indicating that these MI compositions are far from equilibrium with the host.

Trends in MgO vs. CaO/Al_2O_3 (Fig. 5**h**) for MI in this study are similar to trends defined by previously published MI data [29], and are consistent with melt compositions that would be produced during clinopyroxene fractionation from a crystallizing melt.

7. Discussion

The studied nodules were collected from the upper part of the PB-Sarno eruption deposits. As such, the nodules could have formed earlier from the same magma that produced the PB-Sarno eruption. Alternatively, the nodules might represent samples of older Somma volcanic activity (39-22 ka) that were ripped from the conduit walls and entrained into the PB-Sarno magmas as they ascended. Cioni et al. [33] found clear evidence of a caldera collapse associated with the PB-Sarno eruption, and Rolandi et al. [34] suggested that the PB-Sarno eruption was one of four eruptive events that contributed to the destruction of the older Somma cone. Therefore, it is likely that materials from the conduit walls and from older eruptive units have collapsed into the erupting PB-Sarno magma and were carried to the surface during the eruption.

Similarities between Type A and B nodules, including the presence of melt pockets, jagged (irregular) edges and slight zoning of the phenocrysts and the absence of typical equilibrium textures (e.g. planar boundaries, 120° jointing, absence of zoning) indicate that the two different nodule types formed in similar environments and experienced similar pre-eruptive histories. The textural features described above are common in the "sub-effusive" type of nodule described by Hermes & Cornell [4]. They interpret these nodules to have formed at a shallower level compared to the "accumulative" nodule type. These workers state additionally that the compositions of sub-effusive nodules and compositions of extruded lavas are similar. They suggest that the "sub-effusive" type of nodule represents samples of the crystal mush zone in which the

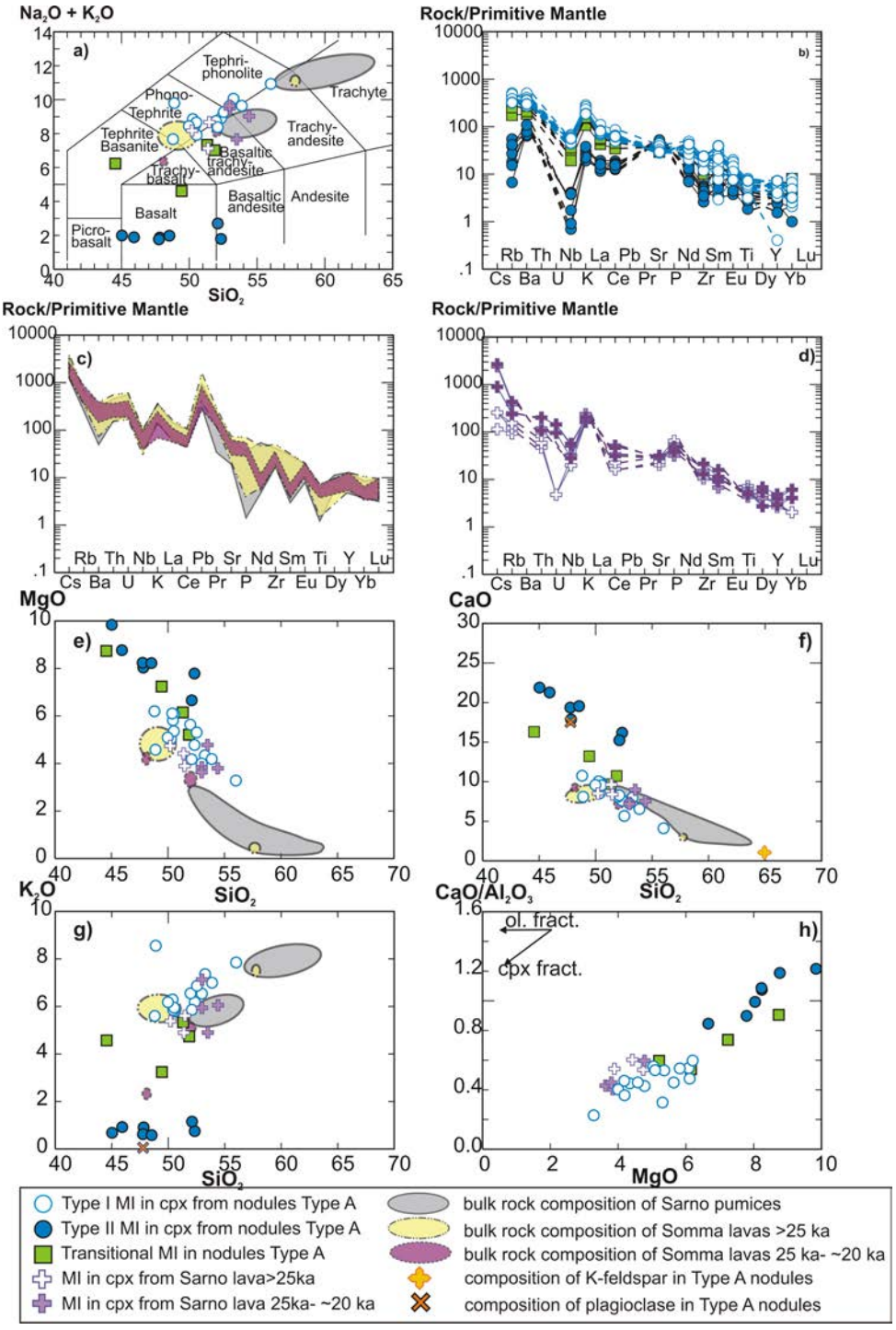

Figure 5. Compositions of host rocks, minerals and melt inclusions associated with PB-Sarno nodules. Compositions of crystallized MI were determined by LA-ICP-MS analysis. a) Total alkali – silica diagram [30] showing MI and published bulk rock compositions of associated Somma lavas and pumices, b-d) Primitive mantle-normalized [31] trace element diagram, e) SiO_2 versus MgO, f) SiO_2 versus CaO, g) SiO_2 versus K_2O, h) MgO versus CaO/Al_2O_3. The arrows on Fig. 3f labeled "cpx fract" and "ol. fract" show the compositional trends in residual melt which would result from clinopyroxene and olivine crystallization, respectively. For comparison, the bulk composition of the pumices erupted during the plinian phase of the PB-Sarno eruption [17, 21], the bulkcompositions of lavas erupted between 35-25 ka [17, 19], of lava and scoria erupted after 25 ka but before the PB-Sarno eruption [19], and compositions of melt inclusions hosted in clinopyroxene from lava erupted between 35 ka and the PB-Sarno eruption [29] are also plotted.

crystal/melt ratio was high. This material was extracted from the crystal mush zone and then transported upwards *"slowly and intact, permitting crystallization of the interstitial liquid"* [4]. Alternatively, Hermes and Cornell [4] also suggest that the type of nodule described here could represent cumulitic xenocrysts that were extracted from the mush-zones and then mixed with magmas of different compositions within a chemically zoned magma chamber. The rare reverse zoning observed in clinopyroxene and the relatively low-Fo olivine (Fo≤76 mol%) inclusions in primitive clinopyroxene (mg#≥0.80) indicate that some mixing occurred. However, the lack of typical non-equilibrium textures (e.g. multiple resorption surfaces within a crystal; complex zoning; reaction rims) suggests that the samples more likely represent a crystal mush zone where the crystal/melt ratio was high, rather than mixing with magmas of different composition. The differences between Type A and B nodules suggest that, even though they formed in a similar environment (probably a crystal mush zone at the margins of a magma chamber), they are derived from different regions of a compositionally zoned magmatic system.

The compositions of the crystals in the studied samples are more primitive compared to the crystal aggregates described by Landi et al. [21], which they found in pumices and scorias deposited during the sustained column phase of the eruption ("plinian phase" in [20, 21]). This compositional difference suggests that the nodules in the present study were derived either from a region of the magma chamber that was not sampled during the plinian phase of the eruption, e.g. from the more crystal-rich part that is closer to the margin, or from a different depth in a layered magma chamber. The latter interpretation is consistent with results of Landi et al. [21], who suggest that the magma chamber associated with the PB-Sarno eruption was compositionally layered. As such, the studied nodules were likely entrained as the magma passed through a portion of the magma chamber with a more primitive composition as it ascended to the surface. Various thermobarometers were applied to the mineral assemblages contained in the nodules in an effort to constrain the pressure and temperature of crystallization. The models in Putirka [32] predict temperatures ranging from 1058 to 1264°C and pressures ranging from 3.9 to 10.6 kbar. Additional MI studies, including analysis of MI in Type B nodules as well as analysis of volatiles in MI from both Type A and B nodules, may help to better constrain the PT conditions.

Two very distinctive types of MI were observed in clinopyroxenes from Type A nodules. The two types of MI are spatially associated, which would suggest a genetic relationship, but the nature of this relationship is unclear. The trace element compositions and the close spatial association of these MI with different compositions indicate that the melts are not differentiated from the same parent melt. Type I MI are in or close to chemical equilibrium with the host and are interpreted to represent the melt from which the surrounding host clinopyroxene crystallized. Type II MI occur in close association with Type I MI, but Type II are not in chemical equilibrium with the host. This suggests that the composition of Type II MI was either modified by accidentally trapped solid phases or that the MI composition reflects heterogeneities within the melt. The high Ca- and low K-contents of Type II MI suggest that trapping and/or dissolution of An-rich plagioclase, which is observed in MI and as solid inclusions in clinopyroxene, might have played a major role in altering the composition of the Type II MI. This process, however, does not explain the high Mg-content of the Type II MI. Mesozoic carbonates with a thickness of ~8 km that dip westward from the adjacent Apenninic belt have been detected at a depth of 2–3 km in the Mt. Somma-Vesuvius area [35–37]. Both the high Ca- and Mg contents of Type II MI can be explained by assimilation of dolomite at depth, either by trapping small dolomite crystals in the MI or incorporating dolomite into the parental magma before MI trapping, but stable isotopic data are required to confirm this hypothesis.

Previous studies have reported anomalous MI (e.g. high-Ca inclusions in Fo-rich olivine) occurring together with "normal" MI (i.e. in equilibrium with the host) in the same sample from various mid-ocean ridge and subduction environments [38] (and references therein). Danyushevsky et al. [38] attributed the origin of these anomalous MI to "dissolution-reaction-mixing (DRM) processes". In a complex magmatic plumbing system consisting of interconnected chambers, each with a well-developed mush zone, the intruding magma batches can react with the much cooler wall-rock and/or material in the semi-solidified crystal-mush zones. In addition to cooling of the intruded magma in the mush zones, phases which are not in equilibrium with the intruded melt may undergo partial dissolution. This may be followed by mixing of the reaction products with the intruded melt to produce hybrid melts that can be trapped as MI. These processes can lead to large localized melt heterogeneities which are then sampled by the crystallizing phases [38]. Danyushevsky et al. [38] emphasize that these anomalous and commonly large inclusions are formed at the edges of the conduit system, where the fresh, hot magma is in contact with the cooler mush-zone. In the center of the magma chamber or conduit, olivine (and other phases) would crystallize in equilibrium with the surrounding melt, and these phenocrysts would not contain anomalous MI.

We suggest a model similar to that of Danyushevsky et al. [38] for the origin of Type II MI in the PB-Sarno nodules. It is well documented that Mt. Somma-Vesuvius has a complex plumbing system consisting of three main levels of magma storage, the two deepest of which represent long-lived reservoirs [39] (and references therein). This geometry provides the opportunity for the formation of extensive mush zones over an extended depth range and P-T conditions [11, 12, 39]. Subsequent interaction of material in these mush zones with the differentiating or upwelling melt and/or the wall rock can occur. The process described by Danyushevsky et al. [38] is consistent with our hypothesis that the Type A nodules represent samples of a crystal-mush zone that was once in contact with the magmas that formed the bulk of the erupted material. However, we are unable to determine the specific location within the overall plumbing system of the mush zone that was sampled, and when in the overall evolution of the system that sampling occurred. The major element composition of the MI overlaps with the composition of the older Somma lavas and their MI, which suggests that the Type A nodules more likely were formed prior to the PB-Sarno plinian eruption. However, because data for the composition of PB-Sarno pumice parental magma is not available, we are unable at this time to test our hypothesis that the nodules formed before the PB-Sarno eruption.

8. Conclusions

Petrographic features, including the porphyrogranular texture, slight zonation of the phenocrysts, crystallized melt pockets, and "jagged" edges of crystals, all suggest that nodules collected from the PB-Sarno eruption represent samples of the mush zone of the active plumbing system of Mt. Somma-Vesuvius. Geochemically different but spatially associated MI, and similarities between type A MI and the BP-Sarno bulk rock composition and the composition of older eruptive material, support this hypothesis. The nodules could have crystallized either from the same magma that was erupted during the earlier plinian phase of the PB-Sarno eruption, or from a magma associated with an older eruptive phase. Data obtained from Type I MI may provide valuable information about inferred heterogeneities (layering within the magma chamber) during the early history of the volcano. Further studies are in progress to homogenize the crystallized MI and determine the major and trace element compositions as well as the volatile content of the melts. These data will help to better constrain the structure of the plumbing system and pre-eruptive processes that formed the nodules and led to the BP-Sarno eruption.

Acknowledgements

The authors would like to thank Rosario Esposito for discussions of melt inclusion systematics, Luca Fedele for help with laser ablation ICP-MS analyses, and Charles Farley for help with Raman analyses. Comments on an earlier version of this manuscript by three anonymous reviewers and by guest editors Miriam Baumgartner and Ron Bakker greatly improved the quality and clarity of the presentation. The research was partially funded by the PhD Programme (XXV Cycle, Coordinated by B. De Vivo) "Internal dynamics of volcanic systems and hydrogeological-environmental risks" of the University of Naples Federico II, (Italy), in collaboration with Virginia Tech in the framework of the Memorandum of Understanding (MoU) signed by the two Universities. This material is based upon work supported in part by the National Science Foundation under Grant no. EAR-1019770 to RJB.

References

[1] Tait S.R., Wörner G., Van Den Bogaard P., Schmincke H.-U., Cumulate nodules as evidence for convective fractionation in a phonolite magma chamber. *J. Volcanol. Geotherm. Res.*, 1989, 37, 21-37

[2] Mattioli M., Upton B.G.J., Renzulli A., Sub-volcanic crystallization at Sete Cidades volcano, Sao Miguel, Azores, inferred from mafic and ultramafic plutonic nodules. *Mineral. Petrol.*, 1997, 60, 1-26

[3] Holness M.B., Bunbury J.M., Insights into continental rift-related magma chambers: Cognate nodules from the Kula Volcanic Province, Western Turkey. *J. Volcanol. Geotherm. Res.*, 2006, 153, 241-261

[4] Hermes O.D., Cornell W.C., Petrochemical significance of xenolithic nodules associated with potash-rich lavas of Somma-Vesuvius volcano, NSF final technical report, University of Rhode Island, 1978

[5] Belkin H.E., De Vivo B., Roedder E., Cortini M., Fluid inclusion geobarometry from ejected Mt. Somma-Vesuvius nodules. *Am. Mineral.*, 1985, 70, 288-303

[6] Belkin H.E., De Vivo B., Fluid inclusion studies of ejected nodules from plinian eruptions of Mt. Somma-Vesuvius. *J. Volcanol. Geotherm. Res.*, 1993, 58, 89-100

[7] Gilg H.A., Lima A., Somma R., Belkin H.E., De Vivo B., Ayuso R.A., Isotope geochemistry and fluid inclusion study of skarns from Vesuvius. *Mineral. Petrol.*, 2001, 73, 145-176

[8] Fulignati P., Kamenetsky V.S., Marianelli P., Sbrana A., Mernagh T.P., Melt inclusion record of immiscibility between silicate, hydrosaline, and carbonate

melts: Applications to skarn genesis at Mount Vesuvius. *Geology*, 2001, 29, 1043-1046

[9] Fulignati P., Kamenetsky V.S., Marianelli P., Sbrana A., Fluid inclusion evidence of second immiscibility within magmatic fluids (79 AD eruption of Mt. Vesuvius). *Periodico di Mineralogia*, 2005, 74, 43-54

[10] De Vivo B., Lima A., Kamenetsky V.S., Danyushevsky L.V., Fluid and melt inclusions in the sub-volcanic environments from volcanic systems: Examples from the Neapolitan area and Pontine Islands, Italy. In: Mineralogical Association of Canada Short Course 36. Montreal, Quebec, 2006, 211-237

[11] Lima A., Danyushevsky L.V., De Vivo B., Fedele L., A model for the evolution of the Mt. Somma-Vesuvius magmatic system based on fluid and melt inclusion investigations. In: De Vivo B., Bodnar R.J., Melt Inclusions in Volcanic Systems: Methods, Applications, Problems. Developments in Volcanology. Elsevier Press, Amsterdam, 2003, 227-249

[12] Lima A., De Vivo B., Fedele L., Sintoni F., Milia A., Geochemical variations between the 79 AD and 1944 AD Somma-Vesuvius volcanic products: Constraints on the evolution of the hydrothermal system based on fluid and melt inclusions. *Chem. Geol.*, 2007, 237, 401-417

[13] De Vivo B., Rolandi G., Gans P.B., Calvert A., Bohrson W.A., Spera F.J., Belkin H.E., New constraints on the pyroclastic eruptive history of the Campanian volcanic Plain (Italy). *Mineral. Petrol.*, 2001, 73, 47-65

[14] Brocchini D., Principe C., Castradori D., Laurenzi M.A., Gorla L., Quaternary evolution of the southern sector of the Campanian Plain and early Somma-Vesuvius activity: insights from the Trecase 1 well. *Mineral. Petrol.*, 2001, 73, 67-91

[15] Santacroce R., Cioni R., Marianelli P., Sbrana A., Sulpizio R., Zanchetta G., Donahue D.J., Joron J.L., Age and whole rock-glass compositions of proximal pyroclastics from the major explosive eruptions of Somma-Vesuvius: A review as a tool for distal tephrostratigraphy. *J. Volcanol. Geotherm. Res.*, 2008, 177, 1-18

[16] Rolandi G., The eruptive history of Somma-Vesuvius. In: Cortini M., De Vivo B., Volcanism and Archeology in Mediterranean Area. Reserch Signpost. Trivandrum, 1997, 77-88

[17] Ayuso R.A., De Vivo B., Rolandi G., Seal R.R., Paone A., Geochemical and isotopic (Nd-Pb-Sr-O) variations bearing on the genesis of volcanic rocks from Vesuvius, Italy. *J. Volcanol. Geotherm. Res.*, 1998, 82, 53-78

[18] De Vivo B., Petrosino P., Lima A., Rolandi G., Belkin H., Research progress in volcanology in the Neapolitan area, southern Italy: a review and some alternative views. *Mineral. Petrol.*, 2010, 99, 1-28

[19] Paone A., The geochemical evolution of the Mt. Somma-Vesuvius volcano. *Mineral. Petrol.*, 2006, 87, 53-80

[20] Bertagnini A., Landi P., Rosi M., Vigliargio A., The Pomici di Base plinian eruption of Somma-Vesuvius. *J. Volcanol. Geotherm. Res.*, 1998, 83, 219-239

[21] Landi P., Bertagnini A., Rosi M., Chemical zoning and crystallization mechanisms in the magma chamber of the Pomici di Base plinian eruption of Somma-Vesuvius (Italy). *Contrib. Mineral. Petrol.*, 1999, 135, 179-197

[22] Thomas J.B., Bodnar R.J., A technique for mounting and polishing melt inclusions in small (<1 mm) crystals. *Am. Mineral.*, 2002, 87, 1505-1508

[23] Halter W.E., Pettke T., Heinrich C.A., Rothen-Rutishauser B., Major to trace element analysis of melt inclusions by laser-ablation ICP-MS: methods of quantification. *Chem. Geol.*, 2002, 183, 63-86

[24] Mutchler S., Fedele L., Bodnar R.J., Analysis Management System (AMS) for reduction of laser ablation ICPMS data. In: Sylvester P., Laser-Ablation-ICPMS in the Earth Sciences: Current Practices and Outstanding Issues. Mineralogical Association of Canada, Vancouver, BC, 2008, 318-327

[25] Norman M.D., Pearson N.J., Sharma A., Griffin W.L., Quantitative analysis of trace elements in geological materials by laser ablation ICPMS: Instrumental Operating Conditions and Calibration Values of NIST Glasses. Geostand. Newslett., 1996, 20, 247-261

[26] Roedder E., Origin and significance of magmatic inclusions. *Bull. Mineral.*, 1979, 102, 487-510

[27] Bodnar R.J., Student J.J., Melt inclusions in plutonic rocks: petrography and microthermometry. In: Webster J.D., Melt inclusions in plutonic rocks. Mineralogical Association of Canada, 2006, 1-25

[28] Esposito R., Bodnar R.J., Danyushevsky L.V., De Vivo B., Fedele L., Hunter J., Lima A., Shimizu N., Volatile Evolution of magma associated with the Solchiaro eruption in the Phlegrean Volcanic District (Italy). *J. Petrol.*, 2011, 52, 2431-2460

[29] Belkin H.E., De Vivo B., Török K., Webster J.D., Pre-eruptive volatile content, melt-inclusion chemistry, and microthermometry of interplinian Vesuvius lavas (pre-A.D. 1631). *J. Volcanol. Geotherm. Res.*, 1998, 82, 79-95

[30] Le Bas M.J., Le Maitre R.W., Streckeisen A., Zanettin B., A chemical classification of volcanic rocks based on the total alkali-silica diagram. *J. Petrol.*, 1986, 27, 745-750

[31] Sun S.-S., McDonough W.F., Chemical and isotopic

systematics of oceanic basalts: implications for mantle composition and processes. In: Saunders A.D., Norry M.J., Magmatism in the Ocean Basins. - Geological Society Special Publication. 1989, 313-345

[32] Putirka K., Thermometers and Barometers for Volcanic Systems. In: Putirka K., Tepley III F.J., Minerals, inclusions and volcanic processes. *Mineralogical Society of America*, 2008, 61-120

[33] Cioni R., Santacroce R., Sbrana A., Pyroclastic deposits as a guide for reconstructing the multi-stage evolution of the Somma-Vesuvius caldera. *Bull. Volcanol.*, 1999, 61, 207-222

[34] Rolandi G., Bellucci F., Cortini M., A new model for the formation of the Somma Caldera. *Mineral. Petrol.*, 2004, 80, 27-44

[35] Bruno P.P.G., Cippitelli G., Rapolla A., Seismic study of the Mesozoic carbonate basement around Mt. Somma-Vesuvius, Italy. *J. Volcanol. Geotherm. Res.*, 1998, 84, 311-322

[36] De Natale G., Troise C., Trigila R., Dolfi D., Chiarabba C., Seismicity and 3-D substructure at Somma-Vesuvius volcano: evidence for magma quenching. *Earth Planet. Sci. Lett.*, 2004, 221, 181-196

[37] Cella F., Fedi M., Florio G., Grimaldi M., Rapolla A., Shallow structure of the Somma-Vesuvius volcano from 3D inversion of gravity data. *J. Volcanol. Geotherm. Res.*, 2007, 161, 303-217

[38] Danyushevsky L.V., Leslie R.A.J., Crawford A., Durance P., Melt inclusions in primitive olivine phenocrysts: the role of localized reaction processes in the origin of anomalous compositions. *J. Petrol.*, 2004, 45, 2531-2553

[39] Piochi M., De Vivo B., Ayuso R.A., The magma feeding system of Somma-Vesuvius (Italy) strato-volcano: new inferences from a review of geochemical and Sr, Nd, Pb and O isotope data. In: De Vivo B., Volcanism in the Campania Plain: Vesuvius, Campi Flegrei and Ignimbrites. Elsevier B. V., 2006, Chapter 9: 181-202

[40] Peccerillo A., Plio-Quaternary Volcanism in Italy: Petrology, Geochemistry, Geodynamics Springer, Heidelberg, 2005

Cent. Eur. J. Geosci.
DOI: 10.2478/s13533-011-0054-y

VERSITA

Central European Journal of **Geosciences**

Application of the Linkam TS1400XY heating stage to melt inclusion studies

Research Article

Rosario Esposito[1], Rita Klebesz[1,2], Omar Bartoli[3], Yury I. Klyukin[4], Daniel Moncada[1], Angela L. Doherty[1, 2, 5], Robert J. Bodnar[1]*

1 *Virginia Polytechnic Institute & State University, Department of Geosciences, Blacksburg, 24061, VA, USA*

2 *Università di Napoli Federico II, Dipartimento di Scienze della Terra, Naples, 80138, Italy*

3 *Università degli Studi di Parma, Dipartimento di Scienze della Terra, Parma, 43100, Italy*

4 *Institute of Geology and Geochemistry of Urals Branch, Russian Academy of Sciences, Yekaterinburg, Russia*

5 *Università degli Studi di Messina, Dipartimento degli Alimenti e dell'Ambiente, Messina, 98166, Italy*

Received 4 November 2011; accepted 30 January 2012

Abstract: Melt inclusions (MI) trapped in igneous phenocrysts provide one of the best tools available for characterizing magmatic processes. Some MI experience post-entrapment modifications, including crystallization of material on the walls, formation of a vapor bubble containing volatiles originally dissolved in the melt, or partial to complete crystallization of the melt. In these cases, laboratory heating may be necessary to return the MI to its original homogeneous melt state, followed by rapid quenching of the melt to produce a homogeneous glass phase, before microanalyses can be undertaken.

Here we describe a series of heating experiments that have been performed on crystallized MI hosted in olivine, clinopyroxene and quartz phenocrysts, using the Linkam TS1400XY microscope heating stage. During the experiments, we have recorded the melting behaviors of the MI up to a maximum temperature of 1360°C. In most of the experiments, the MI were homogenized completely (without crystals or bubbles) and remained homogeneous during quenching to room temperature. The resulting single phase MI contained a homogeneous glass phase. These tests demonstrate the applicability of the Linkam TS1400XY microscope heating stage to homogenize and quench MI to produce homogeneous glasses that can be analyzed with various techniques such as Electron Microprobe (EMP), Secondary Ion Mass Spectrometry (SIMS), Laser ablation Inductively Coupled Plasma Mass Spectrometry (LA ICP-MS), Raman spectroscopy, FTIR spectroscopy, etc.

During heating experiments, the optical quality varied greatly between samples and was a function of not only the temperature of observation, but also on the amount of matrix glass attached to the phenocryst, the presence of other MI in the sample which are connected to the outside of the crystal, and the existence of mineral inclusions in the host.

Keywords: microscope heating stage • melt inclusion • microthermometry • volatiles

*E-mail: rjb@vt.edu

1. Introduction

Melt inclusions provide perhaps the most direct method to study magmatic processes and the evolution of magmatic systems [1, 2], and the number of publications that mention melt inclusions has increased dramatically in recent years [3]. In fact, the only direct way to determine the volatile content of the melt in a magma body before an eruption is by measuring the volatile contents in MI. It is widely accepted that the concentration of volatiles (H_2O, CO_2, SO_2, etc.) in a magma chamber beneath a volcano determines the magnitude and style of the volcanic eruption, and many studies have focused on measurement of the volatiles in MI [1, 4]. These analyses assume that the MI represents the quenched melt that was trapped at magmatic conditions and has undergone no changes during cooling. Depending on the MI pressure-temperature path before and during natural quenching [5–8], the MI may partially or totally crystallize, and/or some of the volatiles that were originally dissolved in the melt may exsolve during cooling to form a vapor bubble. Some volatiles may also diffuse out of the MI following trapping, but this process is beyond the scope of this study and is not discussed further.

Depending on the type of information sought and the analytical technique to be used (e.g., electron microprobe analysis, EMP, or secondary ion mass spectrometry, SIMS), it may be necessary to re-homogenize the MI before analysis in order to obtain compositional data that are representative of the melt at the time of trapping. Various techniques have been used to successfully homogenize MI, including heating in one-atmosphere furnaces [9–12], heating in high-pressure (cold-seal or internally-heated) vessels [13–16], heating in piston cylinder apparatus [17–19], and heating in a microscope-mounted high temperature stage [8, 9, 20–23]. Each of these techniques has advantages and disadvantages, as described by [15, 24].

One of the major advantages of using a microscope-mounted heating stage to homogenize MI is that the MI can be observed continuously during heating from room temperature to homogenization. This approach allows information such as the temperature of first melting and the temperatures (and order) of disappearance of various phases to be observed and measured (Fig. 1 in [15]), and prevents overheating of the MI because heating can be stopped at the moment of homogenization. Importantly, homogenization of the MI using a microscope mounted heating stage allows workers to determine if phases present after quenching represent phases that were still present at the highest temperature to which the MI were heated, or if they represent phases that nucleated from the melt during quenching. This information is critical to understanding whether or not the MI trapped a single melt phase, if heating rates were sufficiently slow to maintain equilibrium between the phases in the MI, and if quenching rates were sufficiently fast to prevent new phases (crystals and vapor bubbles) from nucleating during cooling. As described in [7, 8, 25], in order to rehomogenize the melt to obtain the original volatile content of MI, many researchers have used a heating stage with a rapid quenching system mounted on an optical microscope (e.g. the Vernadsky stage, [26]). Some earlier high temperature stages, such as the Linkam TH1500 which was the precursor model to the stage described here, offered only relatively slow cooling by turning off power to the heater. In this and similar stages, it was often not possible to quench the MI without significant crystallization on the walls, or without crystallizing daughter minerals or nucleating a vapor bubble in the inclusion.

In this study, several experiments have been performed using the new Linkam TS1400XY heating stage to assess its suitability for the homogenization of MI and subsequent quenching of the homogeneous melt to a glass, and the examination of the optical viewing quality during these processes at elevated temperature. Samples studied are from the Toba Tuff eruption (Sumatra), from the Solchiaro eruption on the Island of Procida (Southern Italy), and from the Sarno eruption at Monte Somma-Vesuvius (Southern Italy). The geology and petrologic characteristics of the Toba Tuff [27–29], Solchairo eruption [30] (and references therein) and the Sarno eruption [31, 32] have been described previously, and the interested reader is referred to these sources for additional information.

The three samples used for this study were gently crushed using a wooden pestle to avoid damaging phenocrysts, and crystals were selected and mounted on glass bars and polished using the method described by [33]. Quartz phenocrysts were selected from pumice fragments of the Toba Tuff deposits, olivine and clinopyroxene phenocrysts were extracted from scoria ejected from the Solchiaro volcano, and finally clinopyroxene crystals were selected from nodules of the Sarno eruption. Only crystals containing partially or totally recrystallized MI were selected.

2. Description of the hardware and analytical conditions

The Linkam TS1400XY heating stage (Fig. 1a, c) consists of a platinum winding encased in ceramic (Fig. 1b) to produce a tube furnace that is large enough to accommodate 5 mm × 5 mm samples with a thickness of up to ≈0.5 mm. If inert gas is not circulated through the furnace during heating, the highest temperature achievable is 1400°C;

however, we highly recommend that inert gas is circulated through the furnace during operation, especially for iron-bearing host phases, as described below.

The temperature inside the furnace of the Linkam TS1400XY stage is controlled by the T95-LinkPad system controller that includes a touch-screen controller, which can be operated with either a stylus or using one's fingers (Fig. 1d). With this digital controller, the temperature can be regulated manually, similar to other microscope-mounted heating stages, but can also be programmed before each experiment with a known and constant heating rate. Ramps can also be programmed, whereby the sample is held at a temperature for some period of time before heating is continued, as was described by [12]. During heating experiments, a constant flow of an inert gas is usually introduced into the heating stage to prevent oxidation of the analyzed sample [24]. If He is circulated through the furnace to avoid oxidation of the sample at high temperature, the highest temperature reached during heating experiments was 1260°C. If Ar is circulated through the stage instead of He, the highest temperature achieved during heating experiments was 1360°C. In this study, we used Ar gas at a flow rate of 0.5 (± 5%) liter/min to prevent oxidation. With these conditions, even though we programmed the stage to go to a temperature higher than 1360°C, the temperature "plateaued" at ≈1360°C. Before each experiment, the heating stage was calibrated using the melting temperatures of NaCl (801°C) and Au (1064.2°C). The difference between the known melting temperatures of the calibration standards and the measured temperature was always <10°C.

Samples are placed on a sapphire plate that is mechanically connected to a metal frame which allows the sample to be moved into and out of the furnace (see Fig. 1b). Once the sample is inserted into the ceramic tube furnace and the lid is placed on to the stage, the sapphire plate can be moved ≈6 mm in the X and Y directions to locate and monitor inclusions during heating. The earlier version of this stage, the Linkam TH1500, did not permit the sample to be moved in the X and Y directions after the lid was placed onto the stage. The Linkam TS1400XY heating stage is provided with a spring mechanism connected to the sapphire slide (Fig. 1a, 1c). The spring mechanism allows the user to remove the crystal from the ceramic furnace rapidly to quench the MI after homogenization is achieved. When the sample is removed from the furnace using this technique, it is placed on top of a water cooled metallic platform that reduces the sample temperature to a few hundred degrees in a few seconds. The quench rate with the Linkam TS1400XY stage was determined to be ≈240°C/s from 1400 to 800°C, and ≈230°C/s from 1400 to 600°C, based on numerous quenching tests. This quench rate is slower than that reported for the Vernadsky stage (1–2 seconds to quench from as high as 1500°C to room temperature [26]), but was fast enough to quench the MI tested in this study. The heating rates that can be accommodated by the Linkam TS1400XY range from 1 to 200°C/min.

Various workers used different heating rates and protocols (continuous versus stepped heating) to homogenize silicate melt inclusions and it does not appear that any single rate or method is applicable to all MI in all different host phases. The method that is most appropriate for a given set of MI should be established based on kinetic experiments [5] that consist of heating (followed by cooling) the same MI at different heating rates (from faster to slower), and recording the homogenization temperature for each heating rate. As reported in Fig. 2 by [5], in kinetic experiments, the homogenization temperature decreases with decreasing heating rate until, eventually, the homogenization temperature approaches a constant value, even though the heating rate decreases. For each host phase, the "correct" heating rate is that which corresponds to the heating rate at which the homogenization temperature becomes constant. When faster heating rates are used, the recorded homogenization temperature will be higher compared to the homogenization temperature determined with slower heating rates (~40°C difference in Fig. 2 by [5]). However, when slower heating rates are used, the likelihood that the MI composition will be modified by diffusion of components into or out of the MI increases [24]. A complete discussion of the procedure to determine the "correct" heating rates and homogenization temperatures is beyond the scope of this study, and the reader is referred to [5, 12]. We did not perform kinetic experiments on the MI in this study because the goal of the study was not to determine the "correct" homogenization temperature. The goal was to examine the behavior of MI during heating to produce a homogeneous melt phase, and to determine if the homogenized MI could be quenched quickly enough to maintain a homogeneous melt (glass) to ambient conditions, without the formation of a vapor bubble or crystals. The heating schedules used for heating experiments on crystals from the samples studied are reported in Table 1. It should be noted that the heating rates used in this study (Table 1) are comparable to heating rates used by other workers (1 to 3°C/min near the homogenization temperature [12, 16, 34]). In some cases, after homogenization, the temperature was held constant for about 10 minutes to photograph the MI before quenching.

For the experiments described here, the Linkam TS1400XY was mounted on an Olympus BX60 petrographic microscope and 10X and 40X objective lenses were used for viewing and photographing the inclusions.

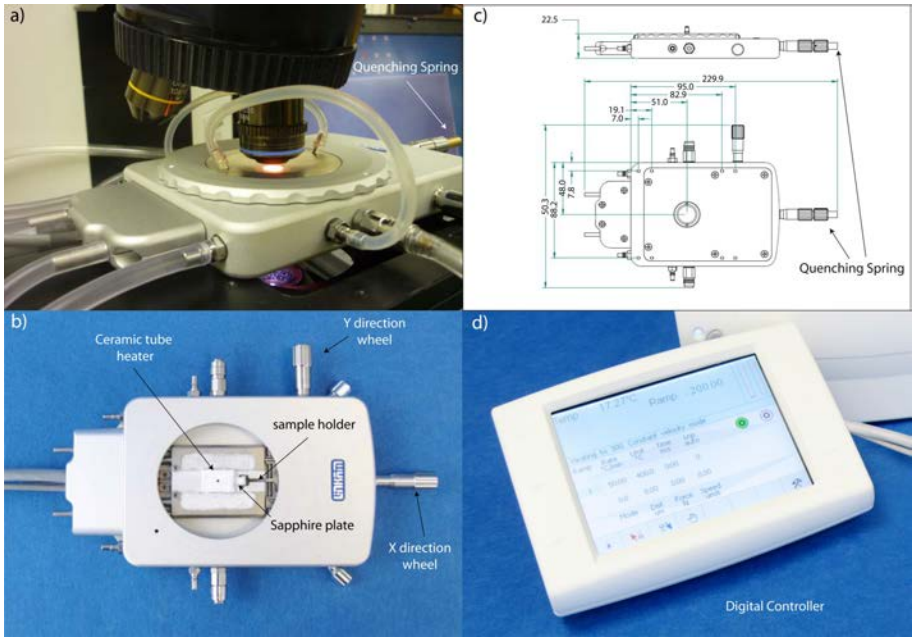

Figure 1. The Linkam TS1400XY heating stage. 1a) The Linkam TS1400XY stage mounted on a microscope during a heating experiment, with the temperature at ≈1350°C. The quenching spring is on the right side of the heating stage as indicated by the arrow. The bright spot immediately beneath the objective lens is the reddish glow from the furnace at this high temperature. 1b) The Linkam TS1400XY with the lid opened. It is possible to observe the ceramic furnace, the sapphire plate with the metallic frame, and the XY control wheels. This photo is modified from: http://www.mccronemicroscopes.com/store/catalog.asp?item=356&categoryid=48.1c) Technical drawing of the Linkam TS1400XY heating stage. All the measurements reported are in mm. Important to note is the quenching spring connected to the X-direction wheel (courtesy of V. Kamp). 1d) T95-LinkPad system controller. Additional technical information and images are available at the Linkam website (http://www.linkam.co.uk/).

Table 1. Heating schedule used for experiments on crystals from the Solchiaro, Sarno and Toba Tuff eruptions.

Temperature °C	Heating rate °C/min	sample
25 - 900	100	Solchiaro and Sarno
900 - 1000	50	Solchiaro and Sarno
1000 - 1100	25	Solchiaro and Sarno
1100 - 1200	10	Solchiaro and Sarno
1200 - 1360	5	Solchiaro and Sarno
25 - 600	100	Toba Tuff
600 - 700	50	Toba Tuff
700 - 800	25	Toba Tuff
800 - 850	10	Toba Tuff
850 - 1000	5	Toba Tuff

3. Results

In most of the experiments described here, it was possible to completely homogenize the MI and, importantly, to quench the melt to a homogeneous glass after homogenization (Figs. 2-5). A few of the MI could not be heated to homogenization, either because the optics deteriorated before homogenization was achieved or, in one case, because the crystals began to fracture and break into smaller pieces owing to the high internal pressures generated in the volatile-rich MI during heating. For such samples, it is necessary to heat the MI in a pressurized vessel to eliminate or minimize decrepitation and/or leakage [14, 15, 24, 35].

In experiments performed on crystallized MI in quartz from the Toba Tuff in Sumatra, it was always possible to completely homogenize and quench the MI to a bubble-free, homogeneous glass (Fig. 2). More importantly, during the heating experiment, the MI behavior was easy to monitor because the viewing optics remained very good up to the highest temperature required for homogenization (<1000°C) (Fig. 2). The behavior of the MI in quartz from the Toba Tuff is expected to be characteristic of MI in quartz from most environments, based on the cumulative experiences of the investigators in this study.

MI in olivine and clinopyroxene from the Solchiaro eruption on Procida Island (Southern Italy) commonly contain one or more solid phases as well as one or more vapor bubbles. These MI homogenized between 1060 and 1340°C. A range in temperatures could be related to several factors. It is well known that there is a positive correlation between the size of the MI and the temperature

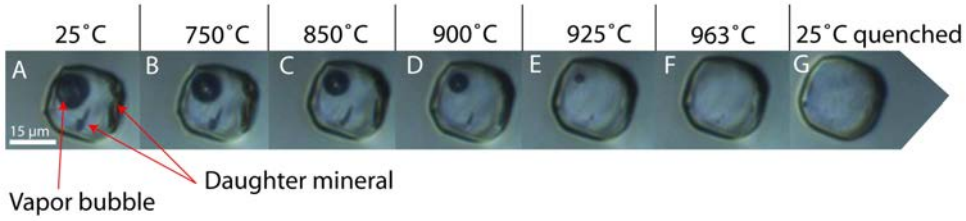

Figure 2. Heating experiment performed on quartz phenocryst from the Toba Tuff eruption in Sumatra. The MI is around 15 µm in diameter and has a sub-rectangular shape. A) At room temperature (25°C), the MI contains one vapor bubble and three unidentified daughter crystals. From B to E) From 750°C to 925 °C the volumes of the vapor bubble and of the three daughter crystals progressively decrease as these phases dissolve back into the melt. F) At 963°C the MI consists of only a homogeneous silicate melt phase. G) The MI contains a homogenous glass at ambient conditions after quenching from 963°C.

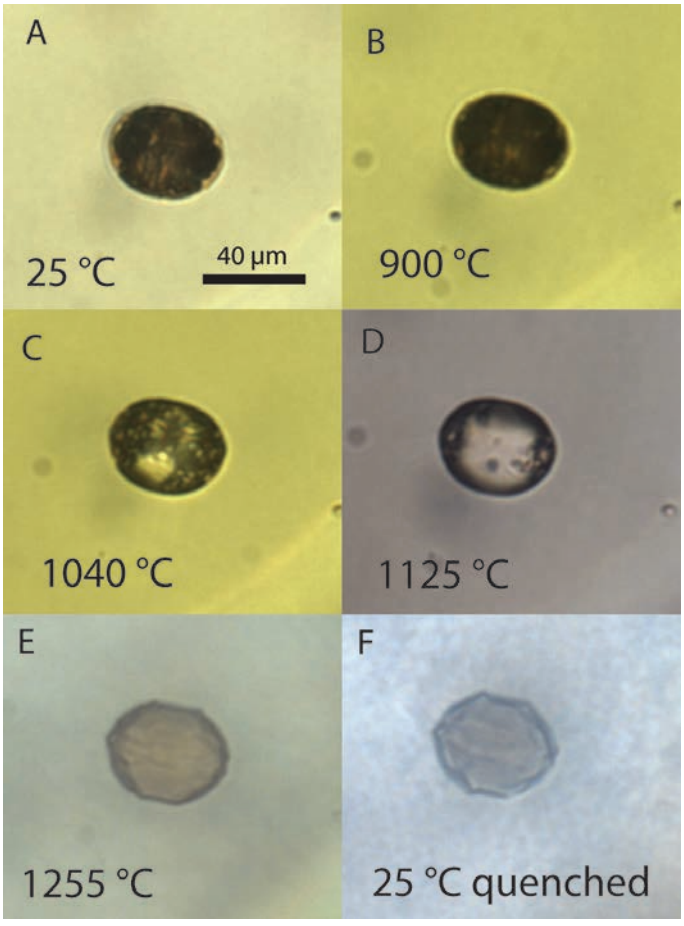

Figure 3. Heating experiment performed on MI in an olivine phenocryst from scoriae of the Solchiaro eruption of the Phlegrean Volcanic District (PVD) in Southern Italy. The MI has an ellipsoidal shape. A) At room temperature (25°C), the MI is partially crystallized and nearly opaque. Some daughter crystals are visible at the olivine host – melt inclusion interface. B) At 900°C, daughter crystals at the olivine/inclusion interface are smaller relative to those at room temperature. C) At 1040°C it is possible to observe some vapor bubbles, solid and melt phases. D) At 1125°C most of the melt inclusion consists of a silicate melt phase. E) At 1255°C the MI is completely homogenized and contains only a melt phase. Note that at this temperature the MI assumes a negative crystal shape. Also, the "wrinkles" at the melt/crystal interface may indicate that the MI was overheated and that the host phase has begun to melt. F) After quenching from >1260°C to ambient temperature the MI contains a homogenous glass. During the quenching, some crystallization of olivine at the olivine/glass interface may have occurred.

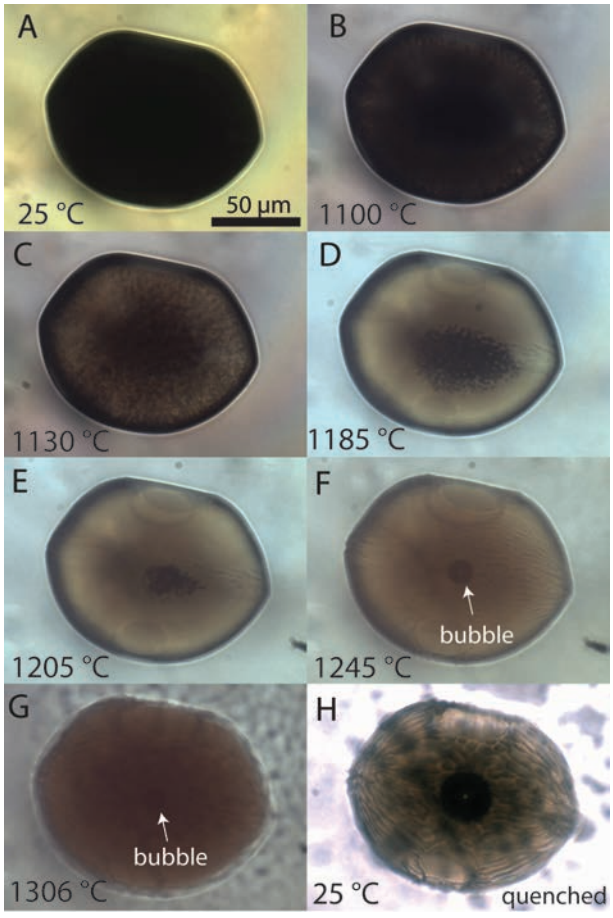

Figure 4. Heating experiment performed on MI contained in an olivine phenocryst from scoriae of the Solchiaro eruption of the Phlegrean Volcanic District (PVD) in Southern Italy. The MI has a sub-negative crystal shape with smooth olivine/inclusion interface. A) At room temperature (25°C), the MI is totally crystallized and may be mis-identified as an opaque solid inclusion (e.g., spinel) during petrographic examination. There are no features visible to suggest that this is a melt inclusion. B) At 1110°C a melt phase can be observed near the olivine/MI interface. The inner part of the MI remains dark. C) As the temperature increases (e.g., 1130°C), the melt region expands toward the center of the MI. D) At 1185°C the black spots in the interior of the MI appear to assemble to form larger vapor bubbles. The MI tends to a more negative crystal shape as the temperature increases. E) At 1205°C a few vapor bubbles are observed and most of the MI consists of silicate melt. F) At 1245°C the MI consists of silicate melt and a single vapor bubble in the center of the MI. G) During heating from 1300 to 1340°C the bubble does not dissolve into the melt and the bubble size does not change. At 1340°C the MI was no longer visible as the field of view became dark and with a reddish glow. H) After quenching from 1340°C to room temperature, the MI contains a homogenous glass plus a vapor bubble that is likely of primary origin. Note the difference between the MI before the experiment and after quenching. The glass composition can be analyzed for major, trace and volatile elements, while the bubble can be analyzed for volatiles using Raman spectrometry.

of homogenization, because the larger the inclusion, the greater the energy necessary to melt the crystal around the MI [7]. However, in these experiments there was no correlation between the size of MI and the temperature of homogenization, suggesting that MI size was not responsible for this temperature range. Rather, the temperature range reflects differences in melt composition reflecting trapping at different times during evolution of the magma. Thus, more primitive MI entrapped in more primitive olivine/clinopyroxene show homogenization temperatures that are much higher than MI entrapped in more evolved phenocrysts (e.g., Fo-poor olivine) [30]. Furthermore, phenocrysts may not be linked genetically and thus MI analyzed may have formed in totally different environments within the magma body, and/or at different times. For this study, petrographic analysis of the phenocrysts and MI was not conducted because the purpose of this study was not to determine a melt petrogenesis, but rather, to test suitability of the Linkam stage for homogenizing and quenching MI.

Some experiments on recrystallized MI from Solchiaro produced homogeneous glassy MI with no vapor bubble (Fig. 3) after quenching from high temperature (1060 to ~1300°C). In a few experiments, the sample was heated to

approximately 1340°C but complete homogenization was not achieved. During heating to that temperature, the field of view became progressively darker and a reddish glow developed, making it difficult to observe the behavior of the MI during continued heating. Darkening and development of the reddish glow generally became noticeable and caused the optics to degrade to the point where the MI could no longer be observed over a temperature range of about 50°C. At lower temperatures, the optics were generally excellent, with the quality of the optics depending mostly on two factors: the thickness of the phenocryst and the relative area of the sample represented by solid and/or melt inclusions, with the optical quality being inversely related to the inclusion content. Also, the optics improved if the crystal was free of matrix glass. As previously noted by [15], groundmass adhering to phenocrysts affects the optics because it consists of dark recrystallized glass that generally melts before the MI has completely homogenized and flows around the crystal (or through fractures in the crystal) causing the optics to deteriorate. In order to remove matrix glass from the crystals before heating experiments, some authors have suggested that the samples should be placed in concentrated hydrofluoric acid solution for several seconds [15, 36], but this was not done for the phenocrysts studied here.

In some cases, the MI were heated to relatively high temperature and all of the solids in the MI melted, but the vapor bubble did not completely dissolve back into the melt before the optics deteriorated and it was no longer possible to observe the MI behavior. When the MI was quenched from a temperature slightly higher than that at which the MI could no longer be observed (*blind quenching*), the single bubble that (presumably) remained in the MI grew larger as the MI cooled due to the effect of the greater thermal contraction of the melt relative to the host (Fig. 4). Because the MI could not be observed to the point of complete vapor bubble disappearance, it is not clear if the bubble did indeed disappear but renucleated during cooling, or if the bubble never completely disappeared and simply grew larger during cooling. Moreover, the bubble in these MI may represent a trapped vapor bubble (i.e., the MI trapped a volatile-saturated melt plus a vapor bubble) and, thus, the bubble should not be expected to dissolve back into the melt. Another interpretation (especially for relatively larger MI) could be that the internal pressure in the MI is now less than the internal pressure at the moment of the entrapment owing to the compressibility of the host phase. Because the host phase is heated at one atmosphere pressure during the experiments, the confining pressure is lower than the pressure at which the phenocryst trapped the MI. Therefore, the volume of the host phase, and the "cavity" represented by the

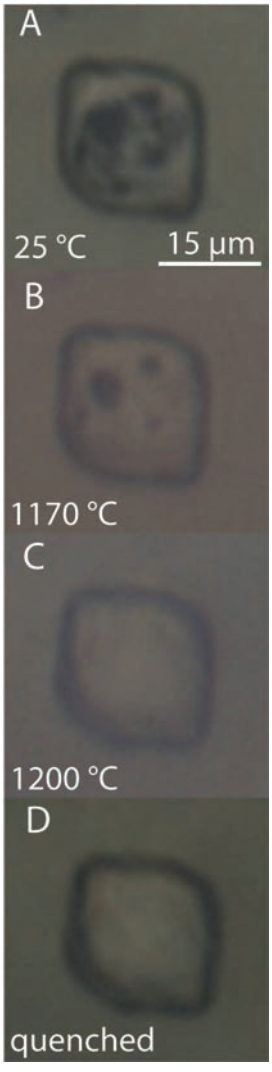

Figure 5. Heating experiment performed on a melt inclusion in clinopyroxene from a nodule from the Sarno eruption at Mt Somma-Vesuvius in Southern Italy. The Sarno eruption is considered to be the largest volume eruption in the history of Somma-Vesuvius [31]. A) At room temperature (25°C), the MI is partially crystallized. Some daughter crystals or vapor bubbles are visible. B) At 1170°C the size of the daughter crystals/vapor bubbles has decreased significantly. C) At 1200°C MI contains only silicate melt. F) After quenching from 1200°C to room temperature, the MI contains a homogenous glass.

MI, is slightly greater than that at the time of trapping, resulting in lower internal pressure in the MI during laboratory heating and, concomitantly, lower volatile solubility in the melt phase. A final explanation for the fact that the bubble remained at the highest temperature to which the MI could be heated and observed is that the actual homogenization temperature is higher than this temperature. However, in our experiment, the latter interpretation

is unlikely owing to the widespread melting of the host observed at these high temperatures (e.g., >1320°C).
In half of the experiments performed on clinopyroxene-hosted, recrystallized MI from nodules from the Sarno eruption of Monte Somma-Vesuvius (Southern Italy), it was possible to quench the MI to a homogeneous glass without re-nucleating vapor bubbles (Fig. 5). Similar to samples from Solchiaro, some of the MI could not be monitored completely up to the temperature of homogenization owing to the deterioration of the optics above a certain temperature. Crystals from the Sarno eruption are rich in solid and recrystallized MI. For this reason, the optics deteriorated at a lower temperature, compared to the experiments performed on olivines from Solchiaro, which contain relatively few melt and solid inclusions. For the Sarno clinopyroxene-hosted MI, the optics remained relatively good up to ≈1260°C; above this temperature they deteriorated rapidly with further heating.

4. Discussion of advantages and limitations of the Linkam TS1400XY stage

The most important advantage of using a microscope-mounted heating stage (such as the Linkam TS1400XY) relative to one atmosphere furnaces and high pressure autoclaves is that the MI can be observed continuously during the heating/cooling experiments [15]. For example, the appearance/disappearance of a microscopically recognizable phase is possible during heating experiments using these types of devices, but is not possible when the MI is heated in a furnace. Also, the temperatures at which phase changes occur in the MI can be determined with better precision using a microscope-mounted heating stage, compared to a large volume furnace. As noted by [15] the ability to monitor the behavior of MI from the Red Mountain, Arizona, porphyry copper deposit continuously during heating, made it possible for those workers to determine that quartz, plagioclase and probably apatite were three minerals on the liquidus when the melt inclusions were trapped, and that the melt was H_2O-saturated. These workers were also able to distinguish between MI that trapped only a melt phase, and those that trapped melt ± crystals ± vapor, and to eliminate those MI that trapped multiple phases from any subsequent analyses.
Compared to some other microscope-mounted heating stages, the Linkam TS1400XY stage offers several advantages. Firstly, the Linkam TS1400XY heating stage is a "turn key" digitally controlled system (e.g., the T95-LinkPad; see Fig. 1d), while some other heating stages require the user to design and build a system to control and monitor the temperature. Thus, compared to some other commercially available stages, the Linkam system may be better for someone who does not have access to machining and/or electronics facilities. The digitally controlled system allows one to set heating/cooling cycles, which, as described above, can be used to establish heating rates to determine the "correct" temperature of homogenization. These cycles adopted during kinetic experiments are easier to perform when the heating rates are controlled electronically rather than manually. Secondly, we found it easier to load crystals into the furnace of the Linkam TS1400XY stage than it is to load crystals into the somewhat confined platinum furnace of the Vernadsky stage. Thirdly, the position of the crystal under the microscope can be moved during the heating experiment without the need to move the entire heating stage. In this way, more MI in a single grain can be monitored while viewing the sample at high magnification during heating experiments by moving the crystal in X-Y space during observation. Finally, in the Vernadsky stage the analyzed crystal is placed onto a metal frame and thus photography during the heating experiment may be compromised, while in the Linkam TS1400XY stage the analyzed crystal sits on a sapphire slide which is transparent to light, resulting in relatively good optics during most of the heating sequence.

As reported above, even though the quench rate with the Linkam TS1400XY stage is slower than that of the Vernadsky stage (≈240°C/s from 1400 to 800°C, and ≈230°C/s from 1400 to 600°C), the quenching rate was fast enough to quench the MI tested in this study. The most significant limitation of the Linkam TS1400XY heating stage identified in this study is the poor visibility that sometimes results during high temperature operation. This effect was not observed for MI hosted in quartz, but was only observed with olivine and pyroxene-hosted MI that require higher temperatures to achieve homogenization. In our experiments involving olivine from Solchiaro, the optics degraded to the point where the MI were not recognizable at a temperature around 1340°C. For experiments on clinopyroxene from the Sarno eruption, the visibility deteriorated to the point that it was not possible to observe the behavior of MI at a temperature around 1260°C. In most cases, the deterioration in the optics was manifested by the sample becoming darker and with a reddish glow that increased in intensity as the temperature increased. The deterioration in optical quality during heating MI in olivine and clinopyroxene is influenced by (1) the presence of matrix glass adhering to the phenocryst, (2) the presence of MI connected (open) to the crystal surface, because they may "boil" during heating, releasing melt to the outside of the crystal, and (3) the high abundance

of solid/melt inclusions in the sample. In addition, we noticed that the optics improved as the sample became thinner. Our observations suggest that during heating the infrared energy ("light") generated by the hot furnace ceramic is reflected in all directions, leading to deterioration in the optics during high temperature experiments. The presence of matrix glass, solid and melt inclusions in the sample, and melt on the exterior of the crystal all serve to enhance this reflection. If a microscope-mounted digital camera is used during heating experiments, the visibility may be improved. Also, the optical issue may be solved in the future by using a confocal method of observation (e.g., spinning disc or laser confocal; V. Kamp, personal communication). In addition, it should be emphasized that the degradation of the optics at a high temperature is not unique to the Linkam TS1400XY heating stage, but also occurs with the Vernadsky stage (and probably with other high temperature microscope stages). The effect is less significant in the Vernadsky stage because of the smaller size of the furnace and because the sample is not encased (or surrounded) by ceramic material.

In summary, the following suggestions can be adopted in order to improve the optical quality during heating experiments using the Linkam TS1400XY. First of all, as much of the matrix glass as possible should be removed from the crystals before heating experiments are conducted (e.g., using concentrated hydrofluoric acid solution as suggested by [15, 36]). Secondly, the host crystals should be as thin as possible because, as explained above, less material reflects less light (infrared energy) generated in the furnace at high temperature. Thirdly, a microscope-mounted digital camera should be used to improve the visibility, especially at high temperature when it becomes difficult to make any observation looking through the microscope lens. Finally, the optics may be improved by using a different optical imaging technique, such as confocal spinning disk or a confocal laser scanning microscope.

5. Summary

Tests confirm that the Linkam TS1400XY heating stage is capable of heating MI to homogenization and quenching to produce a homogenous glass. This method produces glassy MI that can be analyzed using various microanalytical techniques that require a single, homogeneous phase for quantitative analysis to determine the compositions (especially the volatile contents) of the pre-eruptive melt. Experiments performed on recrystallized MI that homogenize at less than ~1100°C are optimal for observing the heating/cooling behavior of MI. Thus, for felsic melts and most intermediate composition melts, optical conditions during heating/cooling experiments are generally quite good. For mafic melt compositions, or samples with crystals that are rich in matrix glass, or contain opened MI or mineral inclusions, the optical quality may deteriorate to the point where the inclusion is no longer visible during heating experiments, and cannot be observed to complete homogenization.

Acknowledgements

We would like to thank the Linkam Group for providing the opportunity to test the functions of the Linkam TS1400XY heating stage, in particular Jeff D. McGinn and Vincent Kamp. We also thank Matthew Steele-MacInnis and Pilar Lecumberri Sanchez for discussions on the topic and editorial assistance. This material is based upon work supported by the National Science Foundation under grant no. EAR-1019770.

References

[1] Métrich N., Wallace P.J., Volatile abundances in basaltic magmas and their degassing paths tracked by melt inclusions. In: Putirka K.D.and Tepley F.J., Minerals, Inclusions and Volcanic Processes. *Rev. Mineral. Geochem.*, 2008, 69, 363-402

[2] Sobolev A.V., Hofmann A.W., Jochum K.P., Kuzmin D.V., Stoll B., A young source for the Hawaiian plume. *Nature*, 2011, 476, 434-437

[3] De Vivo B., and Bodnar, R.J., Melt inclusions in volcanic systems. Elsevier Science, the Netherlands, 2003

[4] Helo C., Longpre M.A., Shimizu N., Clague D.A., Stix J., Explosive eruptions at mid-ocean ridges driven by CO_2-rich magmas. *Nat. Geosci.*, 2011, 4, 260-263

[5] Danyushevsky L.V., McNeill A.W., Sobolev A.V., Experimental and petrological studies of melt inclusions in phenocrysts from mantle-derived magmas: an overview of techniques, advantages and complications. *Chem. Geol.*, 2002, 183, 5-24

[6] Lowenstern J.B., Applications of silicate-melt inclusions to the study of magmatic volatiles. In: Thompson J.F.H. (Ed.), Magmas, Fluids and Ore Deposits. Mineralogical Association of Canada, Short Course, Canada, 1995, 23, 71-99

[7] Roedder E., Origin and significance of magmatic inclusions. *B. Mineral.*, 1979, 102, 487-510

[8] Sobolev A.V., Kostyuk V.P., Magmatic crystallization based on study of melt inclusions. In: Roedder E. (Ed.), Fluid Inclusion Research, Proceedings of COFFI, The University of Michigan Press, 1976, 9, 182-253

[9] Fedele L., Bodnar R.J., DeVivo B., Tracy R., Melt inclusion geochemistry and computer modeling of trachyte petrogenesis at Ponza, Italy. *Chem. Geol.*, 2003, 194, 81-104

[10] Nielsen R.L., Crum J., Bourgeois R., Hascall K., Forsythe L.M., Fisk M.R., Christie D.M., Melt inclusions in high-An plagioclase from the Gorda Ridge: an example of the local diversity of MORB parent magmas. *Contrib. Mineral. Petr.*, 1995, 122, 34-50

[11] Sinton C.W., Christie D.M., Coombs V.L., Nielsen R.L., Fisk M.R., Near-primary melt inclusions in anorthite phenocrysts from the Galapagos Platfrom. *Earth Planet. Sc. Lett.*, 1993, 119, 527-537

[12] Student J.J., Bodnar R.J., Synthetic Fluid Inclusions XIV: Coexisting Silicate Melt and Aqueous Fluid Inclusions in the Haplogranite–H_2O–NaCl–KCl System. *J. Petrol.*, 1999, 40, 1509-1525

[13] Anderson A.T., Davis A.M., Lu F., Evolution of Bishop Tuff Rhyolitic Magma Based on Melt and Magnetite Inclusions and Zoned Phenocrysts. *J. Petrol.*, 2000, 41, 449-473

[14] Skirius C.M., Peterson J.W., Anderson A.T., Homogenizing Rhyolitic Glass Inclusions from the Bishop Tuff. *Am. Mineral.*, 1990, 75, 1381-1398

[15] Student J.J., Bodnar R.J., Silicate melt inclusions in porphyry copper deposits: Identification and homogenization behavior. *Can. Mineral.*, 2004, 42, 1583-1599

[16] Thomas J.B., Bodnar R.J., Shimizu N., Chesner C.A., Melt Inclusions in Zircon. *Rev. Mineral. Geochem.*, 2003, 53, 63-87

[17] Bartoli O., Cesare B., Poli S., Bodnar R.J.., Frezzotti M.L., Acosta-Vigil A, Meli S., Melting in the deep crust: message from melt inclusions in peritectic garnet from migmatites. *Mineral. Mag.*, 2011, 75, 495

[18] Cesare B., Acosta-Vigil A., Ferrero S., Bartoli O., Melt inclusions in migmatites and granulites. *J. Virt. Expl.*, 2011, 40, n. 2, doi: 10.3809/jvirtex.2011.00268

[19] Ferrero S., Bartoli O., Cesare B., Salvioli-Mariani E., Acosta-Vigil A., Cavallo A., Groppo C., Battiston S., Microstructures of melt inclusions in anatectic metasedimentary rocks. *J. Metamorph. Geol.*, 2012, doi: 10.1111/j.1525-1314.2011.00968.x

[20] Clocchiatti R., Les inclusions vitreuses des cristaux de quartz; Etude optique, thermo-optique et chimique; Applications geologiques. Vitreous inclusions in quartz crystals; optical, thermo-optical and chemical studies; geologic applications. *Mem. S. Geo. F.*, no, 1975, 122

[21] Frezzotti M.L., Magmatic immiscibility and fluid phase evolution in the Mount Genis granite (southeastern Sardinia, Italy). *Geochim. Cosmochim. Ac.*, 1992, 56, 21-33

[22] Lowenstern J.B., Dissolved Volatile Concentrations in an Ore-Forming Magma. *Geology*, 1994, 22, 893-896

[23] Reyf F.G., Direct evolution of W-rich brines from crystallizing melt within the Mariktikan granite pluton, west Transbaikalia. *Miner. Deposita*, 1997, 32, 475-490

[24] Bodnar R.J., Student J.J., Melt inclusions in plutonic rocks: Petrography and microthermometry. In: Webster J.D. (Ed.), Melt Inclusions in Plutonic Rocks, Mineralogical Association of Canada, Short Course, Montreal, Quebec, 2006, 36, 1-25

[25] Schiano P., Primitive mantle magmas recorded as silicate melt inclusions in igneous minerals. *Earth-Sci. Rev.*, 2003, 63, 121-144

[26] Sobolev A.V., Dmitriev L.V., Barsukov V.L., Nevsorov V.N., Slutsky A.B., The formation conditions of the high magnesium olivines from the monomineralic fraction of Luna 24 regolith. Proceedings of the 11th Lunar and Planetary Science Conference, 1980, 105-116

[27] Beddoe-Stephens B., Aspden J.A., Shepherd T.J., Glass inclusions and melt compositions of the Toba Tuffs, northern Sumatra. *Contrib. Mineral. Petr.*, 1983, 83, 278-287

[28] Newman S., Chesner C., Volatile compositions of glass inclusions from the 75Ka Toba Tuff, Sumatra. Paper presented at the 1989 annual meeting of the Geological Society of America, St. Louis, MO, US, November 6-9, 1989

[29] Chesner C.A., Petrogenesis of the Toba Tuffs, Sumatra, Indonesia. *J. Petrol.*, 1998, 39, 397-438

[30] Esposito R., Bodnar R.J., Danyushevsky L., De Vivo B., Fedele L., Hunter J., Lima A., Shimizu N., Volatile Evolution of Magma Associated with the Solchiaro Eruption in the Phlegrean Volcanic District (Italy). *J. Petrol.*, 2011, 52, 2431-2460

[31] Bertagnini A., Landi P., Rosi M., Vigliargio A., The Pomici di Base plinian eruption of Somma-Vesuvius. *J. Volcanol. Geoth. Res.*, 1998, 83, 219-239

[32] Landi P., Bertagnini A., Rosi M., Chemical zoning and crystallization mechanisms in the magma chamber of the Pomici di Base plinian eruption of Somma-Vesuvius (Italy). *Contrib. Mineral. Petr.*, 1999, 135, 179-197

[33] Thomas J.B., Bodnar R.J., A technique for mounting and polishing melt inclusions in small (>1 mm) crystals. *Am. Mineral.*, 2002, 87, 1505-1508

[34] Sobolev A.V., Danyushevsky L.V., Dmitriev L.V., Sushchevskaya N.M., High-Alumina Magnesium Tholeiite as One of Primary Melts of Basalts of the Mid-Oceanic Ridges. *Geokhimiya+*, 1988, 1522-1528

[35] Severs M.J., Azbej T., Thomas J.B., Mandeville C.W.,

Jr., Bodnar R.J., Experimental determination of H_2O loss from melt inclusions during laboratory heating. *Chem. Geol.*, 2007, 237(3-4), 358-371

[36] Anderson A.T., Jr., Hourglass inclusions; theory and application to the Bishop rhyolitic tuff. *Am. Mineral.*, 1991, 76, 530-547